DLR-IB-FT-BS-2024-135

Dassault Falcon 2000LX ISTAR

System Identification - Part I
Process and Aerodynamic Model Description

V1.0

Internal Report

Autor: Dipl.-Ing. Christian Raab

Deutsches Zentrum
DLR für Luft- und Raumfahrt

Institute Report
DLR-IB-FT-BS-2024-135

Dassault Falcon 2000LX ISTAR

System Identification - Part I
Process and Aerodynamic Model Description
V1.0

DLR
Institute of Flight Systems
Braunschweig

83 Pages
60 Figures
9 Tables

German Aerospace Center (DLR)
Institute of Flight Systems
Department of Flight Dynamics and Simulation

Level of Accessibility: I, internally and externally unlimited distribution

Braunschweig, 20. August 2024

Institute Director:	Prof. Dr.-Ing. S. Levedag
Department Head:	Dipl.-Ing. P. Ohme
Author:	Dipl.-Ing. C. Raab

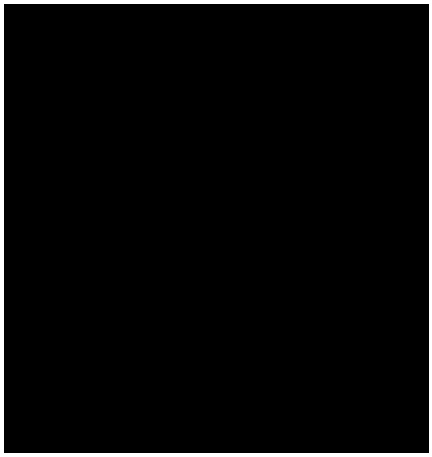

Table of Contents

Nomenclature

$C_{(.)}$	Aerodynamic parameter with influence factor in subscript (.)	-
C_D	Drag force coefficient	-
C_L	Lift force coefficient	-
C_Y	Side force coefficient	-
C_l	Roll moment coefficient	-
C_m	Pitch moment coefficient	-
C_n	Yaw moment coefficient	-
F_T	Engine net thrust	N
I_{XX}, I_{YY}, I_{ZZ}	Mass moments of inertia about the body-fixed axes	kgm²
I_{XZ}	Deviation mass moment of inertia	kgm²
a_x, a_y, a_z	Translational accelerations along the body axes	m/s²
$\bar{c}$	Half-wing span	m
g_0	Standard acceleration due to gravity = 9.80665 m/s²	m/s²
i_{HT}	Horizontal stabilizer deflection	rad
l_μ	Reference length	m
$\bar{q}$	Dynamic pressure	N/m²
q_0, q_1, q_2, q_3	Quaternion components	-
r_{HT}	Distance between the aircraft CG and the horizontal tail reference point.	m
r^*_{HT}	Distance between the aerodynamic reference point and reference point of the horizontal tail.	m
z^*_{HT}	Vertical distance between the aerodynamic and the horizontal tail reference point.	m
α_{dyn}	Dynamic angle of attack	rad
δ_{AB}	Airbrake deployment state	-
δ_{LG}	Landing gear state	-
δ_{SF}	Slat / Flap configuration	-
δ_T	Thrust coefficient	-
σ_y	Engine tilt angle	rad
σ_z	Engine kink angle	rad
h	Aircraft altitude	m
Δt	Time delay	s
Λ	Aspect ratio	-
Φ, Θ, Ψ	Roll, pitch and heading angle	rad
L, M, N	Moments about the body-fixed coordinate axes	Nm
Ma	Mach number	-
$PG_{C_{(.)}}$	Prandl-Glauert factor for the aerodynamic parameter $C_{(.)}$	-
S	Wing area	m²
T	Tensor with mass moments of inertia	kgm²
V	Speed	m/s
X, Y, Z	Force components along the body-fixed axes	N
b	Wing span	m
e	Oswald factor	-
m	Aircraft total mass	kg
p	Pressure	N/m²
p, q, r	Roll, pitch and yaw rate	rad/s

t	Time	s
u, v, w	Velocity components	m/s
x, y, z	Position coordinates / Distances	m
α	Angle of attack	rad
β	Angle of sideslip	rad
ζ	Rudder deflection	rad
η	Elevator deflection	rad
ξ	Aileron deflection	rad
ϵ	Downwash angle	rad
$\varkappa$	Isentropic exponent = 1.4	-

Subscripts

0	Initial value
A	Aerodynamic
CG	Center of gravity
E	Engine
HT	Horizontal tail
LH, RH	Lefthand, righthand
MAC	Mean aerodynamic chord
RP	Aerodynamic reference point
TAS	True airspeed
WB	Wing and aircraft body (fuselage)
b	Body-fixed coordinate frame
e	Aerodynamic coordinate frame
r	Geometric reference coordinate frame
ref	Reference
s	Static
t	Total

Abbreviations

AVES	Air Vehicle Simulator
CFD	Computational Fluid Dynamics
CG	Center of Gravity
DCC	Data Compatibility Check
FETP	Flight Envelope Test Point
ISTAR	In-Flight Systems and Technologies Airborne Research
SF	Slat / Flap Configuration
Sys-ID	System Identification
TP	Test Points
VLE	Maximum speed with extended landing gear.
VLO	Maximum speed for landing gear operation
ZFW	Zero Fuel Weight

1. Introduction

The DLR aircraft Dassault Falcon 2000LX ISTAR is designed as research platform for new flight control and pilot assistance systems. It is also equipped with an additional flight data and structural monitoring sensors for research and application of big data analysis methods. Before flight testing these algorithms, they have to be designed and tested thoroughly on ground. For this purpose, an accurate flight dynamic model of the aircraft is needed. This model is used for hardware in the loop testing and for the flight preparation in a ground simulator of the ISTAR aircraft.

Figure 1: The DLR research aircraft Dassault Falcon 2000LX ISTAR with installed nose boom (Photo: Uwe Bethke, LCBS Braunschweig)

This report describes the results of the system identification campaign of the ISTAR, which was carried out as part of the DLR HighFly project. Well-proven system identification methods were applied for the creation of a flight dynamic model. It started with the planning and execution of a flight test program where system identification maneuvers were performed at different flight test points across the flight envelope.

For confidential reasons the report is split into two parts: The first part describes the process of system identification and describes the identified aerodynamic model structure, whereas the second part [19] contains the estimated model parameters and detailed times series plots of the model validation.

Accurate flight data, especially from the air data sensors, are a necessary requirement for the identification of an accurate aerodynamic model. Aircraft sensor measurements were evaluated and if necessary corrections were applied during a Data Compatibility Check (DCC) which was performed in front of the system identification. The results of the DCC and the detailed information about the aircraft sensors can be found in reference [18].

The individual flights analyzed in this report are listed in Table 1. Flight data measured during these maneuvers is corrected for sensor errors and processed for system identification. An overview of the gathered flight data is given in Chapter 2. Aircraft geometry is important for the definition of flight dynamic model and the aerodynamic properties. Chapter 3 contains a definition of the aircraft reference axes and important geometrical quantities. The system identification process and the additional preprocessing steps are described in Chapter 4. As result of the system identification an aerodynamic model for the ISTAR aircraft was developed. A detailed formulation of the aerodynamic model can be found in Chapter 6. The output of the identified flight dynamic model was evaluated concerning the remaining differences compared to the flight data measurements. Finally, the model was validated with maneuvers at selected operating points. Plots for the evaluation of the identified aerodynamic model are presented in Chapter 7. Finally, a conclusion and outlook are given in Chapter 8.

Table 1: ISTAR flights with system identification maneuvers.

Date	Flight No.	Take Off	Landing	Flight Time
23-FEB-2022	F062	15:00	17:10	2:10
28-FEB-2022	F063	11:30	13:40	2:10
29-APR-2022	F066a	05:10	06:00	0:50
29-APR-2022	F066b	06:20	08:00	1:40
29-APR-2022	F066c	09:05	09:50	0:45
02-MAY-2022	F067	12:05	14:20	02:15
03-MAY-2022	F068	10:05	13:00	2:55
04-MAY-2022	F069	11:55	14:45	2:50
09-MAY-2022	F071	11:40	14:35	2:55
10-MAY-2022	F072	08:35	11:15	2:55
12-MAY-2022	F072	11:30	14:00	2.:40

2. Flight Data

2.1. Flight Test Points and Data Envelope

The scope of the ISTAR system identification was the generation of a model representing the flight dynamics across the complete range of the flight envelope. A flight test request [20] with the test points and the planned maneuvers covering the ISTAR flight envelope was compiled. Test points with different altitude and speed as were planned which are considering different aerodynamic configurations e.g. slat/flap setting, landing gear status and also compressibility effects depending on the Mach number. An overview of the flight envelope test points (FETP) and the collected flight data considered in this report is shown in Figure 2.

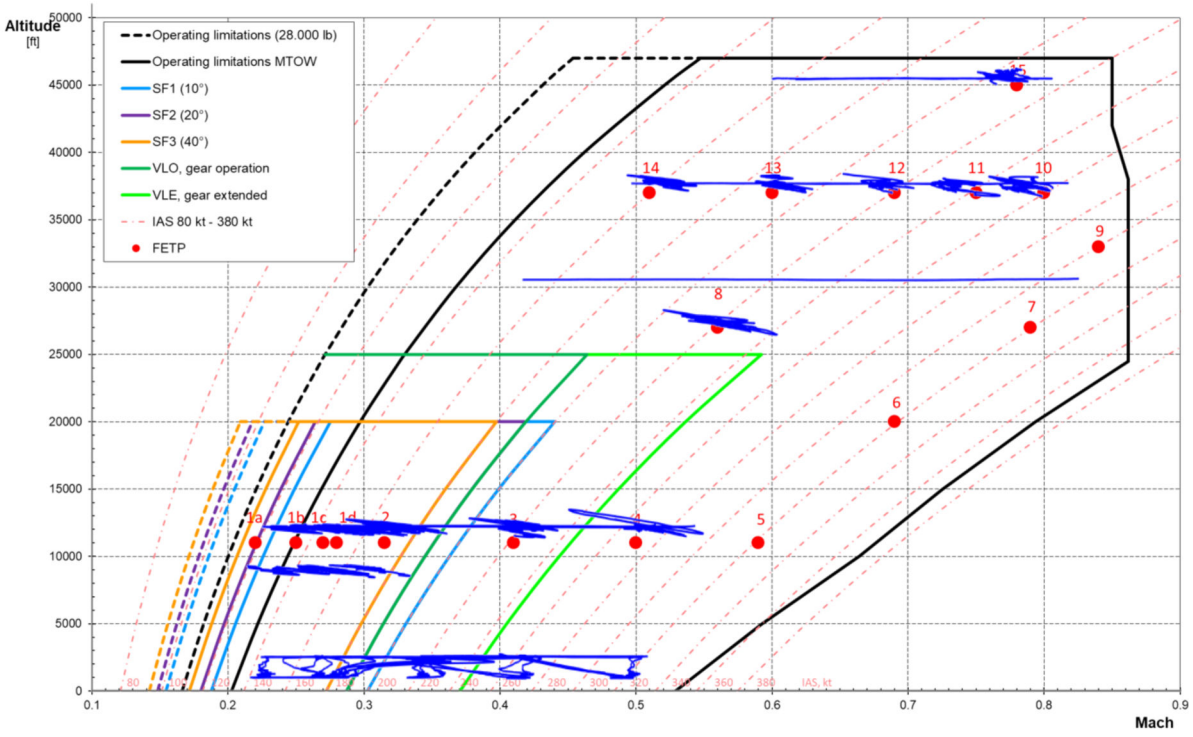

Figure 2: Overview of the flight data envelope with planned flight test points for system identification maneuvers (red circles) and the measured flight data (blue lines).

Red circles on the envelope represent the planned test points numbered according to the description in the flight test request. The blue lines represent the flight data measurements collected during the flight test campaign. In the flight envelope diagram system identification maneuvers are presented as well as level acceleration and deceleration flights performed e.g. at flight level (FL) 300 and tower fly-byes near ground. TPs number 5, 6, 7 and 9 are not included in the current flight test data, but are planned to be flown in an additional test campaign in 2025.

The following diagrams show the coverage of the flight test data important for the identification of representative aerodynamic model. The angle of attack (AOA) of the acquired flight test data is shown in Figure 3 and covers a range between around -4 to 12 deg. In Figure 4 the angle of sideslip coverage (AOS) is presented and shows a range between around -10 to 10 deg. The quality of the identified aerodynamic model depends on a good coverage of the AOA and AOS data. At this point it should be mentioned that flight data at high AOAs near stall is currently not part of the gathered flight data. This will be part of the extended flight test program were data near the bordered of the envelope at high and low speed will be gathered. For the identification of aerodynamic effects which depend on the aircraft structural flexibility, the coverage of the vertical load factor plays an important role and is shown in the diagram of Figure 5. High variations in the load factor are caused by the maneuvers performed at specified TPs. For example, at a Mach No. of 0.78 the vertical load factor ranges from 0.4 up to 2.1 g.

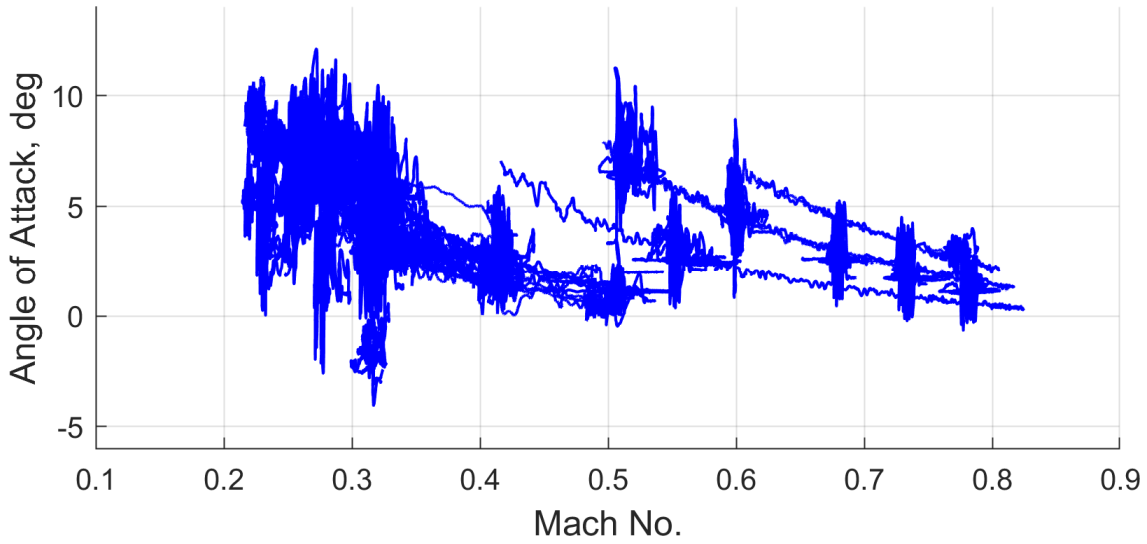

Figure 3: Angle of attack vs. Mach No. for the total analyzed flight test data.

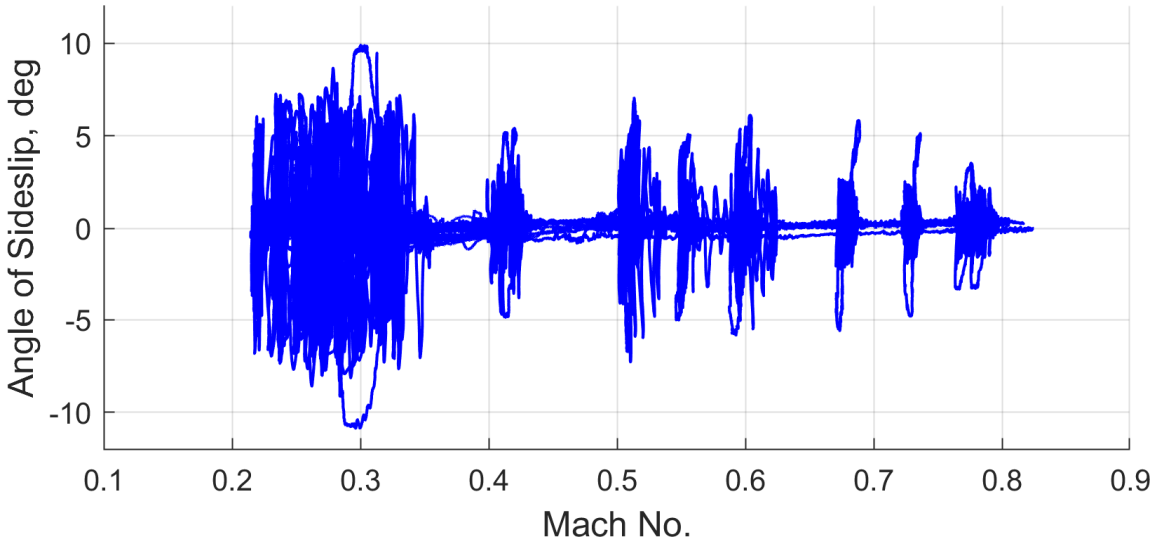

Figure 4: Angle of sideslip vs. Mach No. for the total analyzed flight test data.

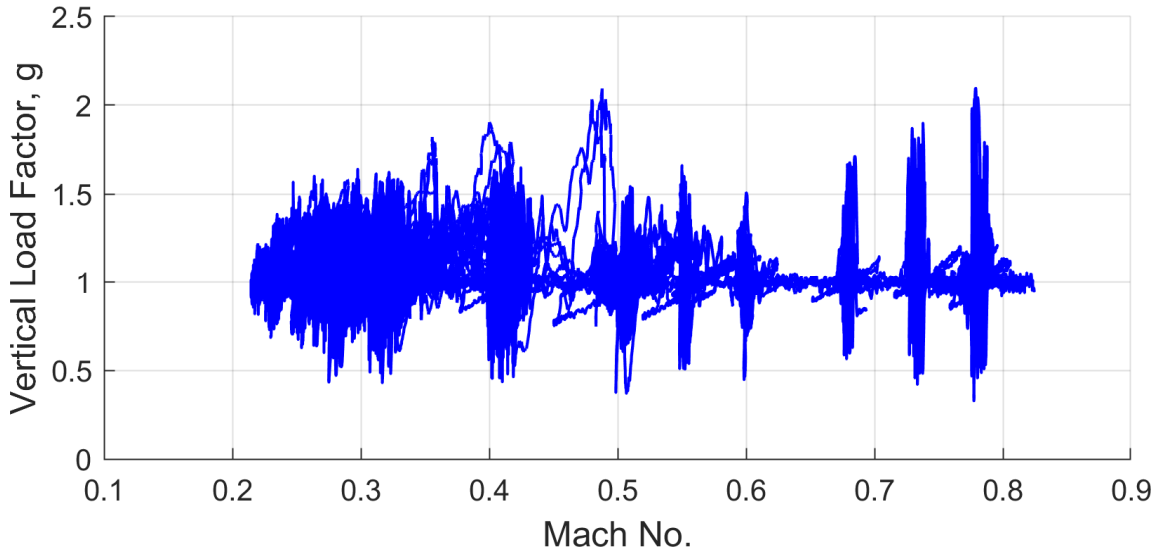

Figure 5: Vertical load factor vs. Mach No. for the total analyzed flight test data.

2.2. Maneuvers

The independent excitation of the aircraft motion modes is the central objective of the system identification maneuvers. For longitudinal motion these excitation maneuvers included 13211-step inputs on the elevator as well as small step inputs followed by a long time for the free reaction to observe the Phugoid motion. Doublet step input excitations were also applied on the thrust lever and on the horizontal stabilizer input. For the identification of their effectiveness, the airbrakes were deflected and retraced in a controlled manner. The lateral maneuvers included bank-to-bank turns, aileron and rudder doublets as well as steady heading sideslip maneuvers. At some TPs combined maneuvers like a 13211-elevator step input with a constant 30 deg bank angle were performed. A detailed description of the flight test program and the maneuvers can be found in the flight test request [20].

For the evaluation of the nose boom static pressure measurement, tower fly-bys were included in the flight test program. During these maneuvers the aircraft flew at an of altitude of 150 – 200 ft AGL near the tower in a level flight condition at a defined constant speed. The nose boom static pressure was compared to the one measured with calibrated pressure sensor on the airport tower.

Another part of the flight test program were acceleration and deceleration flights at a constant defined altitude. These have not been used in the system identification process, however they are planned to be considered in more detailed analysis of the aircraft lift curve and drag polar.

All planned and performed test maneuver are compiled in the overview presented in Table 2. It shows velocity, altitude, configuration and the excitation maneuvers considered for specified test point. All test points marked in green were flown during the flight test campaign, whereas the ones marked yellow are planned for an additional campaign in 2024. The rows marked in light green show test points were the yaw damper of the aircraft was forgotten to be turned off. There these maneuvers were not used in the system identification process as they do not contain the aircraft free reaction to the excitation. However, these maneuvers may be used in a later process for tuning the yaw damper of the simulation model.

Table 2: Planned and flown excitation maneuvers for the system identification flight test campaign.

No.	FTP	Alt. [ft]	VIAS [kt]	Ma	SF	Gear	Longitudinal Maneuvers							Lateral Maneuvers					Priority
							Elevator-13211	Elevator Pulse	Stabilizer Doublet	Thrust Doublet	AB-Ext. / Retr.	Elevator Frequency Sweep	Bank to Bank	Aileron Doublet	Rudder Doublet w/o	Rudder Doublet w. Damper	Steady Heading Sideslip	Const. Turn w. Elev-13211	
1	1c	11000	145	0.27	CLEAN	UP	X	X	X	X	-	-	X	X	X	X	X	-	I
2	1b	11000	135	0.25	1	UP	X	-	X	X	-	-	X	X	X	X	X	-	I
3	1b	11000	135	0.25	2	UP	X	-	X	X	-	-	X	X	X	X	X	-	I
4	1a	11000	120	0.22	3	UP	X	-	X	X	-	-	X	X	X	X	X	-	I
5	1d	11000	150	0.28	CLEAN	DOWN	X	X	X	X	-	-	X	X	X	-	X	-	I
6	1c	11000	145	0.27	1	DOWN	X	-	-	-	-	-	X	X	X	-	X	-	II
7	1b	11000	135	0.25	2	DOWN	X	-	-	-	-	-	X	X	X	-	X	-	II
8	1a	11000	120	0.22	3	DOWN	X	-	-	-	-	-	X	X	X	-	X	-	II
9	2	11000	170	0.32	CLEAN	UP	X	X	X	X	X	-	X	X	X	X	X	X	I
10	2	11000	170	0.32	1	UP	X	-	X	X	X	-	X	X	X	X	X	X	II
11	2	11000	170	0.32	2	UP	X	-	X	X	X	-	X	X	X	X	X	X	II
12	2	11000	170	0.32	3	UP	X	-	X	X	X	-	X	X	X	X	X	X	II
13	2	11000	170	0.32	CLEAN	DOWN	X	X	X	X	X	-	X	X	X	-	X	-	I
14	2	11000	170	0.32	1	DOWN	X	-	-	-	X	-	X	X	X	-	X	-	III
15	2	11000	170	0.32	2	DOWN	X	-	-	-	X	-	X	X	X	-	X	-	III
16	1d	11000	150	0.28	3	DOWN	X	-	-	-	X	-	X	X	X	-	X	-	III
17	3	11000	220	0.41	CLEAN	UP	X	X	X	X	X	-	X	X	X	X	X	X	I
18	3	11000	220	0.41	CLEAN	DOWN	X	-	X	X	X	-	X	X	X	X	X	X	I
19	4	11000	270	0.50	CLEAN	UP	X	X	X	X	X	-	X	X	X	-	X	X	I
20	5	11000	320	0.59	CLEAN	UP	X	-	X	X	X	-	X	X	X	-	X	X	I
21	6	20000	320	0.69	CLEAN	UP	X	-	X	X	-	-	X	X	X	-	X	X	II
22	7	27000	320	0.79	CLEAN	UP	X	X	X	X	-	X	X	X	X	-	X	X	I
23	8	27000	220	0.56	CLEAN	UP	X	X	X	X	-	-	X	X	X	-	X	X	I
24	9	33000	300	0.84	CLEAN	UP	X	X	X	X	-	X	X	X	X	-	X	X	I
25	10	37000	260	0.80	CLEAN	UP	X	X	X	X	-	-	X	X	X	-	X	X	I
26	11	37000	240	0.75	CLEAN	UP	X	-	X	X	-	-	X	X	X	-	X	X	I
27	12	37000	220	0.69	CLEAN	UP	X	-	X	X	-	X	X	X	X	-	X	X	I
28	13	37000	190	0.60	CLEAN	UP	X	-	X	X	-	-	X	X	X	-	X	X	II
29	14	37000	160	0.51	CLEAN	UP	X	X	X	X	-	X	X	X	X	-	X	X	I
30	15	45000	210	0.78	CLEAN	UP	X	X	X	X	-	X	X	X	X	-	X	X	II

To Do | Done | Yaw Damper On | Planned for 2025

3. Aircraft Geometry

3.1. Coordinate Frames

3.1.1. Geometric Reference Frame

For the specification of geometric positions, a reference coordinate frame was defined shown in Figure 6. Its origin is located 0.1435 m behind the aircraft nose with the XY-plane on the fuselage horizontal reference line. The X-axis is pointing in flight direction, the Y-axis is pointing to RH side and the Z-axis is pointing downward. This coordinate frame is also used for the definition of the aircraft CG position and the moment reference point.

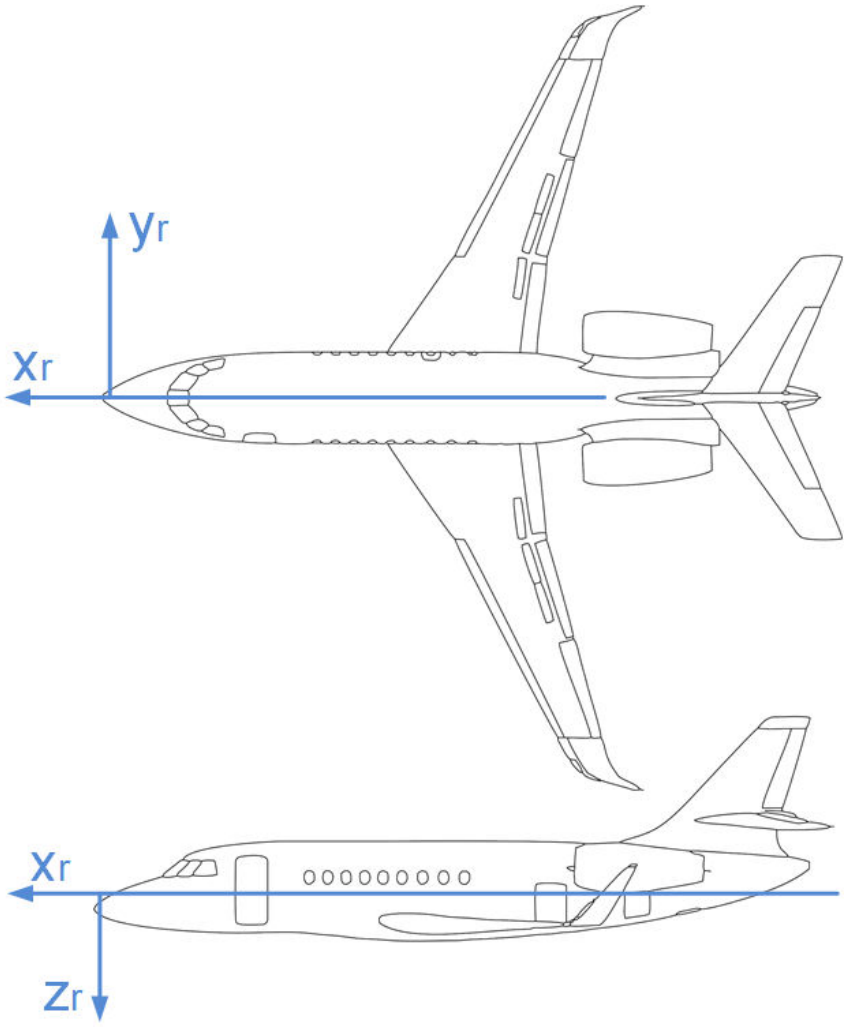

Figure 6: Reference coordinate frame for geometric positions.

3.1.2. Body-fixed, Aerodynamic and Experimental Coordinate Frames

Different coordinate systems are used to define the direction of forces, moments, and velocities for the flight dynamics model. The equations of motion, which are a fundamental part of the simulation model, are usually formulated in a body-fixed system, while the aerodynamic forces and moments acting on the aircraft are determined in the experimental coordinate system. Figure 7 shows the definition of body-fixed, the experimental and the aerodynamic coordinate system.

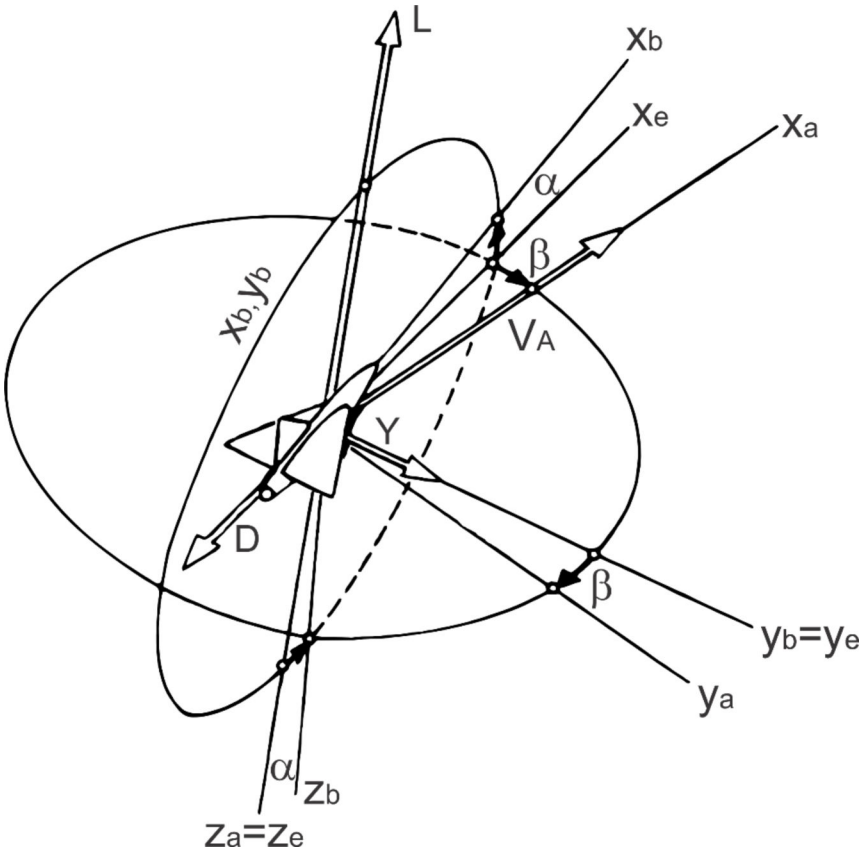

Figure 7: Body fixed, experimental and aerodynamic coordinate systems.

The origin of all coordinate systems is at the aircraft center of gravity. The directions of the body-fixed frame axes are parallel to those defined for the geometric reference frame shown in Figure 6. However, the origin is at the current CG position. The direction of the aerodynamic x-axis x_a is determined by the aerodynamic velocity vector V_A. The body-fixed and aerodynamic frames differ from each other by a rotation about the angle of attack α and the angle of sideslip β. The direction of the experimental x-axis x_e is determined by the projection of the aerodynamic velocity vector onto the body-fixed plane x_b, y_b. The system identification process determines the aerodynamic forces and moments in the represented experimental frame. This model formulation is also important for the aerodynamic model parameters which are defined in the experimental coordinate frame.

3.2. Geometric Dimensions and Control Surfaces

Table 3 in this section contains all geometric quantities used in the description of flight dynamic model. It contains also the reference areas and lengths used for the determination of the aerodynamic forces and moments.

Table 3: Geometric dimensions, positions and lengths for the Dassault Falcon 2000LX – ISTAR.

General Reference Quantities

Wing Reference Area S_{ref} [m²]	49.000
Reference Length l_μ [m]	2.888

Aerodynamic Moment Reference Point

X-Coord. in the reference frame $x_{RP,r}$ [m]	-9.883
Y-Coord. in the reference frame $y_{RP,r}$ [m]	0.000
Z-Coord. in the reference frame $z_{RP,r}$ [m]	-0.240

Fuselage

Length [m]	20.230
Diameter [m]	2.500

Wing

Span b [m]	21.380
Wing Area [m²]	40.300
Aspect Ratio Λ	9.100
Mean Aerodynamic Chord (MAC) Length [m]	2.888
Inner Wing Chord Length [m]	4.079
Outer Wing Chord Length [m]	1.120
Taper Ratio	0.220
Wing Sweep - Leading Edge [deg]	35 (internal) 27.6 (external)
Wing Sweep - Trailing Edge [deg]	6.4 (internal) 15.6 (external)
Wing Dihedral [deg]	0° 30'
X-Coordinate of MAC Beginning $x_{MAC,r}$ [m]	-9.306

Horizontal Tail

Horizontal Tail Area [m²]	13.300
Horizontal Tail Mean Aerodynamic Chord Length [m]	1.792
Taper Ratio	0.500
Aspect Ratio	4.500
Sweep (Leading Edge) [deg]	36.100
Sweep (Trailing Edge) [deg]	23.700
Negative Dihedral [deg]	8.000
X-Coordinate Reference Point $x_{RP,HT,r}$ [m]	-17.822
Z-Coordinate Reference Point $z_{RP,HT,r}$ [m]	-1.723

Vertical Tail

Vertical Tail Area [m²]	8.700
Vertical Tail Mean Aerodynamic Chord Length [m]	2.551
Sweep (Leading Edge) [deg]	43.600
Sweep (Trailing Edge) [deg]	17.000
Taper Ratio	0.320
Aspect Ratio	1.600

Configuration and Control Deflections

Slat / Flap Configurations δ_{SF}	SF0: flaps 0 deg, automatic slats extension SF1: flaps 10 deg, slats extended SF2: flaps 20 deg, slats extended SF3: flaps 40 deg, slats extended
Stabilizer i_{HT} Trim Deflection Limits	-10 deg / +2 deg
Elevator η Deflection Limits	- 20 deg / +16 deg
Aileron ξ Deflection Limits	+/- 25 deg
Rudder ζ Deflection Limits	+/- 29 deg
Airbrakes δ_{AB}	0 – Retracted, 1 – Mid Deployment, 2 – Full Deployment
Landing Gear δ_{LG}	0 – Retracted, 0 - Extended

Propulsion

Tilt Angel σ_y [deg] Angle between x-body and the projection of the engine x-axis and the (x-body, z-body) plan; positive when the front of the engine goes upwards.	1.9000
Kink Angle σ_z [deg] Angle between x-body and the projection of the engine x-axis and the (x-body, y-body) plan; positive when the front of the right engine goes towards the right.	2.3000
LH Engine No. 1 Thrust Point X-Coord. $x_{E_{LH},r}$ [m]	-15.8111
LH Engine No. 1 Thrust Point Y-Coord. $y_{E_{LH},r}$ [m]	-1.6648
LH Engine No. 1 Thrust Point Z-Coord. $z_{E_{LH},r}$ [m]	-0.2600
RH Engine No. 2 Thrust Point X-Coord. $x_{E_{RH},r}$ [m]	-15.8111
RH Engine No. 2 Thrust Point Y-Coord. $y_{E_{RH},r}$ [m]	1.6648
RH Engine No. 2 Thrust Point Z-Coord. $z_{E_{RH},r}$ [m]	-0.2600

4. System Identification

4.1. Description

The so-called output error method was used to estimate the aerodynamic parameters. This method works in the time domain and compares the model outputs with the measured flight data [8]. Using a maximum likelihood optimization, the model parameters i.e. aerodynamic parameters were estimated in such a way that the model error is minimized. For this process the recorded flight maneuvers were used. The individual maneuver time slices are compiled for each aircraft configuration. Table 2 contains an overview of the maneuvers that were used in the system identification process.

An overview of the procedure used is shown in Figure 8. The measured control deflections, the engine thrust, the current position of the center of gravity, total weight and moments of inertia were used as input to the model. Using these inputs and the rigid body model states, the aerodynamic model calculated the forces and moments acting on the aircraft. The necessary state variables, such as e.g. the flight speed, were determined using the equations of motion. Numerical integration of the equations of motion lead to the resulting model states which were the input for the sensor models. The sensor models remained fixed and their properties were the result of the Resulting previously performed data compatibility check [17] [18]. The outputs of the sensor models were compared with measured flight data. In an iterative process the calculated model error was minimized by optimizing the model parameters. To do this, the structure and parameters of the aerodynamic model were adjusted accordingly.

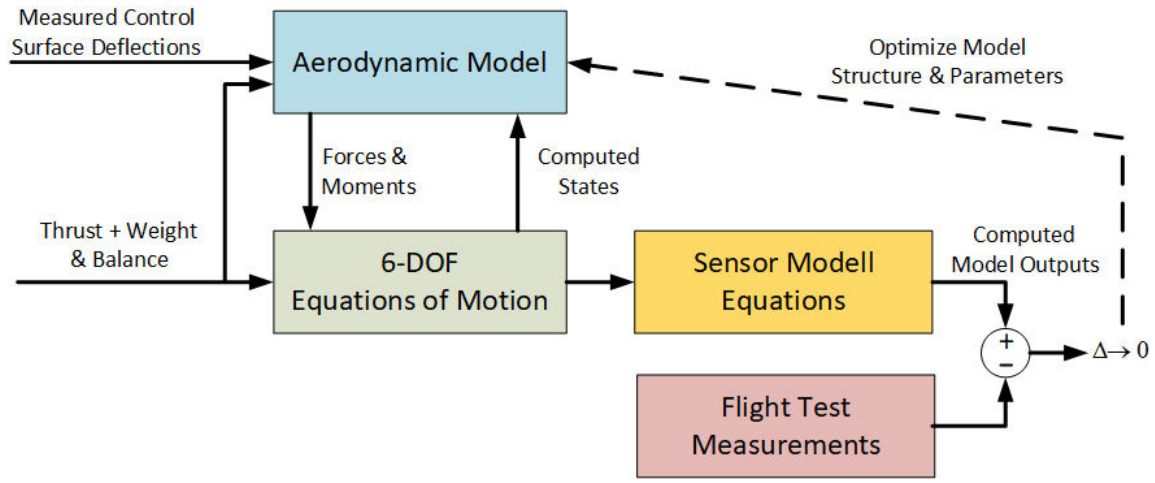

Figure 8: System identification process of the aerodynamic aircraft model.

4.2. Setup

The FITLAB software was used for system identification. It was implemented in MATLAB and the process shown in Figure 8: System identification process of the aerodynamic aircraft model. Figure 8 can be controlled and evaluated via a graphical user interface. The flight dynamics model is implemented in C++ and can be accessed via a compiled DLL from FITLAB. To make changes to the model structure and add parameters, the program code must be adapted accordingly and the DLL must be recompiled.

To estimate the aerodynamic parameters, input signals for the flight dynamics model must be defined. The input signals used and the associated model inputs are listed in Table 4. As already mentioned, when using the output error method, the measured flight data is compared with the model outputs. The output signals used are referred to as weighted channels, as they are used directly for the maximum likelihood optimization process, and are listed in Table 5. In addition to the weighted channels, the model also has other output signals that can used for evaluation purposes.

Table 4: Input signals used for the system identification process.

Ch. No.	Measured Input Signal	Model Input	Description	Unit
1	Elevator_pos_BASE	Elevator_pos_BASE	Elevator Deflection	deg
2	Aileron_LH_pos_BASE	Aileron_LH_pos_BASE	LH Aileron Deflection	deg
3	Aileron_RH_pos_BASE	Aileron_RH_pos_BASE	RH Aileron Deflection	deg
4	Rudder_pos_BASE	Rudder_pos_BASE	Rudder Deflection	deg
5	Stabilizer_pos_CSIONE	Stabilizer_pos_CSIONE	Horiz. Stabilizer Deflection	deg
6	AB_State	AB_State	Airbrake State	-
7	FL_State	FL_State	Flap/Slat Configuration	-
8	Gears_DOWN_CSITWO	Gears_DOWN_CSITWO	Landing Gear State	-
9	THRUST_ENG1	THRUST_ENG1	LH Engine Thrust Force	N
10	THRUST_ENG2	THRUST_ENG2	RH Engine Thrust Force	N
11	TOTAL_Weight	TOTAL_Weight	Total Aircraft Weight	kg
12	CG_X	CG_X	CG Position X-Coord.	m
13	CG_Y	CG_Y	CG Position Y-Coord.	m
14	CG_Z	CG_Z	CG Position Z-Coord.	m
15	I_XX	I_XX	I_XX Moment of Inertia	kgm²
16	I_YY	I_YY	I_YY Moment of Inertia	kgm²
17	I_ZZ	I_ZZ	I_ZZ Moment of Inertia	kgm²
18	I_XZ_cor	I_XZ	I_XZ Moment of Inertia (positive sign!)	kgm²
19	p_s_true_NB	p_s_true_NB	Nose Boom Static Pressure	mbar
20	p_t_true_NB	p_t_true_NB	Nose Boom Total Pressure	mbar

Ch. No.	Measured Input Signal	Model Input	Description	Unit
21	T_s_NB	T_s_NB	Nose Boom Static Temperature	deg C
22	Radio_Alt_LH_GIO_1	Radio_Alt_LH_GIO_1	Radio Altitude	m
23	Not Used (Zero Signal)	PSI_W	Wind Direction	deg
24	Not Used (Zero Signal)	V_W	Wind Speed	m/s

Table 5: Weighted channel outputs used for the system identification process.

Ch. No.	Measured Output	Model Output	Unit	Description
1	ax_IRS3	ax_IRS3_sim	g	Body-fixed longitudinal acceleration.
2	ay_IRS3	ay_IRS3_sim	g	Body-fixed lateral acceleration.
3	az_IRS3	az_IRS3_sim	g	Body-fixed vertical acceleration.
4	p_IRS3	p_IRS3_sim	deg/s	Roll rate.
5	q_IRS3	q_IRS3_sim	deg/s	Pitch rate.
6	r_IRS3	r_IRS3_sim	deg/s	Yaw rate.
7	Phi_IRS3	Phi_IRS3_sim	deg	Roll angle.
8	Theta_IRS3	Theta_IRS3_sim	deg	Pitch angle.
9	Psi_IRS3_cor	Psi_IRS3_sim	deg	True heading.
10	Alt_p_NB	Alt_p_NB_sim	ft	Nose boom barometric altitude.
11	Mach_NB	Mach_NB_sim	-	Mach number.
12	TAS_NB	TAS_NB_sim	kt	True airspeed.
13	AOA_NB	AOA_NB_sim	deg	Angle of attack.
14	AOS_NB	AOS_NB_sim	deg	Angle of sideslip.
15	p_dot_IRS3	p_dot_IRS3_sim	deg/s²	Roll rate acceleration.
16	q_dot_IRS3	q_dot_IRS3_sim	deg/s²	Pitch rate acceleration.
17	r_dot_IRS3	r_dot_IRS3_sim	deg/s²	Yaw rate acceleration.

4.3. Pre-Processing

In order to successfully carry out the system identification, some of the necessary variables had to be calculated and pre-processed from the flight measurement data. The files with the measured flight data were supplemented with these variables or corrected at the input of the flight dynamics model. The following section provides an overview of the additions and corrections made.

4.3.1. Thrust Calculation

The engine thrust cannot be measured directly in flight. It must therefore be calculated using an engine model. For system identification, an engine model was created as a look-up table based on the model data provided by the manufacturer and listed in report [14]. The current Mach number, N1 and the barometric flight altitude are required as input variables for calculating the net thrust. The input signals used are listed in Table 6. The calculated net thrust for both engines was added to the flight data files as separate channels.

Table 6: Measured flight data signals used for the calculation of the engine thrust.

Measured Signal	Unit	Description
Mach_ADS1	-	Mach number.
Alt_p_ADS1	ft	Barometric altitude.
N1_comp_FADEC1	%	LH Engine compensated N1
N1_comp_FADEC2	%	RH Engine compensated N1

4.3.2. Weight and Balance Properties

The weight and the position of the center of gravity are important input parameters for the flight mechanics model. These parameters, as well as the moment of inertia, cannot be measured directly during the flight, but must be determined using models. The model required for this was provided by the aircraft manufacturer [14]. The total weight, current position of the center of gravity and the mass moment of inertia are determined from the zero-fuel weight and the current fuel content in the tanks. For each flight the zero fuel-weight and the zero-fuel CG position is needed for the weight and balance calculation. These values were taken from the weight and balance report which was compiled by the pilots before each flight. The required measurement signals and input variables are listed in Table 2. The mass properties were added to the flight measurement data files as individual signals.

Table 7: Measured flight data signals additional information needed for the weight and balance model.

Measured Signal	Unit	Description
LH_CircuitTotalFuelQTY_FQMC	kg	LH Fuel tank content.
RH_CircuitTotalFuelQTY_FQMC	kg	RH Fuel tank content.
theta_IRS1	deg	Pitch angle.
ZFW	kg	Zero-fuel weight.
CG_ZFW	% MAC	CG position at zero-fuel weight.

4.3.3. Control Surface Input Correction

Another important input signal for system identification is the deflection of the control surfaces. Unfortunately, these measurement signals could not be checked using the DCC methods. Errors in the measurement signals for the control surfaces were therefore only noticed after a closer analysis of the flight data. This primarily concerns the signals for the deflection of the ailerons. In flight mechanics, the aileron deflection is zero when the aileron coincides exactly with the wing profile. Normally, both ailerons are deflected downwards by +4.5 deg when the control horn is in the neutral position. However, when analyzing the take-off procedures, it was noticed that the ailerons both show a deflection of +1.5 downwards.

After reviewing the calibration logs [23], it was noticed that the position of the aileron at which the deflection coincides with the wing profile was apparently set to a reference value of -3 deg (deflection upwards). With an actual aileron deflection of +4.5 deg in the neutral position (steering wheel in the center), this would explain the +1.5 deg in the measurement data. However, the zero point (correspondence with the wing profile) would then be incorrect, resulting in an offset of +3 deg in the aileron deflection. Therefore, a value of + 3 deg must be added to the measurement signals of both ailerons. This correction was made at the input vector in the C++ program code of the flight mechanics model. For future flights with ISTAR, the calibration of the aileron measurement should be checked and corrected again.

Another correction that is made for all signals for the control surface deflections concerns the time delay between the deflection sensors and the flight data that is transmitted to the basic aircraft data bus. The potentiometers that measure the rudder deflections and the air data sensors of the nose mast are directly connected to the aircraft measurement system, while inertial data, such as accelerations and rotation rates, are transmitted on the bus. This leads to different signal latencies. Flight maneuvers in the longitudinal and lateral movement were selected for an estimate of these time delays. Using the output error method, an optimal value for the time delay of Δt = -0.0156 s was determined which was applied only for the measurement signal of the elevator, aileron and rudder deflections. The correction of the signals for the control surfaces was done directly in the C++ program code for the flight mechanics model.

5. Aircraft Model Formulation

The flight dynamics model is an essential part of the system identification process. This section contains the mathematical equations describing the model and explains the calculation and processing of the calculated forces and moments.

5.1. Equations of Motion

In this investigation the aircraft is considered as a rigid body. Its motion can be described by the following state equations of rigid body dynamics [3], [22]:

$$\begin{aligned}
\dot{u} &= -q\,w + r\,v - g_0 \sin\Phi + \frac{1}{m}(X_E + X_A) \\
\dot{v} &= -r\,u + p\,w + g_0 \cos\Phi \sin\Phi + \frac{1}{m}(Y_E + Y_A) \\
\dot{w} &= -p\,v + q\,u - g_0 \cos\Phi \cos\Phi + \frac{1}{m}(Z_E + Z_A)
\end{aligned} \qquad \begin{aligned} u(t_0) &= u_0 \\ v(t_0) &= v_0 \\ w(t_0) &= w_0 \end{aligned} \qquad \text{Eq. 1}$$

$$\begin{bmatrix} \dot{p} \\ \dot{q} \\ \dot{r} \end{bmatrix} = T_b^{-1} \left\{ \begin{bmatrix} L_A \\ M_A \\ N_A \end{bmatrix}_b + \begin{bmatrix} L_E \\ M_E \\ N_E \end{bmatrix}_b - \begin{bmatrix} qr(I_{zz} - I_{yy}) - pqI_{xz} \\ rp(I_{xx} - I_{zz}) + (p^2 - r^2)I_{xz} \\ pq(I_{yy} - I_{xx}) + qrI_{xz} \end{bmatrix}_b \right\} \qquad \text{Eq. 2}$$

$$T_b^{-1} = \begin{bmatrix} I_{xx} & 0 & -I_{xz} \\ 0 & I_{yy} & 0 \\ -I_{xz} & 0 & I_{zz} \end{bmatrix}_b^{-1} = \frac{1}{I_{yy}(I_{xx}I_{zz} - I_{xz}^2)} \begin{bmatrix} I_{yy}I_{zz} & 0 & I_{yy}I_{xz} \\ 0 & I_{xx}I_{zz} - I_{xz}^2 & 0 \\ I_{yy}I_{xz} & 0 & I_{xx}I_{yy} \end{bmatrix} \qquad \text{Eq. 3}$$

For the description of the aircraft attitude a quaternion formulation is used. The quaternions are determined with the following differential equations:

$$\begin{aligned}
\dot{q}_0 &= \frac{1}{2}(q_1 p + q_2 q + q_3 r) \\
\dot{q}_1 &= \frac{1}{2}(q_0 p - q_3 q + q_2 r) \\
\dot{q}_2 &= \frac{1}{2}(q_3 p + q_0 q - q_1 r) \\
\dot{q}_3 &= \frac{1}{2}(-q_2 p + q_1 q + q_0 r)
\end{aligned} \qquad \begin{aligned} q_0(t_0) &= (q_0)_0 \\ q_1(t_0) &= (q_1)_0 \\ q_2(t_0) &= (q_2)_0 \\ q_3(t_0) &= (q_3)_0 \end{aligned} \qquad \text{Eq. 4}$$

The initial values for the quaternion are calculated from the initial Euler angles with the following equation:

$$(q_0)_0 = \cos\left(\frac{\Phi_0}{2}\right)\cos\left(\frac{\Theta_0}{2}\right)\cos\left(\frac{\Psi_0}{2}\right) + \sin\left(\frac{\Phi_0}{2}\right)\sin\left(\frac{\Theta_0}{2}\right)\sin\left(\frac{\Psi_0}{2}\right)$$

$$(q_1)_0 = \sin\left(\frac{\Phi_0}{2}\right)\cos\left(\frac{\Theta_0}{2}\right)\cos\left(\frac{\Psi_0}{2}\right) - \cos\left(\frac{\Phi_0}{2}\right)\sin\left(\frac{\Theta_0}{2}\right)\sin\left(\frac{\Psi_0}{2}\right)$$

$$(q_2)_0 = \cos\left(\frac{\Phi_0}{2}\right)\sin\left(\frac{\Theta_0}{2}\right)\cos\left(\frac{\Psi_0}{2}\right) + \sin\left(\frac{\Phi_0}{2}\right)\cos\left(\frac{\Theta_0}{2}\right)\sin\left(\frac{\Psi_0}{2}\right) \quad \text{Eq. 5}$$

$$(q_3)_0 = \cos\left(\frac{\Phi_0}{2}\right)\cos\left(\frac{\Theta_0}{2}\right)\sin\left(\frac{\Psi_0}{2}\right) - \sin\left(\frac{\Phi_0}{2}\right)\sin\left(\frac{\Theta_0}{2}\right)\cos\left(\frac{\Psi_0}{2}\right)$$

$$\Phi_0 = \Phi(t_0),\ \Theta_0 = \Theta(t_0),\ \Psi_0 = \Psi(t_0)$$

For practical applications and comparison with sensor measurements, the Euler angles can be obtained from the following transformation equations:

$$\varphi = \operatorname{atan2}\left(\frac{2(q_2q_3 + q_0q_1)}{q_0^2 - q_1^2 - q_2^2 + q_3^2}\right)$$

$$\theta = -\operatorname{asin}\left(2(q_1q_3 - q_0q_2)\right) \quad \text{Eq. 6}$$

$$\psi = \operatorname{atan2}\left(\frac{2(q_1q_2 + q_0q_3)}{q_0^2 + q_1^2 - q_2^2 - q_3^2}\right)$$

The aircraft altitude is determined with the following differential equation:

$$\dot{h} = u\sin\Theta - v\sin\Phi\cos\Theta - w\cos\Phi\cos\Theta \quad \text{Eq. 7}$$

For the system identification process most of the maneuvers analyzed already during the DCC [18] were used. During the DCC process the initial values for the states, indicated by the subscript '0' in the above-mentioned equations, were determined for each maneuver time slice. These results were reused again as initial states for the system identification process.

The state variables $(u, v, w, p, q, r, q_0, q_1, q_2, q_3, h)$ were determined through numerical integration of the equations of motion using a fourth-order Runge-Kutta method. The integration step size used for the system identification process was 25 Hz.

5.2. Body-Fixed Forces and Moments

Forces and moments acting on the aircraft rigid body are the necessary input values for solving the equations of translational Eq. 1 and rotational motion Eq. 2. This section explains the transformations and procedures necessary to calculate the aerodynamic and engine forces and moments. During takeoff and landing, the landing gear exerts additional forces and moments on the aircraft body, but these have not been considered in this system identification campaign. The aerodynamic effects caused by the deployment/retraction of the landing gear are considered by the aerodynamic model formulation. Note that reference areas and lengths as well as positions used in the equations are listed in Table 3.

5.2.1. Aerodynamic Forces and Moments

The body-axis longitudinal, lateral and vertical aerodynamic forces X_A, Y_A and Z_A are obtained with through

$$\begin{aligned} X_A &= \bar{q}\, S_{ref}\, C_X \\ Y_A &= \bar{q}\, S_{ref}\, C_Y \\ Z_A &= \bar{q}\, S_{ref}\, C_Z\,. \end{aligned} \qquad \text{Eq. 8}$$

The dynamic pressure is calculated from the static air pressure and the current Mach number

$$\bar{q} = \frac{1}{2} p_s \kappa M a^2. \qquad \text{Eq. 9}$$

The body-fixed force coefficients C_X and C_Z are calculated by the following transformation:

$$\begin{aligned} C_X &= +C_L \sin\alpha - C_D \cos\alpha \\ C_Z &= -C_L \cos\alpha - C_D \sin\alpha \end{aligned} \qquad \text{Eq. 10}$$

where C_L, $C_D$and C_Y are the lift, drag and side force coefficients in the experimental coordinate system described in Chapter 3.1.2. The aerodynamic moments L_A, M_A and N_A are referred to the center of gravity and are given by

$$\begin{aligned} L_A &= \bar{q}\, S_{ref}\, \bar{c}\, C_{l_{CG}} \\ M_A &= \bar{q}\, S_{ref} l_\mu C_{m_{CG}} \\ N_A &= \bar{q}\, S_{ref}\, \bar{c}\, C_{n_{CG}} \end{aligned} \qquad \text{Eq. 11}$$

with the half wing span $\bar{c} = \frac{b}{2}$.

The CG referred rolling, pitching and yawing moment coefficients $C_{l_{CG}}$, $C_{m_{CG}}$ and $C_{n_{CG}}$in the body-fixed system are calculated as follows:

$$\begin{aligned} C_{l_{CG}} &= C_{l_{RP}} + \frac{1}{\bar{c}}\left(C_Z\, y_{RP,CG} - C_Y\, z_{RP,CG}\right) \\ C_{m_{CG}} &= C_{m_{RP}} + \frac{1}{l_\mu}\left(-C_Z\, x_{RP,CG} + C_X\, z_{RP,CG}\right) \\ C_{n_{CG}} &= C_{n_{RP}} + \frac{1}{\bar{c}}\left(C_Y\, x_{RP,CG} - C_X\, z_{RP,CG}\right) \end{aligned} \qquad \text{Eq. 12}$$

The variables $C_{l_{RP}}$, $C_{m_{RP}}$and $C_{n_{RP}}$ are the moment coefficients in the body-fixed system referred to the aerodynamic moment reference point defined in Table 3. For the transformation of the moment coefficients the distances between the reference point and the CG position $x_{RP,CG}$, $y_{RP,CG}$ and $z_{RP,CG}$need to determine with the following equations:

$$\begin{aligned} x_{RP,CG} &= x_{RP,r} - x_{CG,r} \\ y_{RP,CG} &= y_{RP,r} - y_{CG,r} \\ z_{RP,CG} &= z_{RP,r} - z_{CG,r} \end{aligned} \qquad \text{Eq. 13}$$

$x_{RP,r}$, $y_{RP,r}$ *and* $z_{RP,r}$ are coordinates of the moment reference point in the aircraft reference system as defined in Table 3. The aircraft CG position in the reference coordinate system ($x_{CG,r}, y_{CG,r}, z_{CG,r}$) are determined with the weight and balance described in Chapter 4.3.2.

The body-fixed moment coefficients $C_{l_{RP}}$, $C_{m_{RP}}$and $C_{n_{RP}}$ are determined from the coefficients in the experimental coordinate system using the following transformation:

$$\begin{aligned} C_{l_{RP}} &= C_{l_{RP,e}} \cos\alpha - C_{n_{RP,e}} \sin\alpha \\ C_{m_{RP}} &\widehat{=} C_{m_{RP,e}} \\ C_{n_{RP}} &= C_{l_{RP,e}} \sin\alpha + C_{n_{RP,e}} \cos\alpha \end{aligned} \qquad \text{Eq. 14}$$

The moment coefficients referred to the moment reference point in the experimental coordinate frame $C_{l_{RP,e}}, C_{m_{RP,e}}$ and $C_{n_{RP,e}}$ are the ones that are calculated with the aerodynamics model described in Chapter 6.

5.2.2. Forces and Moments generated by the Aircraft Engines

In addition to the aerodynamic forces, the forces and moments acting on the solid body from the engine are required to calculate the equations of motion. In chapter 3.1 it was already mentioned that the engine net thrust was calculated with a thrust model and added to the flight data. However, the thrust axes of the two engines are not aligned parallel to the solid axes. On the Dassault Falcon 2000LX ISTAR, the thrust axes of both engines are turned outwards. In the case of the right engine, the axis is rotated by σ_z =+2.3 deg in the xy-plane of the body-fixed coordinate system. For the left engine, the angle is correspondingly negative. The thrust axis of both engines is also inclined by σ_y =+1.9 deg. Consider the engine inclination and toe out engines, the net thrust force components for the LH and RH engine are determined in the body-fixed coordinate system by:

$$\begin{aligned} X_{E_{LH}} &= +F_{T_{LH}} \cos\sigma_y \cos\sigma_z \\ Y_{E_{LH}} &= +F_{T_{LH}} \cos\sigma_y \sin\sigma_z \\ Z_{E_{LH}} &= -F_{T_{LH}} \sin\sigma_y \\ X_{E_{RH}} &= +F_{T_{RH}} \cos\sigma_y \cos\sigma_z \\ Y_{E_{RH}} &= -F_{T_{RH}} \cos\sigma_y \sin\sigma_z \\ Z_{E_{RH}} &= -F_{T_{RH}} \sin\sigma_y \end{aligned} \qquad \text{Eq. 15}$$

$F_{T_{LH}}$ and $F_{T_{RH}}$ are the net thrust forces of the left and right engine calculated with the engine thrust model as explained in Chapter 4.3.1. The total resultant forces and moments acting on the rigid body are then determined with the following equations:

$$\begin{aligned} X_E &= X_{E_{LH}} + X_{E_{RH}} \\ Y_E &= Y_{E_{LH}} + Y_{E_{RH}} \\ Z_E &= Z_{E_{LH}} + Z_{E_{LH}} \end{aligned} \qquad \text{Eq. 16}$$

$$\begin{aligned} L_E &= \left(y_{E_{LH,CG}} Z_{E_{LH}} - z_{E_{LH,CG}} X_{E_{LH}}\right) + \left(y_{E_{RH,CG}} Z_{E_{RH}} - z_{E_{RH,CG}} X_{E_{RH}}\right) \\ M_E &= \left(z_{E_{LH,CG}} X_{E_{LH}} - x_{E_{LH,CG}} Z_{E_{LH}}\right) + \left(z_{E_{RH,CG}} X_{E_{RH}} - x_{E_{RH,CG}} Z_{E_{RH}}\right) \\ N_E &= \left(x_{E_{LH,CG}} Y_{E_{LH}} - y_{E_{LH,CG}} X_{E_{LH}}\right) + \left(x_{E_{RH,CG}} Y_{E_{RH}} - y_{E_{RH,CG}} X_{E_{RH}}\right) \end{aligned} \qquad \text{Eq. 17}$$

where $x_{E_{LH/RH,CG}}$, $y_{E_{LH/RH,CG}}$ and $z_{E_{LH/RH,CG}}$ refer to the current distances between the aircraft CG and the engine thrust point location. They are determined with the following equation:

$$\begin{aligned} x_{E_{LH/RH,CG}} &= x_{E_{LH/RH,r}} - x_{CG,r} \\ y_{E_{LH/RH,CG}} &= y_{E_{LH/RH,r}} - y_{CG,r} \\ z_{E_{LH/RH,CG}} &= z_{E_{LH/RH,r}} - z_{CG,r} \end{aligned} \qquad \text{Eq. 18}$$

The positions of the left and right engine are listed in Table 3, whereas the location of the current aircraft CG is taken from the calculated flight as explained in Chapter 4.3.2.

6. Aerodynamic Model

The following chapter describes the structure of the identified aerodynamic model for the Dassault Falcon 2000LX ISTAR aircraft. The modeling approach is explained and the model equations with the parameters used are listed.

6.1. Modelling Approach and Implementation

The aerodynamic model is founded upon the existing knowledge and experience of the DLR Institute of Flight Systems in the field of aircraft system identification [8], [9]. The objective of the modeling approach was to develop a comprehensive flight dynamics model that could be utilized across the entire flight envelope. The specific characteristics of the ISTAR aircraft, including its T-tail configuration and rear engine installation, were considered.

A mathematical expression was developed for each individual aerodynamic force and moment coefficient. The initial model formulation was relatively simple, comprising only a few parameters. In a step-by-step process, the equations were expanded with additional model parameters in order to enhance the model's precision. For instance, non-linear model terms were incorporated with respect to the dependency of the model on Mach number.

A two-point aerodynamic model was employed for the purpose of modeling the longitudinal aircraft motion [16]. In this model, the aerodynamic flow conditions on the wing and horizontal tail are considered separately. As a consequence, the aerodynamic forces exerted by the wing and fuselage are modelled separately.

The aerodynamic model is implemented as a C++ class object and was compiled as a DLL for the system identification process with FITLAB. It is also possible to compile the model as an S-function and utilize it in MATLAB Simulink. The simulation model can then be employed in the AVES Simulator, for instance. The procedure for compiling the model is explained in more detail in the DLR Wiki and can be found under following address:
https://wiki.dlr.de/display/FDSimfw/Aerodynamic+Model+-+Update+of+the+Equations+and+Re-Compiling+as+S-Function

6.2. Model Utilization

The identified aerodynamic model is based on the flight data used for this purpose, which are listed in Chapter 2.2. The model is therefore only sufficiently accurate for the flight range where identification was possible. The flight behavior in the areas where no flight data was available for the system identification is therefore not or only partially depicted with the present model version. At present, this mainly concerns the behavior during stall or in ground effect during take-off and

landing. This must be considered when using the model and evaluating the generated simulation data. The dataset with the identified aerodynamic parameters for each slat/flap configuration can be found in the second part of the report [19].

6.3. Control Surfaces

The Dassault Falcon 2000LX ISTAR has several aerodynamically effective control surfaces. These measured variables were initially corrected according to the procedure described in Chapter 4.3.3. Table 8 contains the unit and description of the variables used in the formulation of the aerodynamic model. In addition to the control surfaces, there are secondary control systems that affect the aerodynamic characteristics of the aircraft, which are listed in Table 9. No time delay correction was performed for these systems.

Table 8: Control surface deflections used in the aerodynamic model.

Symbol	Unit	Description
η	rad	Elevator deflection
$\xi = \frac{1}{2}(\xi_{RH} - \xi_{LH})$	rad	Aileron deflection
ζ	rad	Rudder deflection

Table 9: Secondary aerodynamic surface used in the aerodynamic model.

Symbol	Unit	Description
i_{HT}	rad	Horizontal stabilizer deflection
δ_{AB}	-	Airbrake condition: 0 – Retracted 1 – Mid Deployment 2 – Full Deployment
δ_{LG}	-	Landing gear condition: 0 – Retracted 1 – Extended
δ_{SF}	-	Slat / Flap condition: 0 - flaps 0 deg, automatic slats extension 1 - flaps 10 deg, slats extended 2 - flaps 20 deg, slats extended 3 - flaps 40 deg, slats extended

6.4. Aerodynamic Flow Variables

For the calculation of aerodynamic forces and moments quantities describing the aerodynamic characteristics need to be determined. The true airspeed V_{TAS} at the center of gravity is calculated from the body-fixed velocity components:

$$V_{TAS} = \sqrt{u^2 + v^2 + w^2} \quad \text{Eq. 19}$$

The angle of attack and the angle of sideslip are determined with

$$\alpha = atan2\left(\frac{w}{u}\right) \quad \text{Eq. 20}$$

$$\beta = \text{asin}\left(\frac{v}{V_{TAS}}\right) \quad \text{Eq. 21}$$

The Mach number is determined from the static and total air pressure:

$$Ma = \sqrt{5\left(\frac{p_t}{p_s}\right)^{\frac{2}{7}} - 1} \quad \text{Eq. 22}$$

6.5. Prandtl-Glauert Effects

As the Mach number increases, compressibility effects begin to influence its aerodynamic properties. The Prandtl-Glauert transformation enables the correction of incompressible aerodynamic parameters $C_{(.)}$ for effects associated with the Mach number ($Ma > 0.7$). The general equation is as follows:

$$C_{(.)}(Ma) = \frac{C_{(.)}}{\sqrt{1 - PG_{C_{(.)}} Ma^2}} \quad \text{Eq. 23}$$

6.6. Engine Thrust Coefficient

During the system identification process some aerodynamic effect showed a dependency on the engine thrust. CFD calculations confirmed that there is a slight influence on the fuselage and the wing caused by the engine inflow. This effect is modelled using the engine thrust coefficient being determined with the following equation:

$$\delta_{T_{LH/RH}} = \frac{F_{T_{LH/RH}}}{\bar{q}\, S_{ref}} \quad \text{Eq. 24}$$

6.7. Lift Coefficient

The lift coefficient C_L is described by a two-point model consisting of the wing body and horizontal tail components:

$$C_L = C_{L,WB} + C_{L,HT}\frac{S_{HT}}{S_{ref}}\cos\left(\alpha_{dyn} - \epsilon_{HT}\right) \quad \text{Eq. 25}$$

where the wing body contribution (including compressibility correction) is given as:

$$\begin{aligned} C_{L,WB} = {} & \frac{C_{L0}}{\sqrt{1 - PG_{CL_0}Ma^2}} + \left(\frac{C_{L\alpha,WB}}{\sqrt{1 - PG_{C_{L\alpha,WB}}Ma^2}}\right)\alpha \\ & + C_{L\beta^2}\beta^2 \\ & + \left(C_{L\delta_{AB}} + C_{L\delta_{AB}\alpha}\alpha\right)\delta_{AB} \\ & + C_{L\delta_{LG}}\delta_{LG} \\ & + C_{L\delta_T}\left(\delta_{T_{LH}} + \delta_{T_{RH}}\right) \end{aligned} \quad \text{Eq. 26}$$

The horizontal tail lift contribution $C_{L_{HT}}$ is determined with:

$$C_{L,HT} = C_{L0,HT} + \left(\frac{C_{L\alpha,HT}}{\sqrt{1 - PG_{CL_{\alpha,HT}}Ma^2}}\right)\alpha_{HT} + C_{L\eta}\eta \quad \text{Eq. 27}$$

where the angle of attack at the horizontal tail $\alpha_{HT}$is given by:

$$\alpha_{HT} = \alpha + \alpha_{dyn} + i_{HT} - \epsilon_{HT} \quad \text{Eq. 28}$$

and the downwash angle at the horizontal tail ϵ_{HT} is:

$$\epsilon_{HT} = \epsilon_{0,HT} + \frac{\partial\epsilon_{HT}}{\partial\alpha}\alpha(t - \Delta t) \quad \text{Eq. 29}$$

The time delay is given by

$$\Delta t = \frac{r^*_{HT}}{V_{TAS}} \quad \text{Eq. 30}$$

which represents the time interval of the flow from the wing to the horizontal tail. The distance between the aerodynamic reference and the reference point of horizontal tail r_{HT}^{*} can be determined from the neutral point positions listed in Table 3 with the following equation:

$$r_{HT}^{*} = x_{RP,r} - x_{RP,HT,r} \qquad \text{Eq. 31}$$

The dynamic angle of attack α_{dyn} is determined from

$$\alpha_{dyn} = arctan\left(\frac{q\, r_{HT}}{V_{TAS}}\right) \qquad \text{Eq. 32}$$

with r_{HT} being the distance between the current aircraft CG position and the reference point of the horizontal tail, obtained from

$$r_{HT} = x_{CG,r} - x_{RP,HT,r} \qquad \text{Eq. 33}$$

The downwash angle for the case $\alpha = 0$ is determined with:

$$\epsilon_{0,HT} = \frac{C_{L0}}{C_{L\alpha,WB}} \frac{\partial \epsilon_{HT}}{\partial \alpha} \qquad \text{Eq. 34}$$

6.8. Drag Coefficient

The drag coefficient C_D is determined with a standard quadratic drag polar equation, horizontal tail effects and additional linear and nonlinear terms covering the effects of the control surfaces, airbrakes and landing gear extension:

$$\begin{aligned} C_D = & \left(\frac{C_{D0}}{\sqrt{1 - PG_{D0}Ma^2}}\right) \\ & + \frac{C_L^2}{e\pi\Lambda} \\ & - C_{L,HT}\frac{S_{HT}}{S_{ref}}\sin\left(\alpha_{dyn} - \epsilon_{HT}\right) \\ & + C_{D\beta^2}\beta^2 \\ & + \left(C_{D\delta_{AB}} + C_{D\delta_{AB\alpha}}\alpha\right)\delta_{AB} \\ & + C_{D\delta_{LG}}\delta_{LG} \\ & + C_{D\delta_T}\left(\delta_{T_{LH}} + \delta_{T_{RH}}\right) \end{aligned} \qquad \text{Eq. 35}$$

6.9. Pitch Moment Coefficient

A combination of stabilizing and controlling effects of the horizontal tail, wing contributions like pitch damping and airbrake and sideslip effects are determining the pitch moment coefficient $C_{m,RP}$ about the aerodynamic reference point:

$$\begin{aligned} C_{m,RP} = \; & C_{m0,WB} \\ & + C_{L,HT}\frac{S_{HT}}{S_{ref}}\frac{r_{HT}^{*}}{l_{\mu}}\left(-\cos\left(\alpha_{dyn}-\epsilon_{HT}\right)\right) \\ & - C_{L,HT}\frac{S_{HT}}{S_{ref}}\frac{z_{HT}^{*}}{l_{\mu}}\sin\left(\alpha_{dyn}-\epsilon_{HT}\right) \\ & + C_{mq,WB}\frac{q l_{\mu}}{V_{TAS}} \\ & + C_{m\beta^2}\beta^2 \\ & + \left(C_{m\delta_{AB}} + C_{mq\delta_{AB}\alpha}\alpha + C_{m\delta_{AB}q}\frac{q l_{\mu}}{V_{TAS}}\right)\delta_{AB} \\ & + \left(C_{m\delta_{LG}} + C_{mq\delta_{LG}}\frac{q l_{\mu}}{V_{TAS}}\right)\delta_{LG} \\ & + C_{m\delta_T}\left(\delta_{T_{LH}} + \delta_{T_{RH}}\right) \end{aligned} \qquad \text{Eq. 36}$$

with z_{HT}^{*}being the vertical distance between the aerodynamic and the horizontal tail reference point:

$$z_{HT}^{*} = z_{RP,r} - z_{RP,HT,r} \qquad \text{Eq. 37}$$

6.10. Side Force Coefficient

The side force coefficient C_Y is influenced by the angle of sideslip, the roll and yaw rate as well as various control deflections and is formulated as:

$$\begin{aligned} C_Y = \; & C_{Y0} \\ & + \left(C_{Y\beta} + C_{Y\beta\alpha}\alpha + C_{Y\beta Ma}Ma + C_{Y\beta\delta_{LG}}\delta_{LG}\right)\beta \\ & + \left(C_{Yp} + C_{Yp\alpha}\alpha + C_{Yp\delta_{LG}}\delta_{LG}\right)\frac{p\, l_\mu}{V_{TAS}} \\ & + \left(C_{Yr} + C_{Yr\alpha}\alpha + C_{Yr\delta_{AB}}\delta_{AB} + C_{Yr\delta_{LG}}\delta_{LG}\right)\frac{r\, l_\mu}{V_{TAS}} \\ & + C_{Y\xi}\,\xi \\ & + \left(C_{Y\zeta} + C_{Y\zeta\beta}\beta\right)\zeta \end{aligned} \qquad \text{Eq. 38}$$

6.11. Roll Moment Coefficient

Similar to the side force coefficient, the rolling moment coefficient $C_{l,RP}$ has various influences due to the roll and yaw rate as wells as control deflections, angle of sideslip and compressible flow. The rolling moment coefficient with respect to the aerodynamic reference point results as a sum of linear and non-linear terms given by:

$$\begin{aligned} C_{l,RP} = \; & C_{l0} \\ & + \left(C_{l\beta} + C_{l\beta\alpha}\alpha + C_{l\beta Ma}Ma + C_{l\beta\delta_{LG}}\delta_{LG}\right)\beta \\ & + \left(C_{lp} + C_{lp\alpha}\alpha + C_{lp\delta_{LG}}\delta_{LG} + C_{lpMa^2}Ma^2\right)\frac{p\, l_\mu}{V_{TAS}} \\ & + \left(C_{lr} + C_{lr\alpha}\alpha + C_{lr\delta_{AB}}\delta_{AB} + C_{lr\delta_{LG}}\delta_{LG} + C_{lrMa}Ma\right)\frac{r\, l_\mu}{V_{TAS}} \\ & + \left(C_{l\xi} + C_{l\xi\alpha}\beta + C_{l\xi Ma}Ma + C_{l\xi Ma^2}Ma^2\right)\xi \\ & + \left(C_{l\zeta} + C_{\zeta\alpha}\alpha + C_{Ma}\,Ma\right)\zeta \end{aligned} \qquad \text{Eq. 39}$$

6.12. Yaw Moment Coefficient

Like the other lateral aerodynamic coefficients, the yawing moment coefficient $C_{n,RP}$ is influences by the aircraft roll and yaw rate, control deflections, the sideslip angle and compressible flow. The yawing moment coefficient about the aerodynamic reference point is given by the following equation:

$$\begin{aligned} C_{n,RP} = \; & C_{n0} \\ & + \left(C_{n\beta} + C_{n\beta Ma} Ma + C_{n\beta\delta_{LG}} \delta_{LG}\right)\beta \\ & + \left(C_{np} + C_{np\alpha}\alpha + C_{np\delta_{LG}}\delta_{LG} + C_{npMa} Ma + C_{npMa^2} Ma^2\right)\frac{p\, l_\mu}{V_{TAS}} \\ & + \left(C_{nr} + C_{nr\alpha}\alpha + C_{nr\delta_{AB}}\delta_{AB} + C_{nr\delta_{LG}}\delta_{LG} + C_{nrMa} Ma + + C_{nrMa^2} Ma^2\right)\frac{r\, l_\mu}{V_{TAS}} \\ & + \left(C_{n\xi} + C_{n\xi\alpha}\,\alpha + C_{n\xi\beta}\,\beta + C_{n\xi Ma} Ma + C_{n\xi Ma^2} Ma^2\right)\xi \\ & + \left(\mathrm{C}_{l\zeta} + \mathrm{C}_{\zeta\alpha}\,\alpha + \mathrm{C}_{\zeta\beta}\,\beta\right)\zeta \end{aligned} \qquad \text{Eq. 40}$$

7. Model Evaluation

For an evaluation of the identified model, the measured flight data was compared with the model outputs. This chapter contains selected time history plots of flight maneuvers as well as cross plots of selected flight mechanical parameters that allow an evaluation of the model quality. For the most important flight parameters cross plots are presented for each flap/slat configuration showing the remaining model error versus the according flight measurement.

7.1. Longitudinal Maneuvers

Figure 9 and Figure 10 present time series plots of the longitudinal and lateral flight parameters for selected two 3211-elevator excitations, an elevator pulse, two stabilizer doublet inputs, and two airbrake extension maneuvers. The maneuvers were conducted at FETP No. 9 at an altitude of 11000 feet and a speed of 170 kt. The blue lines represent the measured data, while the red lines indicate the model output signals. In general, there is only a minimal discrepancy between the measurements and the model outputs. During the extension of the airbrakes, a peak is observed in the vertical acceleration a_z model output. This characteristic is associated with the discrete signal representing the airbrake state δ_{AB}, which is employed as an input to the model. In future model investigations, this signal should be modified to a more continuous signal that directly represents the deflection of the airbrake spoilers. During the elevator pulse maneuvers, a greater discrepancy is observed between the measured heading angle Ψ and the model output. Given the duration of this maneuver, which exceeds two minutes, external influences such as minor changes in wind direction and turbulence may result in a deviation from the measured heading over time. This potential issue could be mitigated through the implementation of an artificial stabilization controller during such prolonged maneuvers. However, the impact of this discrepancy on the overall identification results is minimal, and therefore, this solution was not incorporated into the investigation.

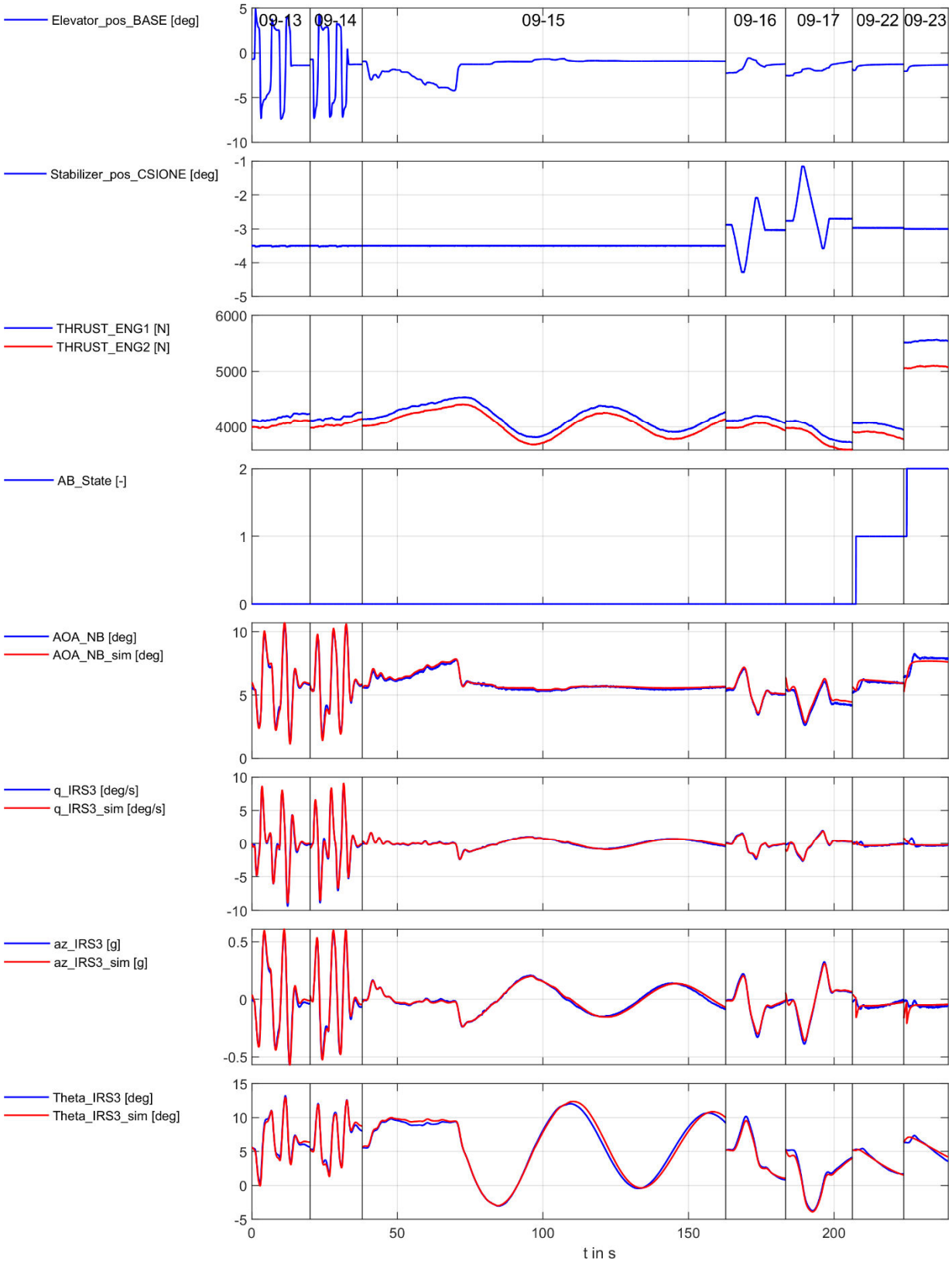

Figure 9: Longitudinal flight parameters for longitudinal flight maneuvers. Flight measurements in plotted in blue and model output in red.

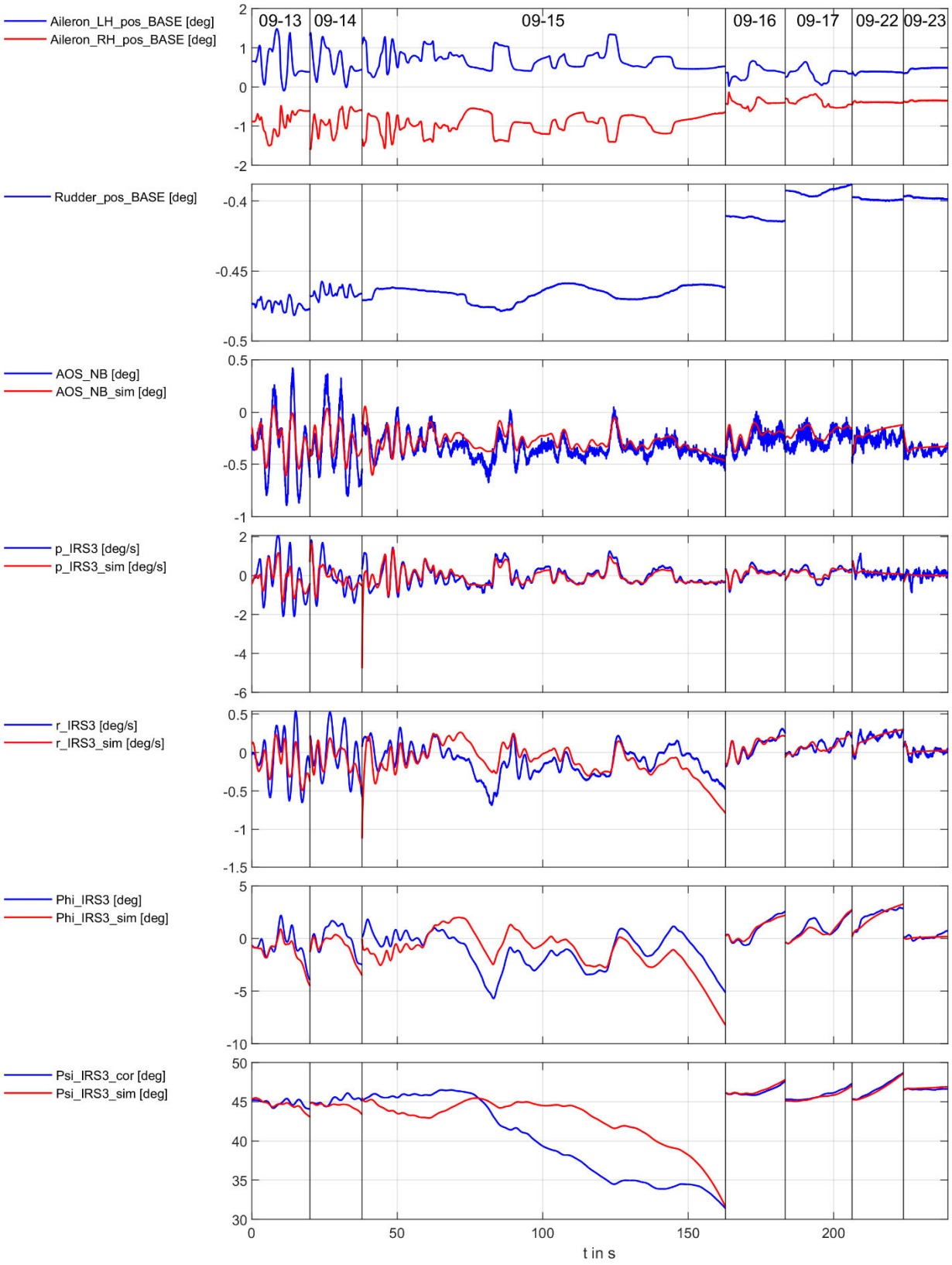

Figure 10: Lateral flight parameters for longitudinal flight maneuvers. Flight measurements in plotted in blue and model output in red.

7.2. Lateral Maneuvers

Figure 11 and Figure 12 present time series plots of the longitudinal and lateral flight parameters for selected two bank-to-bank, two aileron doublet, two rudder doublet and one steady heading sideslip maneuvers with a rudder release at the end. The maneuvers were conducted at test point No. 30 at an altitude of 45000 feet and a speed of 210 kt. The blue lines represent the measured data, while the red lines indicate the model output signals. A comparison of the model output and the measured flight parameters reveals that the two are in close agreement, thereby indicating that the selected flight dynamic behavior is accurately represented by the identified model.

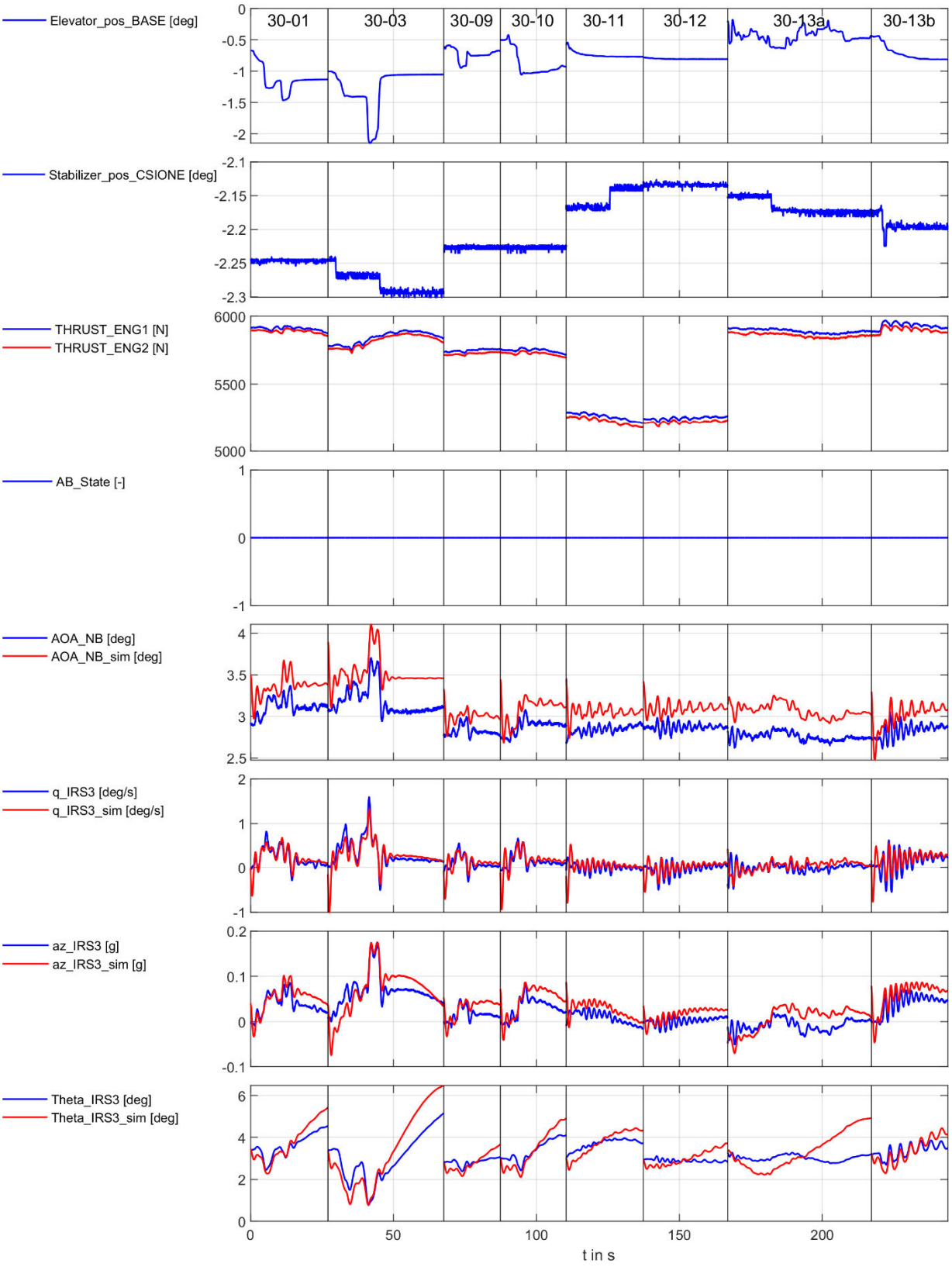

Figure 11. Longitudinal flight parameters for lateral flight maneuvers. Flight measurements in plotted in blue and model output in red.

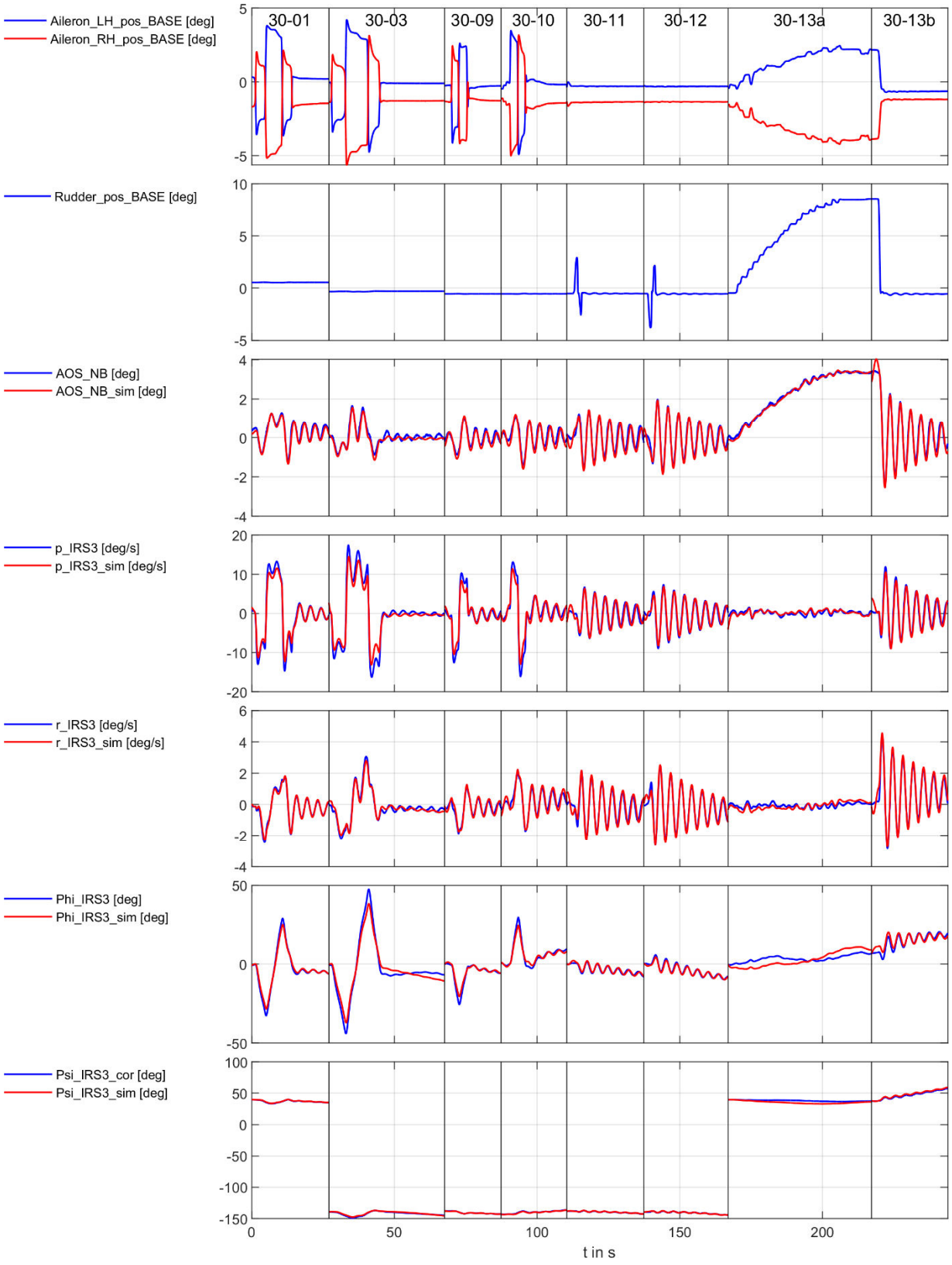

Figure 12: Lateral flight parameters for lateral flight maneuvers. Flight measurements in plotted in blue and model output in red.

7.3. Cross Plots – Configuration SF0 - CLEAN

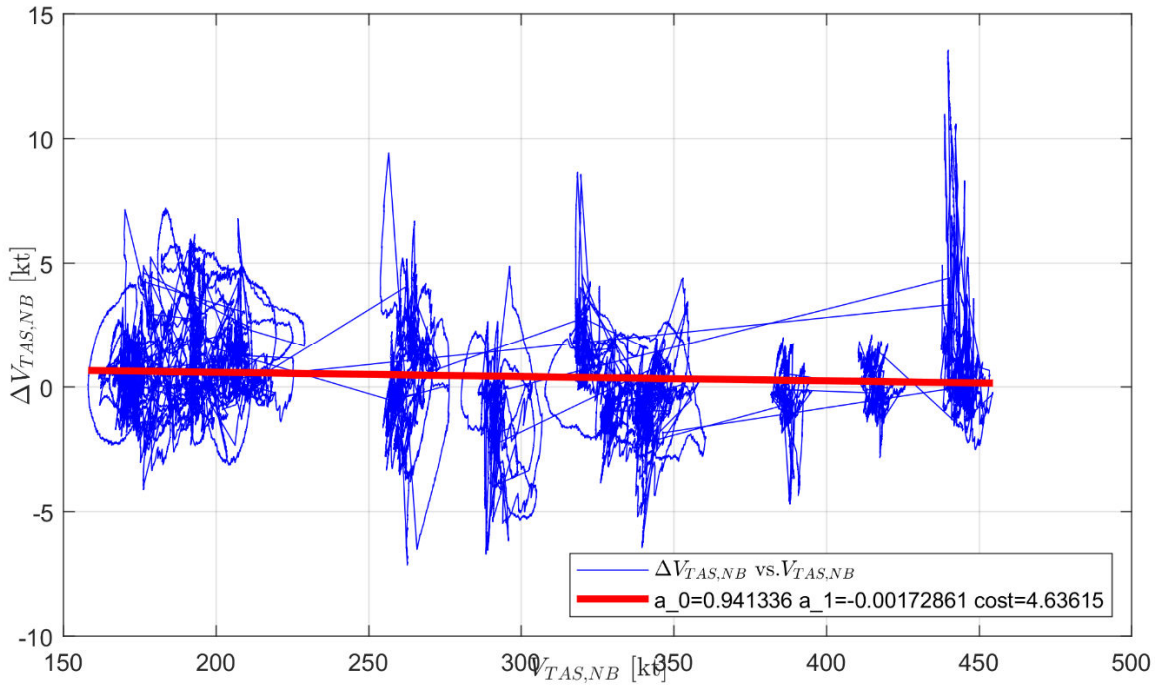

Figure 13: Comparison of the model error in VTAS and the measured VTAS for configuration SF0.

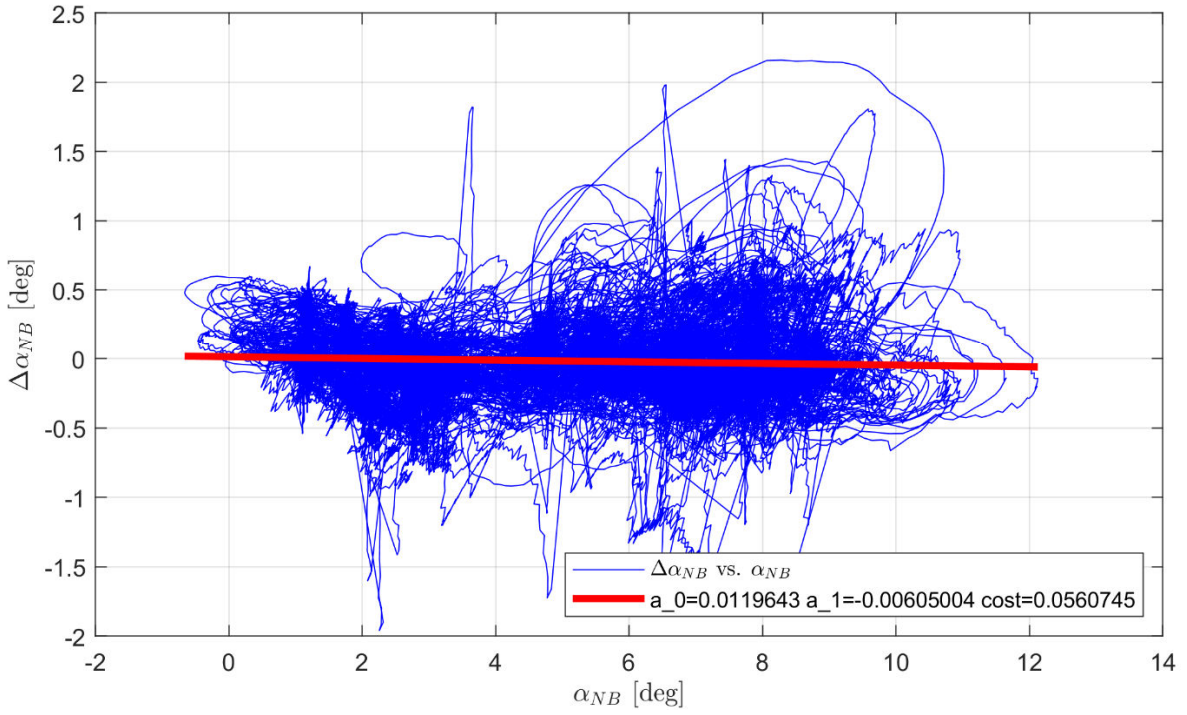

Figure 14: Comparison of the model error in the angle of attack and the measured angle of attack for configuration SF0.

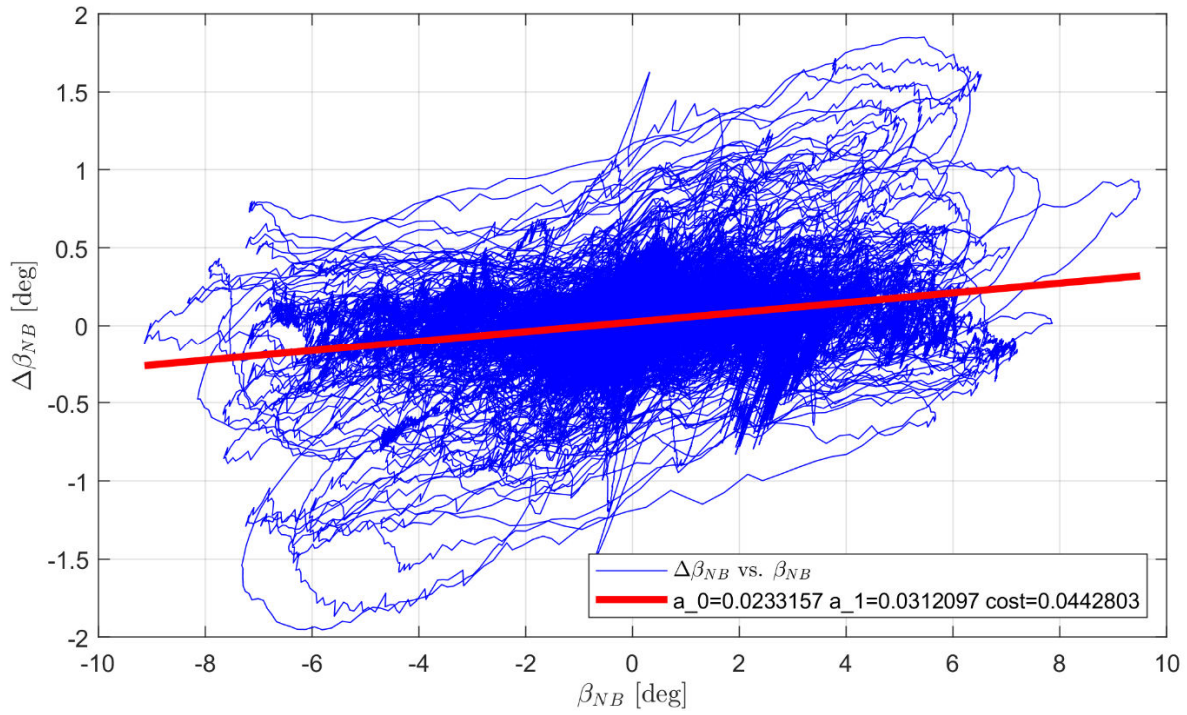

Figure 15: Comparison of the model error in the angle of sideslip and the measured angle of sideslip for configuration SF0.

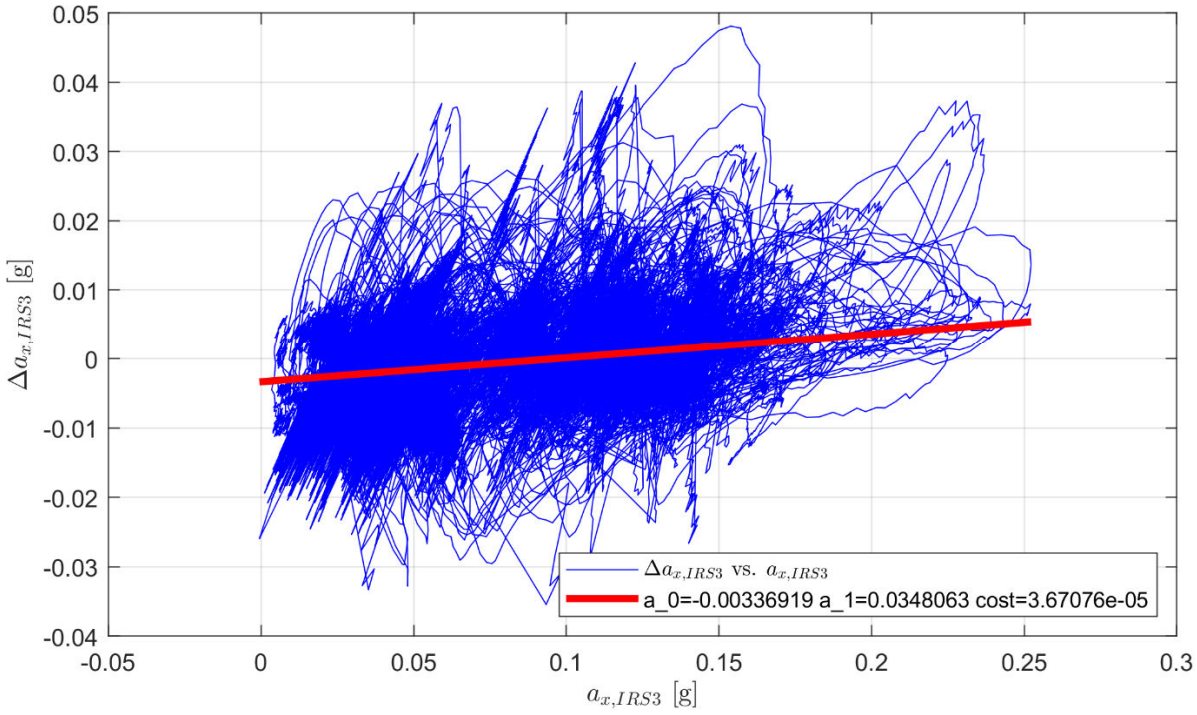

Figure 16: Comparison of the model error in the longitudinal acceleration and the measured longitudinal acceleration for configuration SF0.

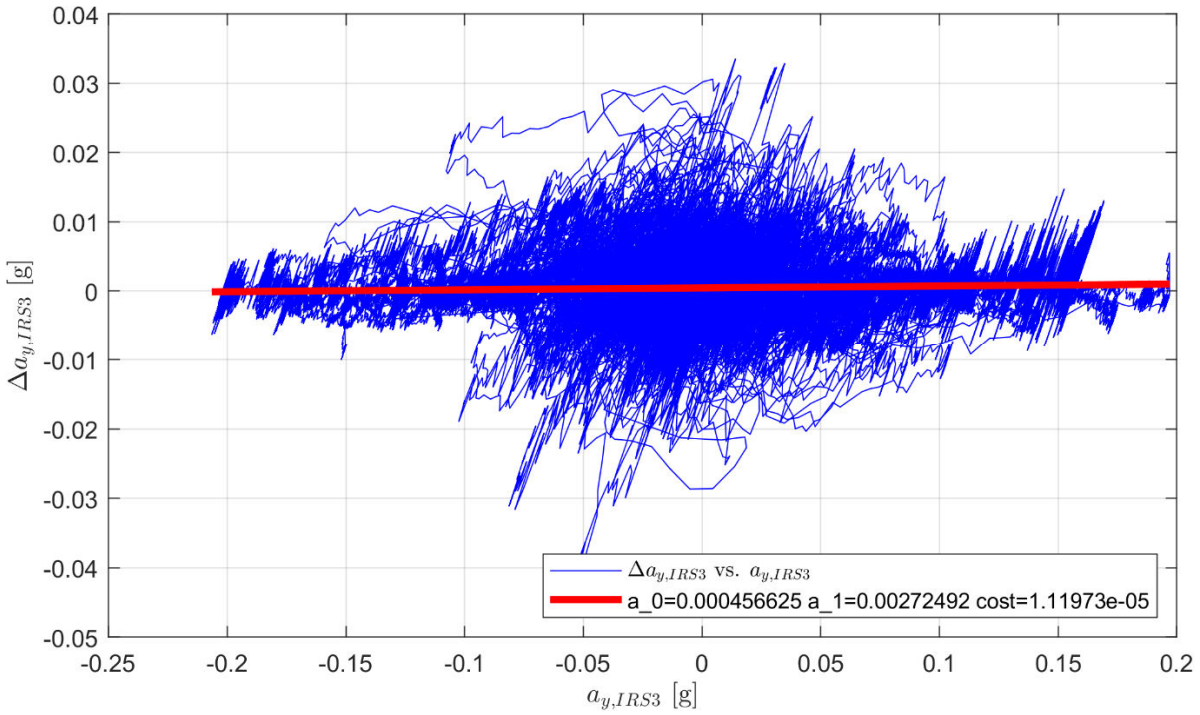

Figure 17: Comparison of the model error in the lateral acceleration and the measured lateral acceleration for configuration SF0.

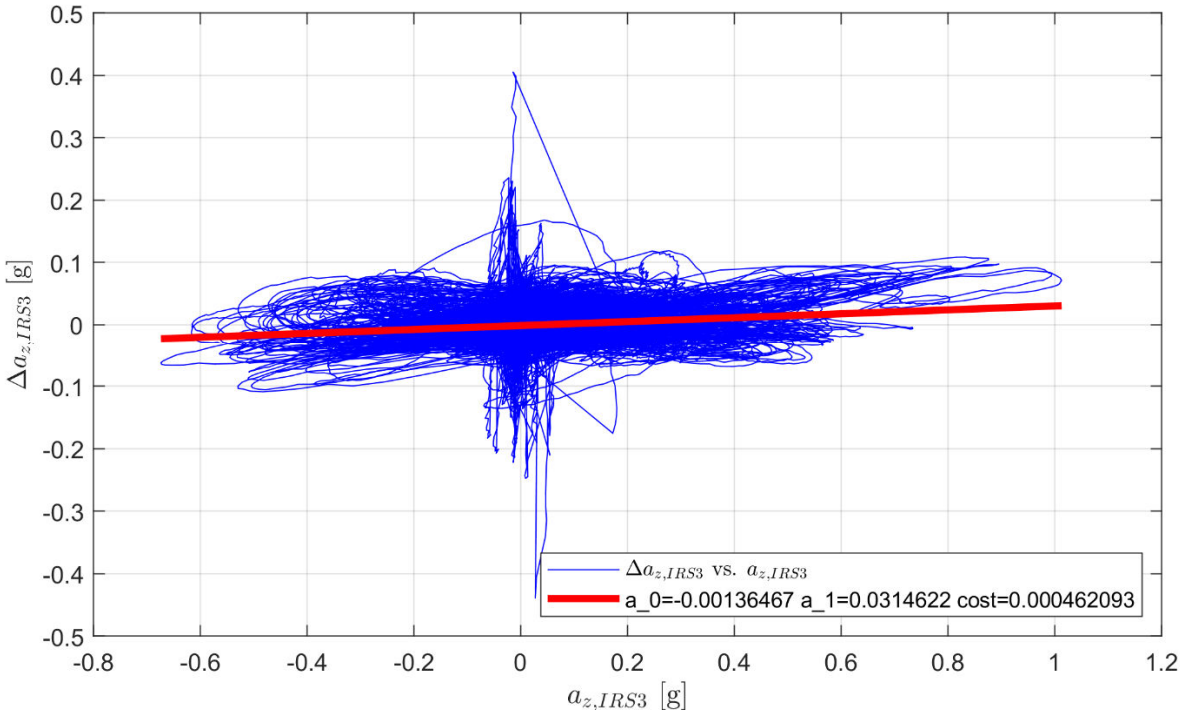

Figure 18: Comparison of the model error in the vertical acceleration and the measured vertical acceleration for configuration SF0.

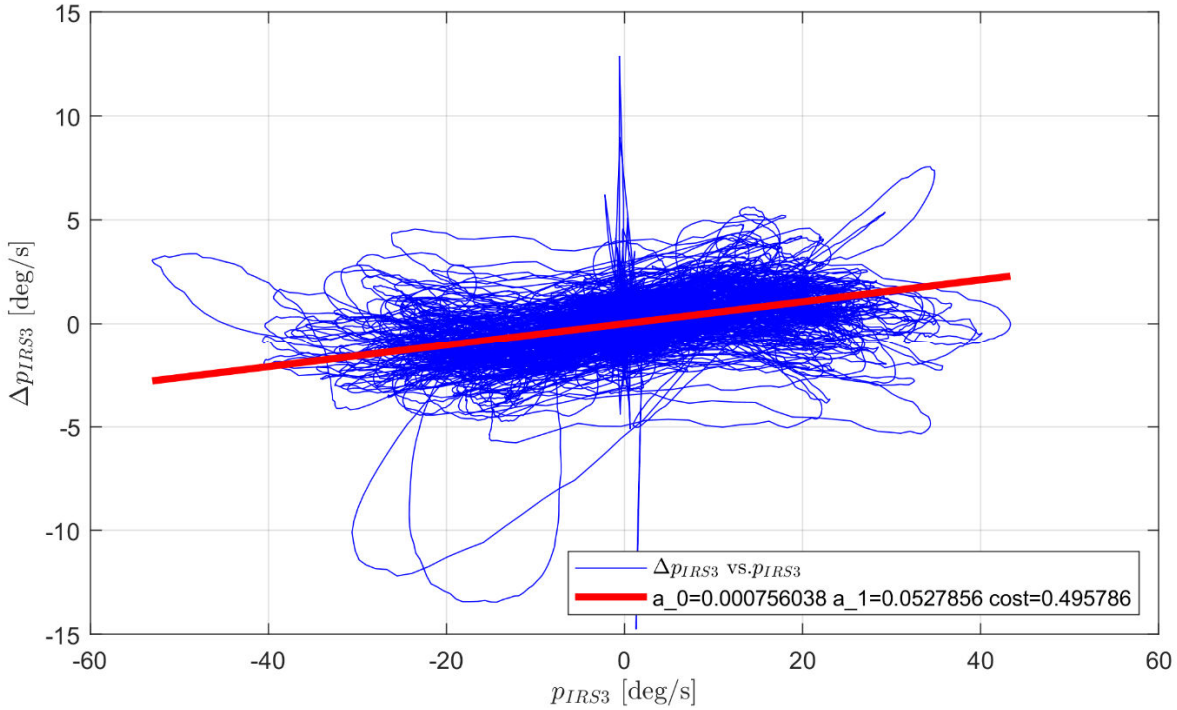

Figure 19: Comparison of the model error in the roll rate and the measured roll rate for configuration SF0.

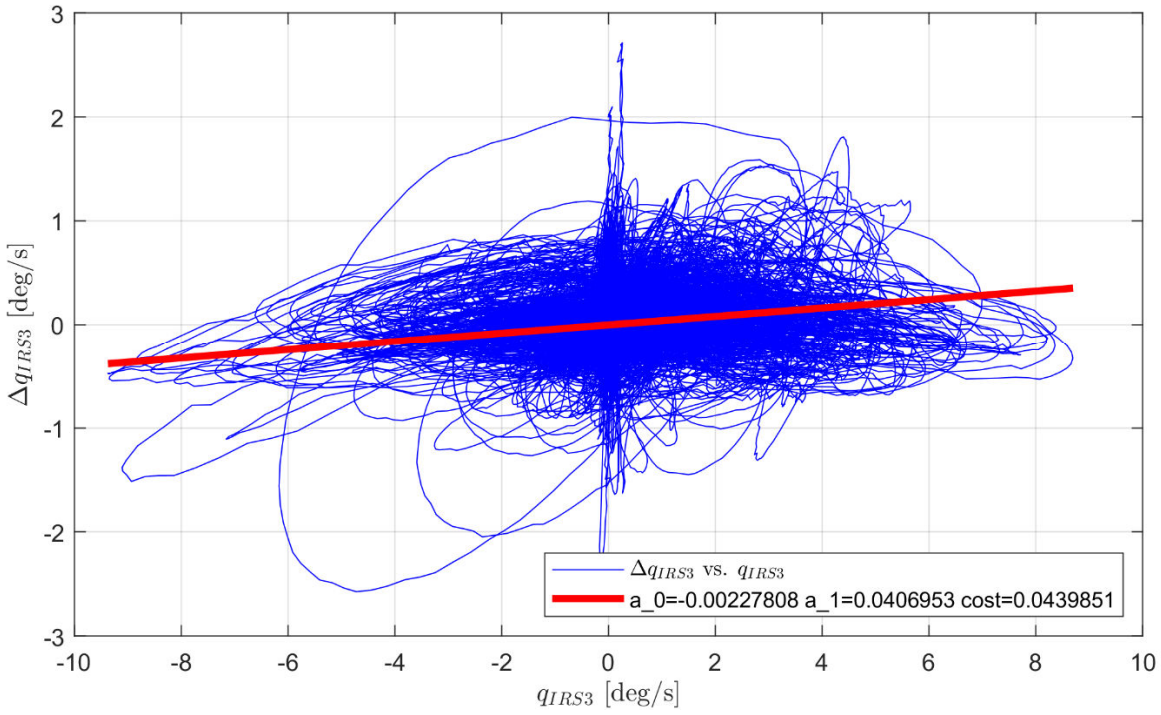

Figure 20: Comparison of the model error in the pitch rate and the measured pitch rate for configuration SF0.

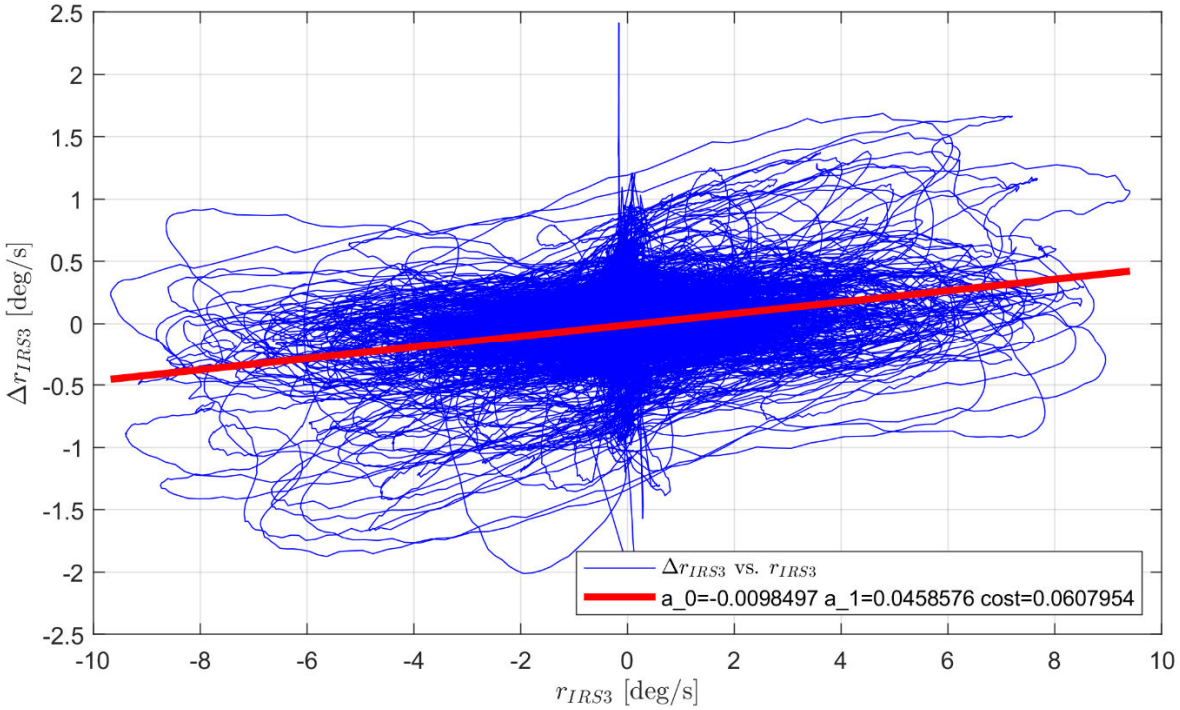

Figure 21: Comparison of the model error in the yaw rate and the measured yaw rate for configuration SF0.

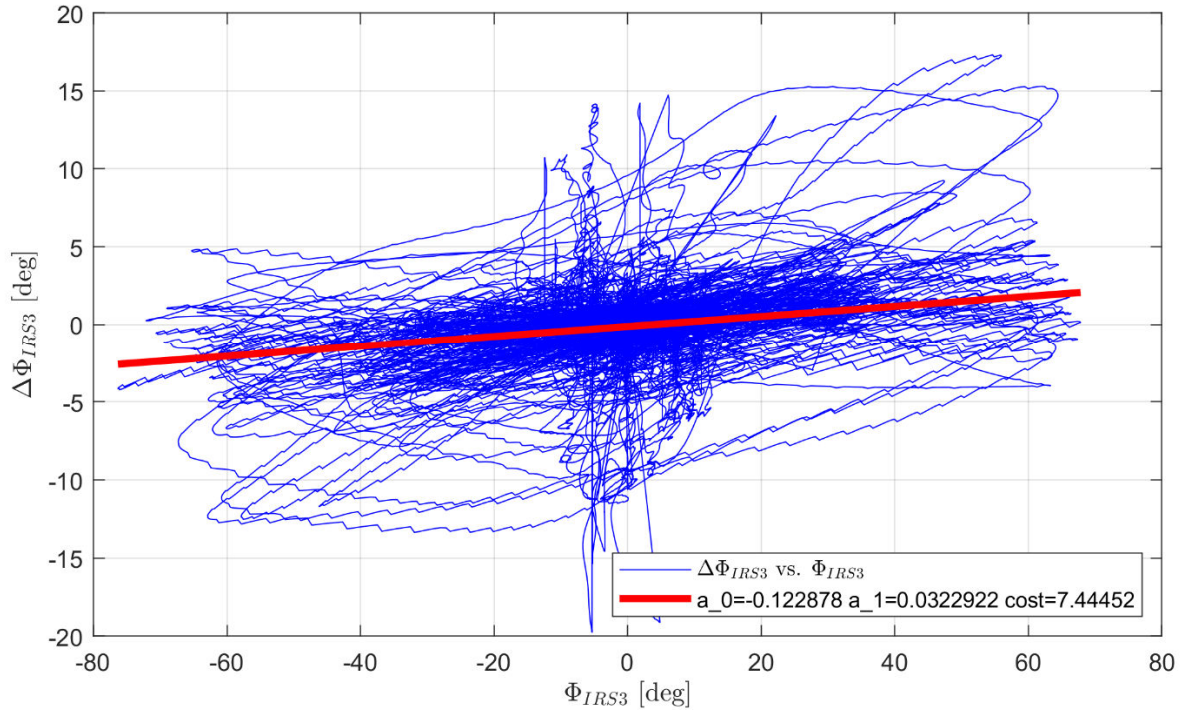

Figure 22: Comparison of the model error in the roll angle and the measured roll angle for configuration SF0.

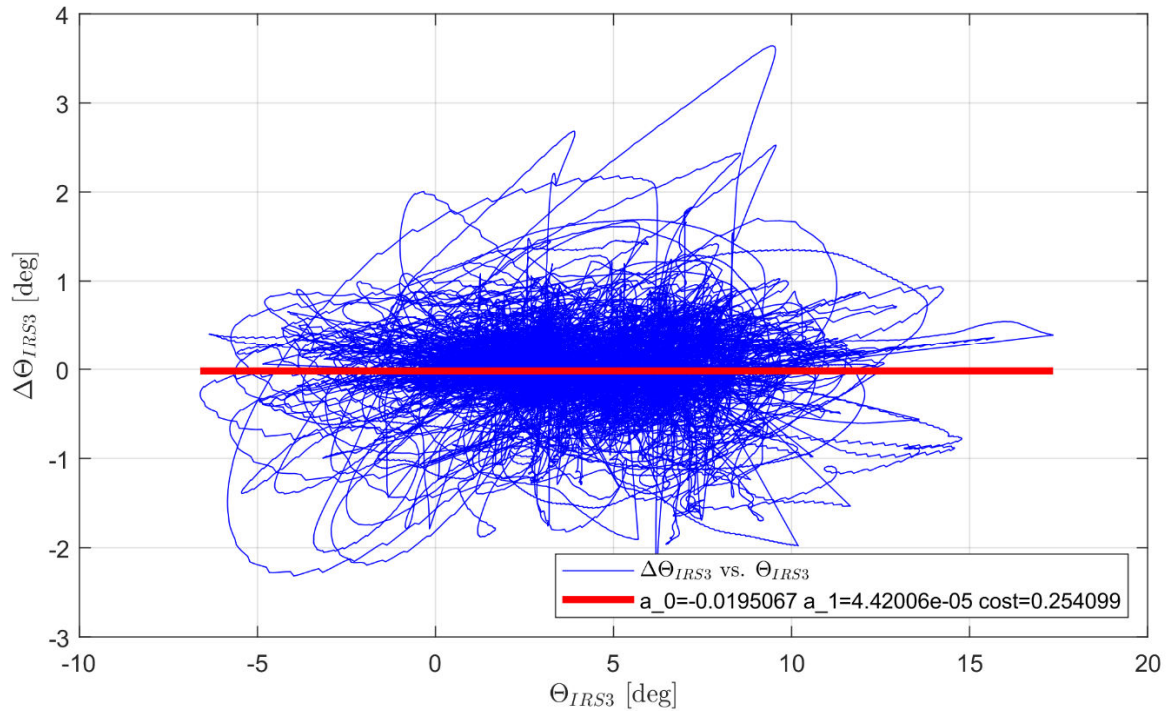

Figure 23: Comparison of the model error in the pitch angle and the measured pitch angle for configuration SF0.

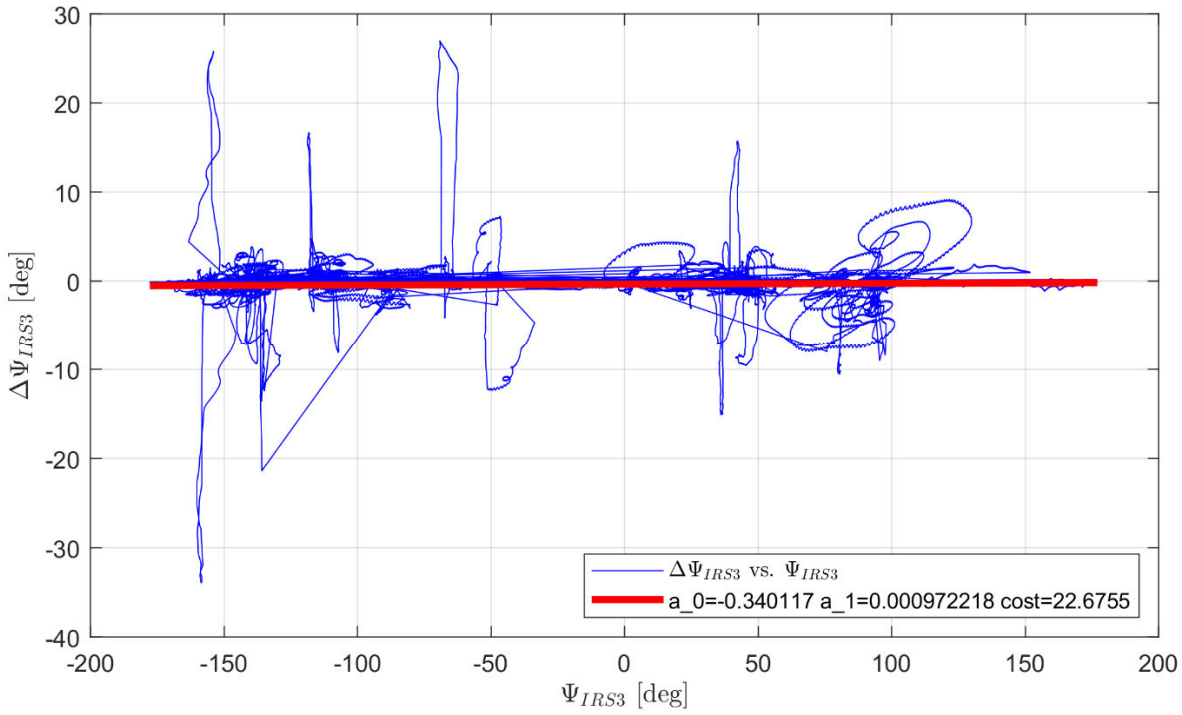

Figure 24: Comparison of the model error in the heading angle and the measured heading angle for configuration SF0.

7.4. Cross Plots – Configuration SF1

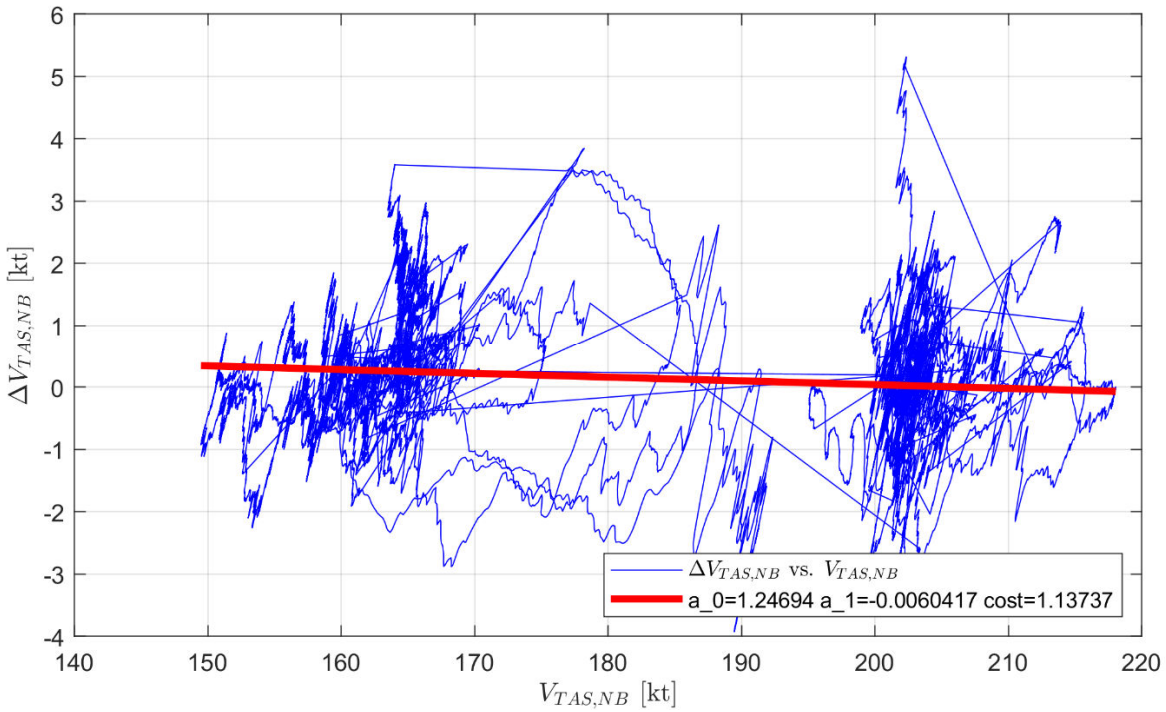

Figure 25: Comparison of the model error in VTAS and the measured VTAS for configuration SF1.

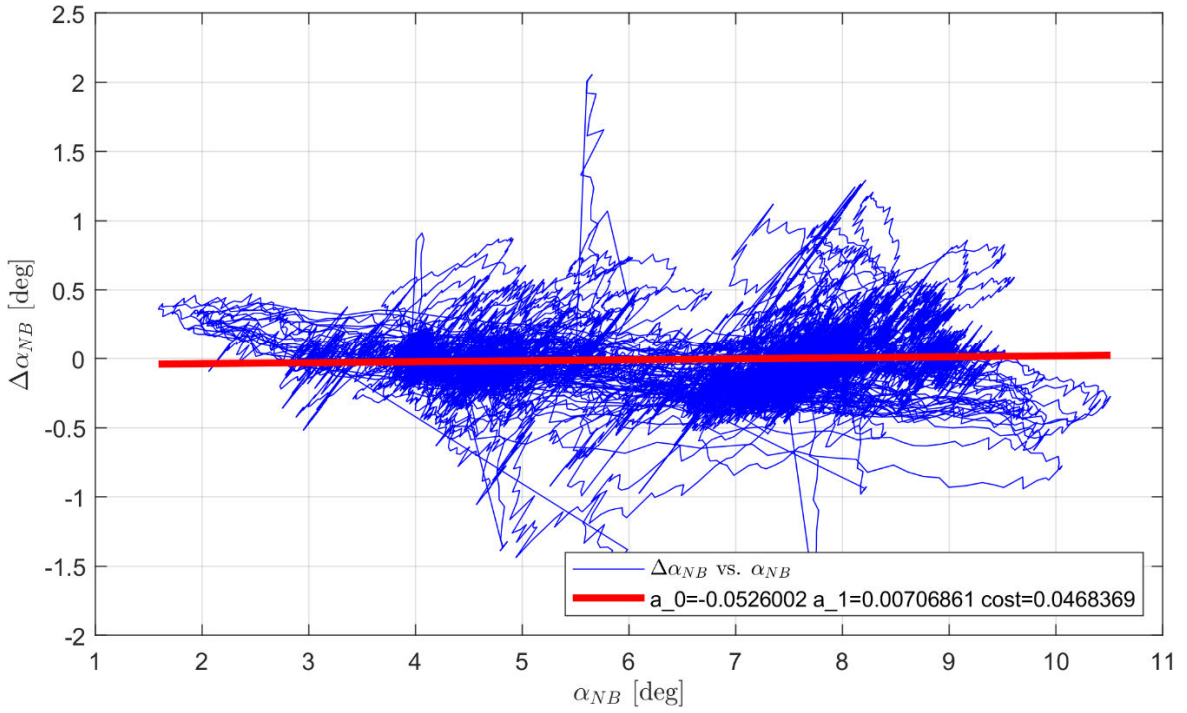

Figure 26: Comparison of the model error in the angle of attack and the measured angle of attack for configuration SF1.

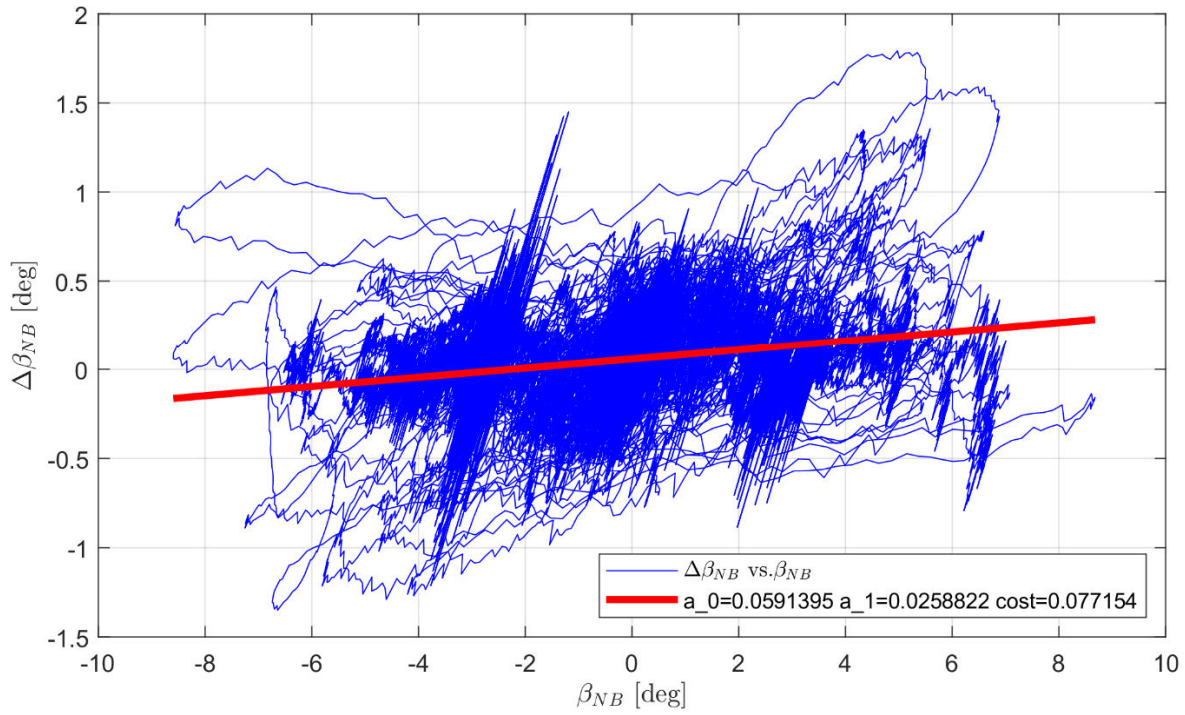

Figure 27: Comparison of the model error in the angle of sideslip and the measured angle of sideslip for configuration SF1.

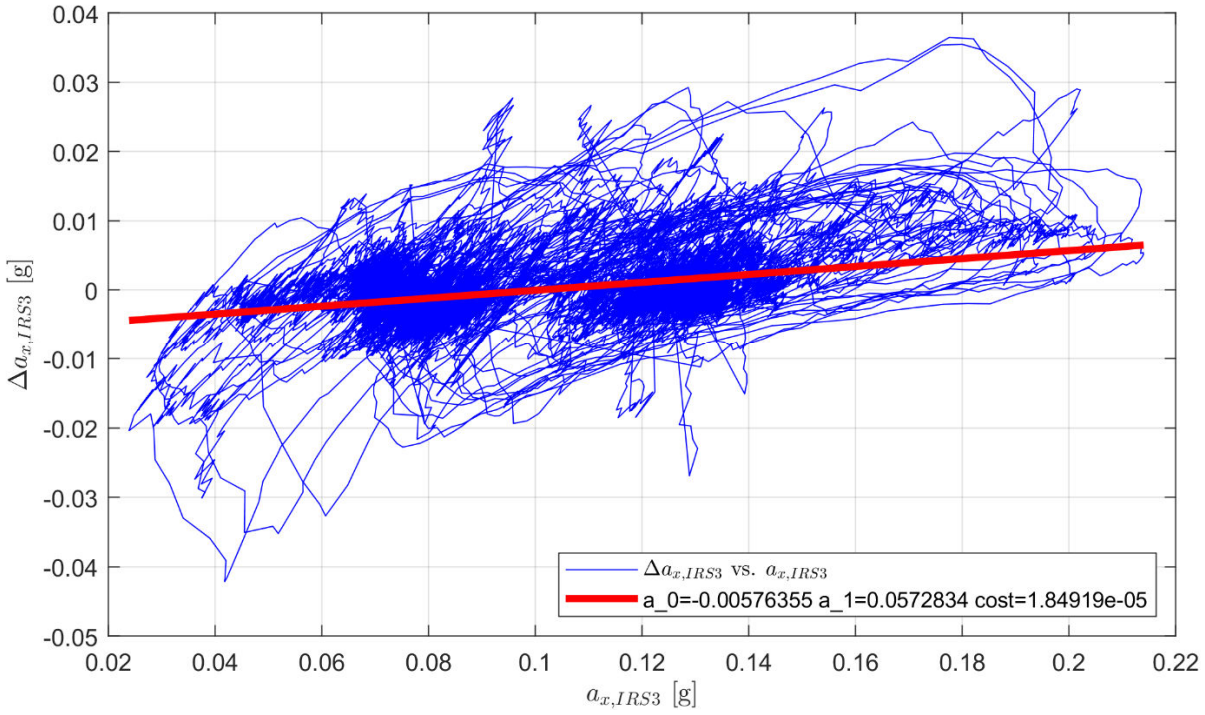

Figure 28: Comparison of the model error in the longitudinal acceleration and the measured longitudinal acceleration for configuration SF1.

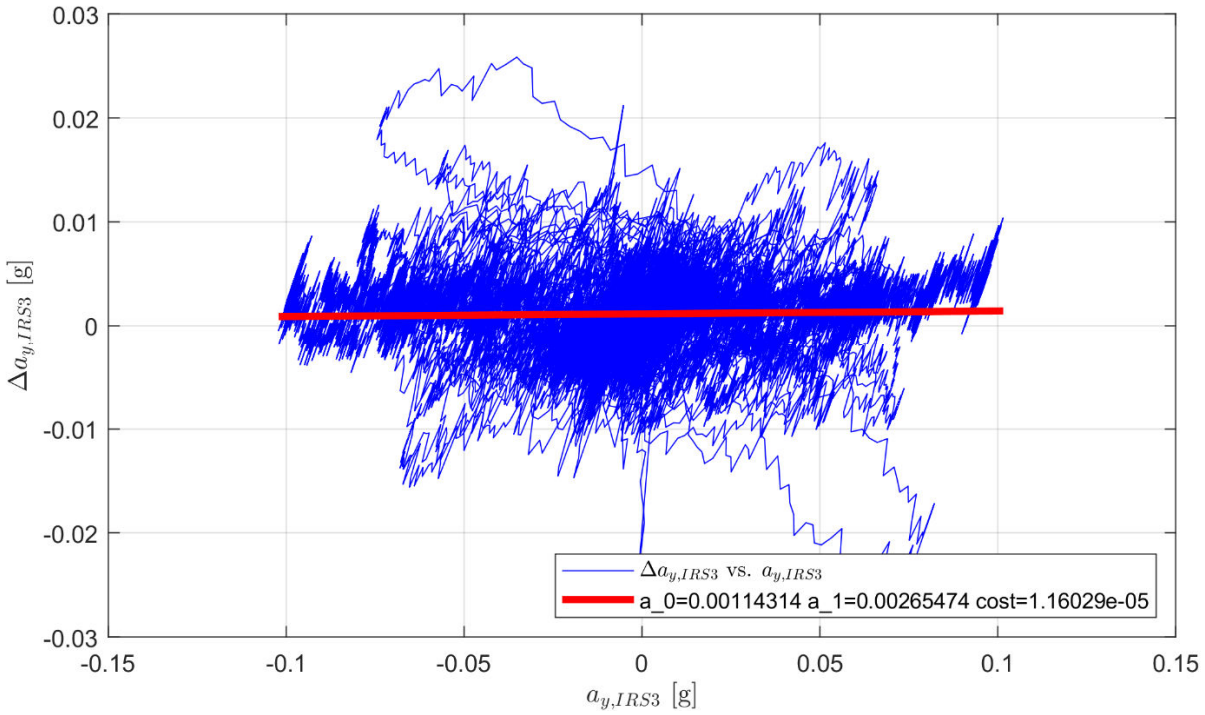

Figure 29: Comparison of the model error in the lateral acceleration and the measured lateral acceleration for configuration SF1.

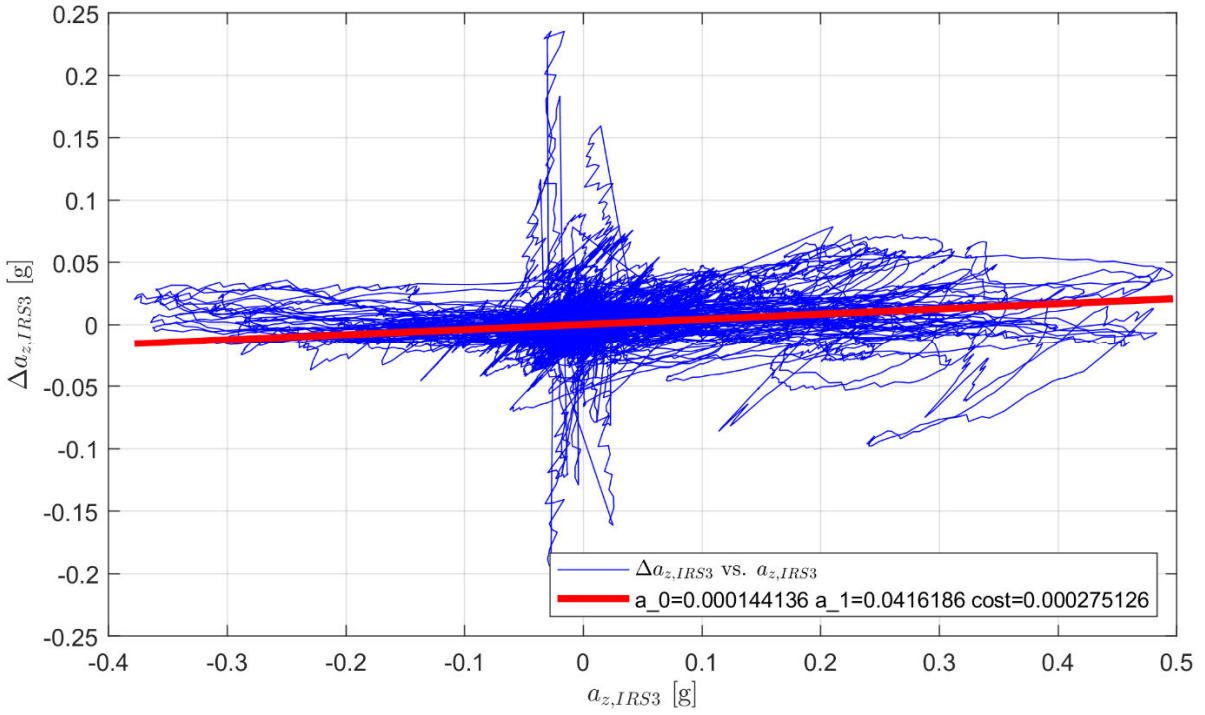

Figure 30: Comparison of the model error in the vertical acceleration and the measured vertical acceleration for configuration SF1.

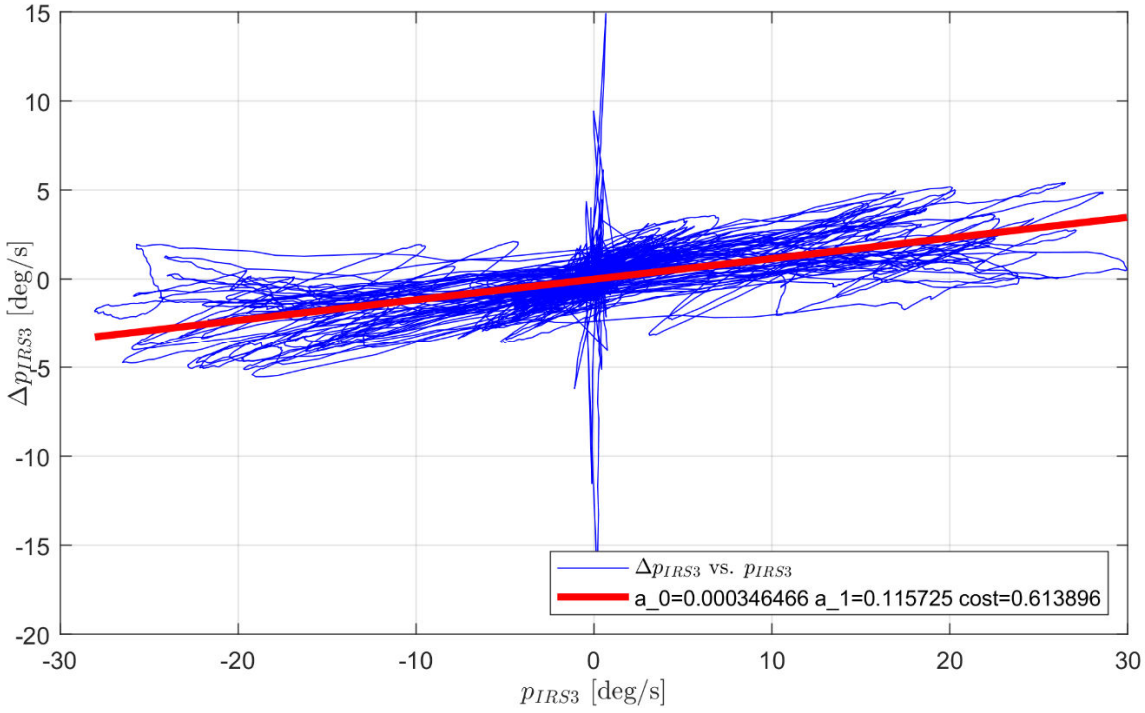

Figure 31: Comparison of the model error in the roll rate and the measured roll rate for configuration SF1.

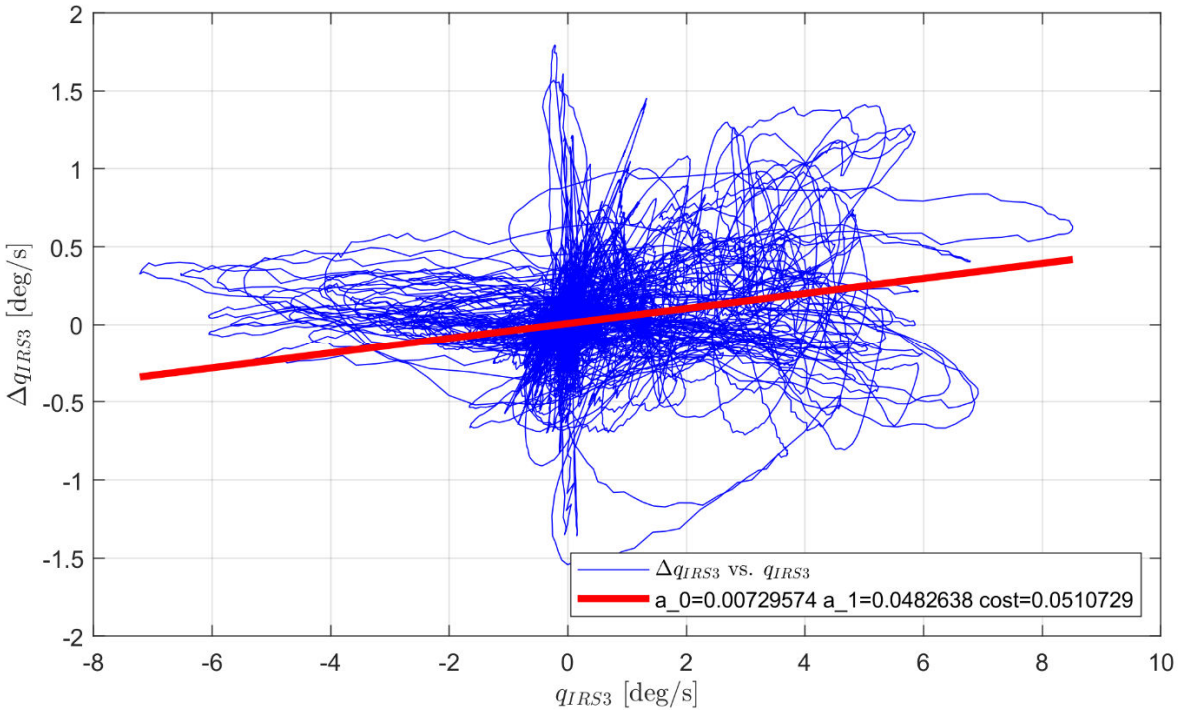

Figure 32: Comparison of the model error in the pitch rate and the measured pitch rate for configuration SF1.

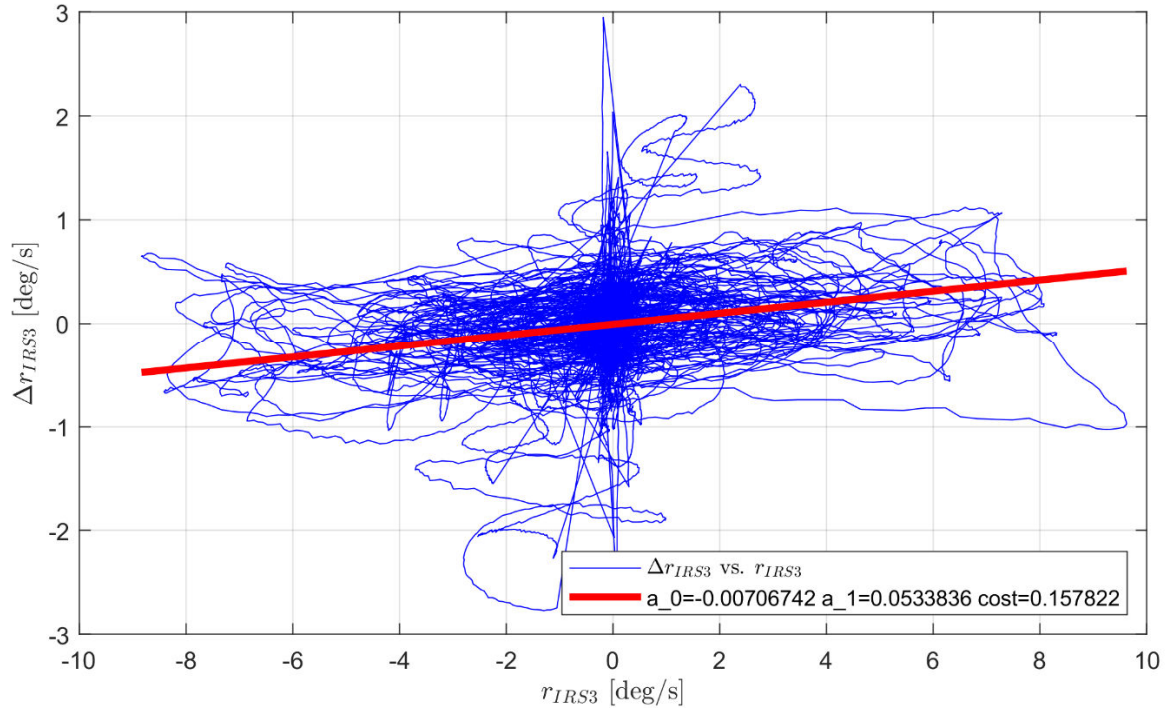

Figure 33: Comparison of the model error in the yaw rate and the measured yaw rate for configuration SF1.

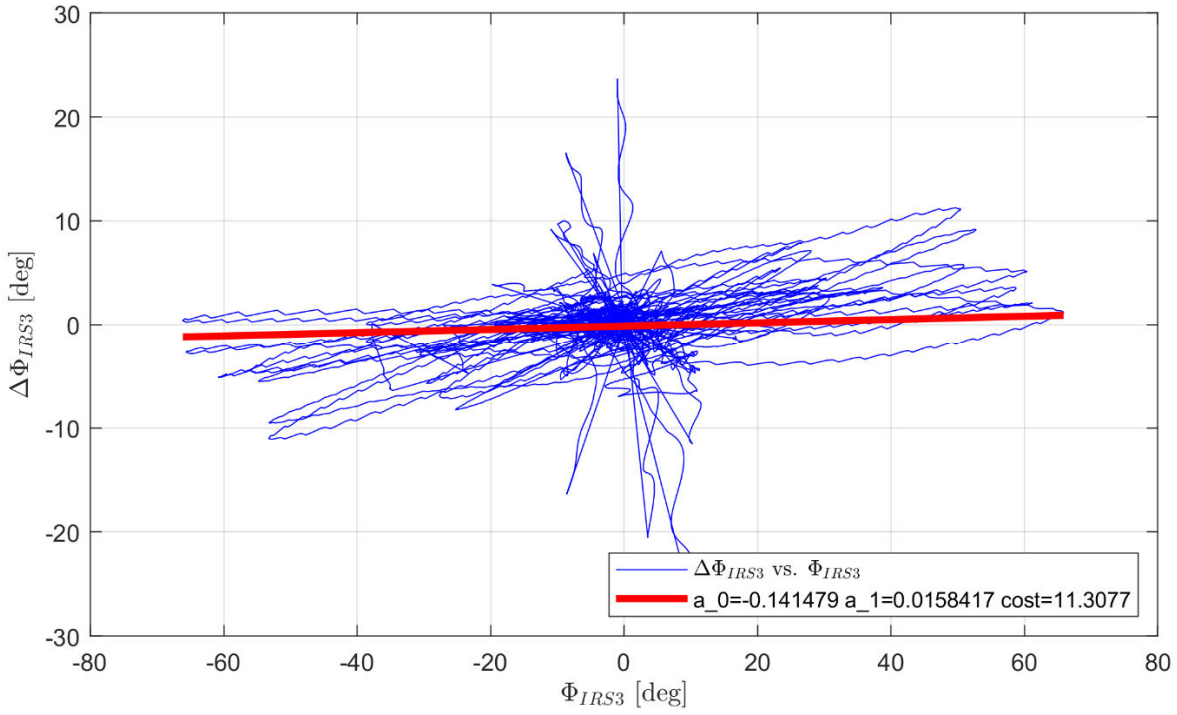

Figure 34: Comparison of the model error in the roll angle and the measured roll angle for configuration SF1.

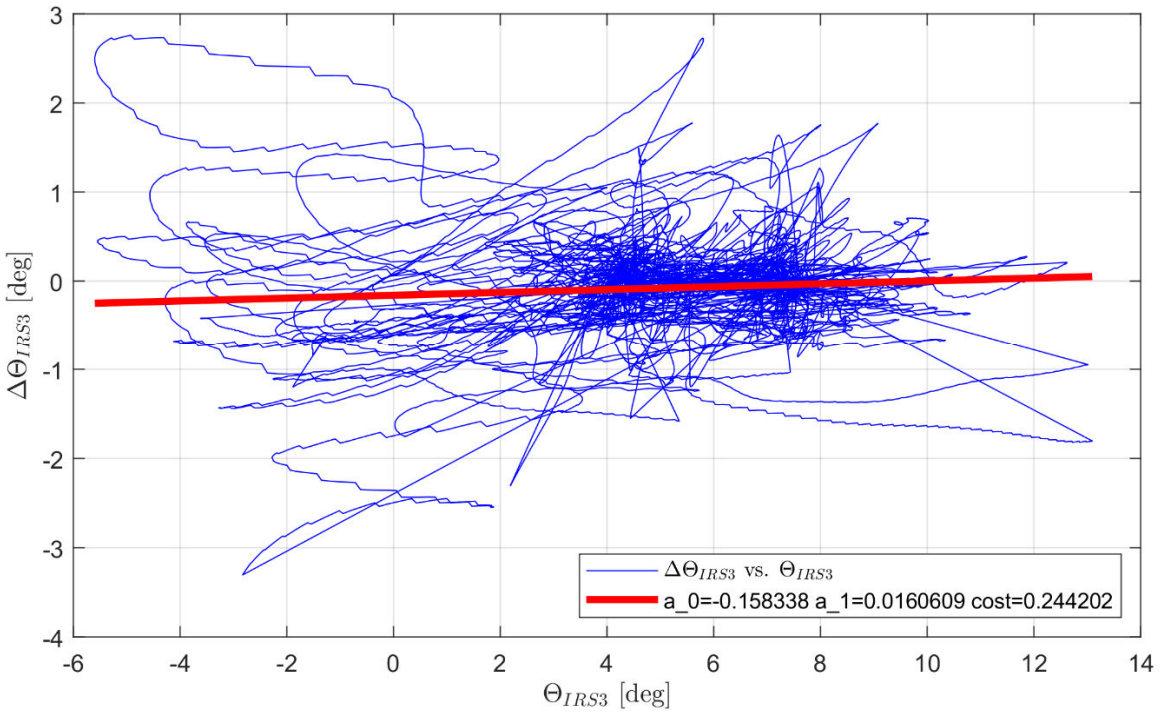

Figure 35: Comparison of the model error in the pitch angle and the measured pitch angle for configuration SF1.

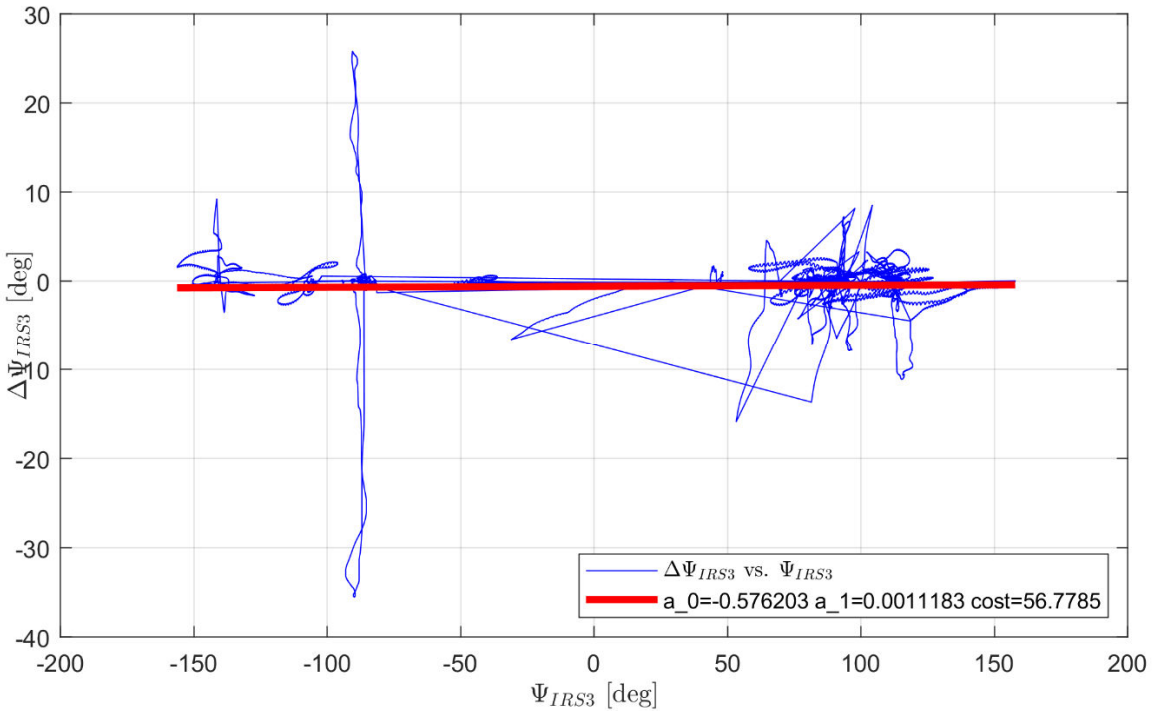

Figure 36: Comparison of the model error in the heading angle and the measured heading angle for configuration SF1.

7.5. Cross Plots – Configuration SF2

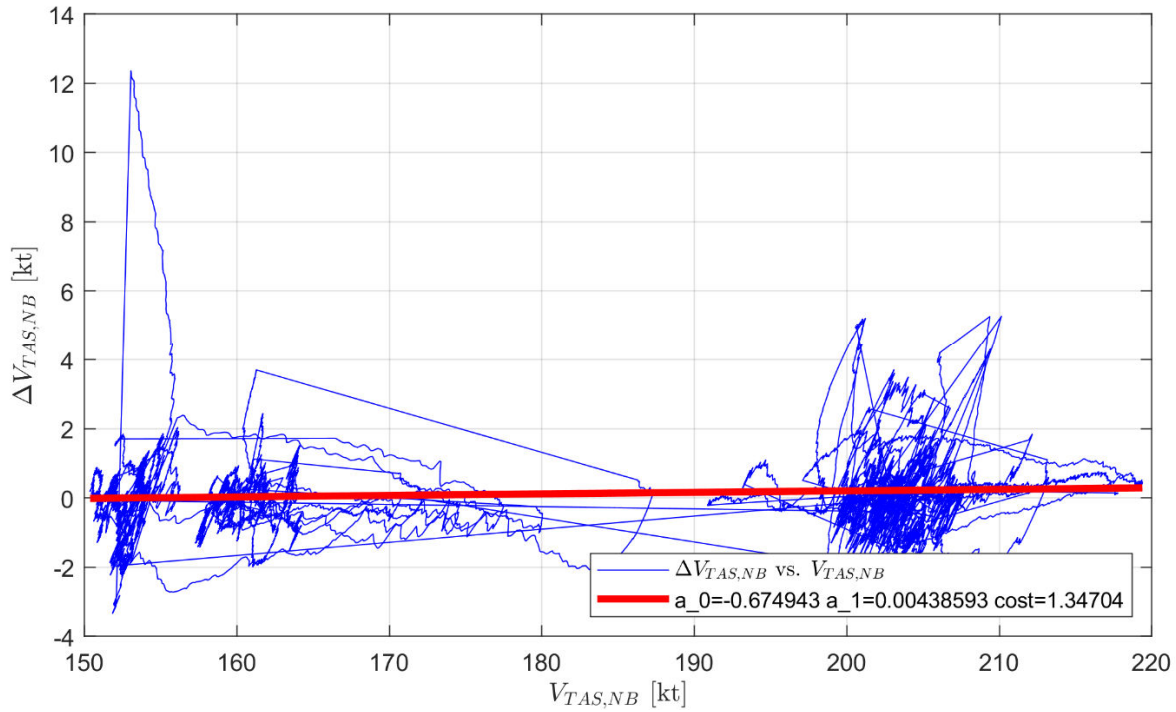

Figure 37: Comparison of the model error in VTAS and the measured VTAS for configuration SF2.

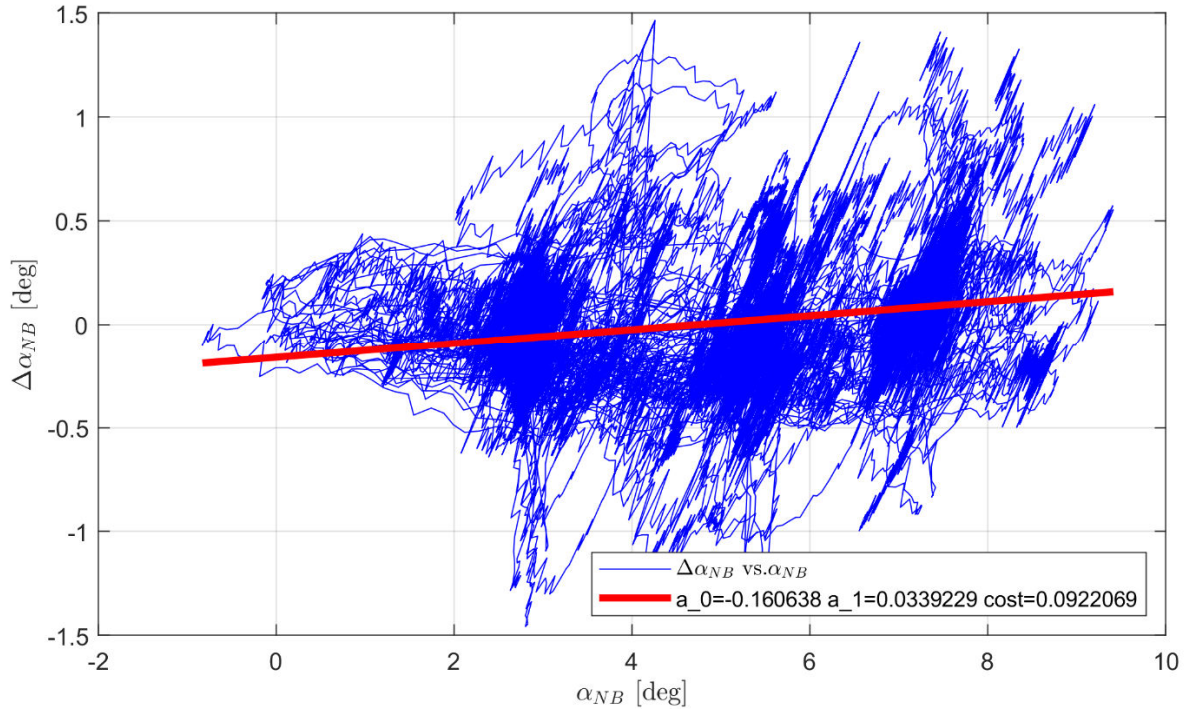

Figure 38: Comparison of the model error in the angle of attack and the measured angle of attack for configuration SF2.

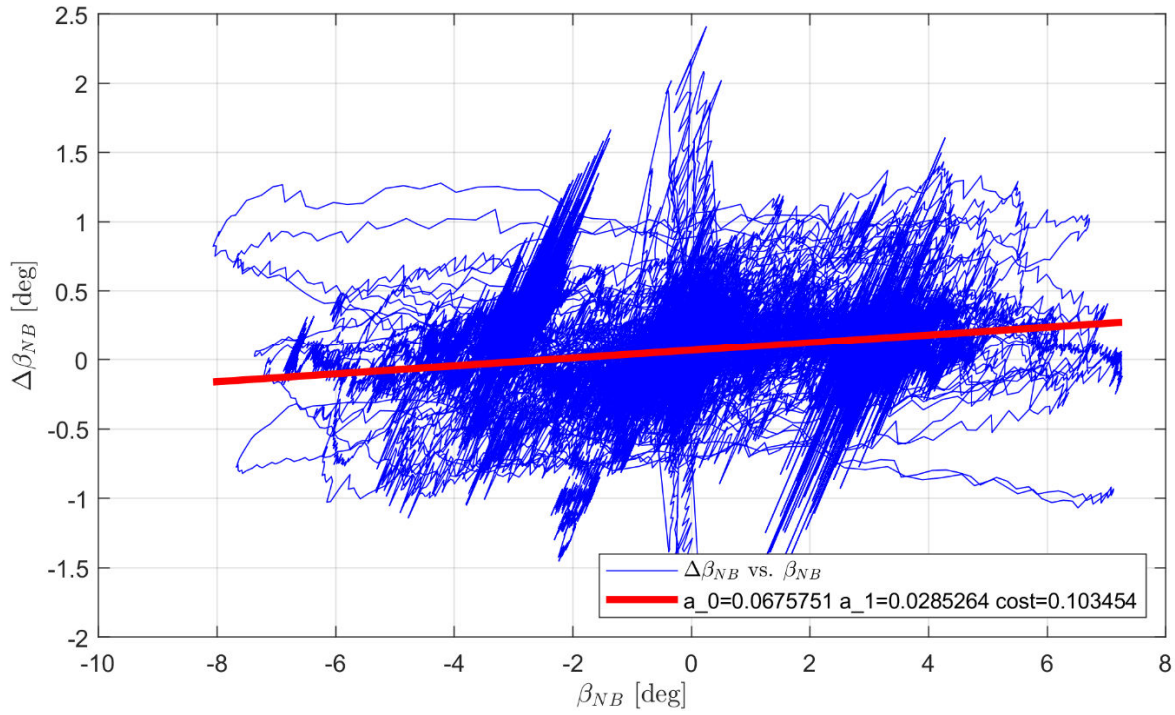

Figure 39: Comparison of the model error in the angle of sideslip and the measured angle of sideslip for configuration SF2.

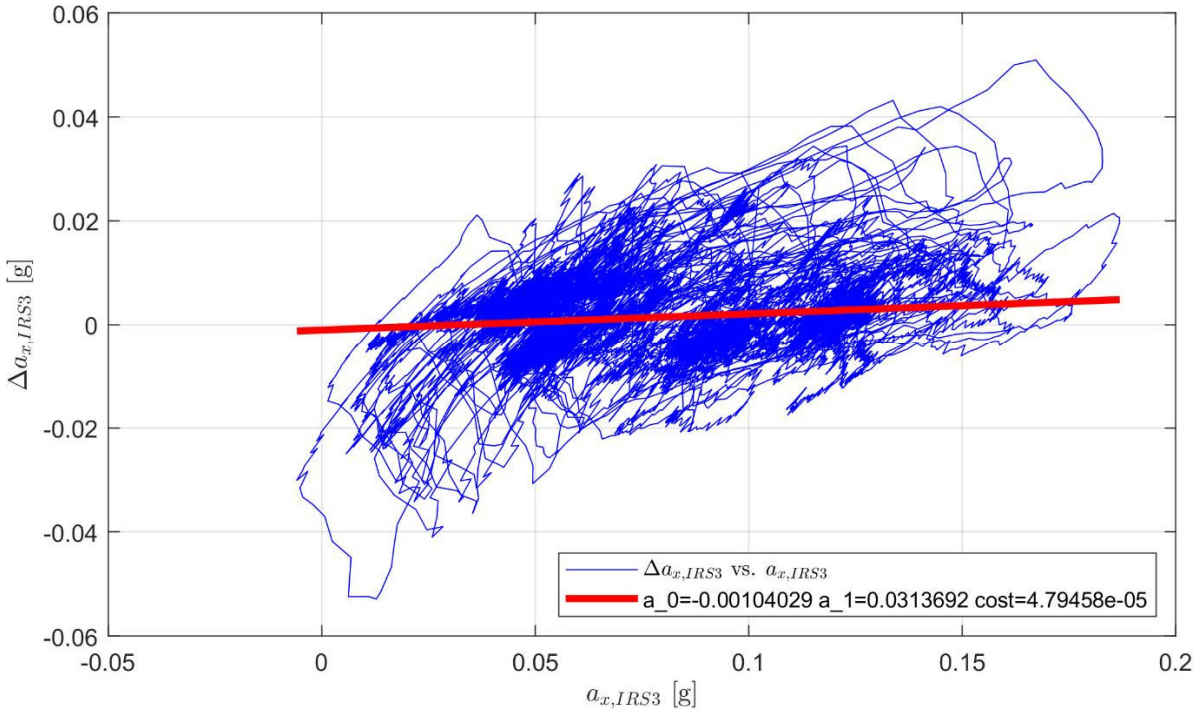

Figure 40: Comparison of the model error in the longitudinal acceleration and the measured longitudinal acceleration for configuration SF2.

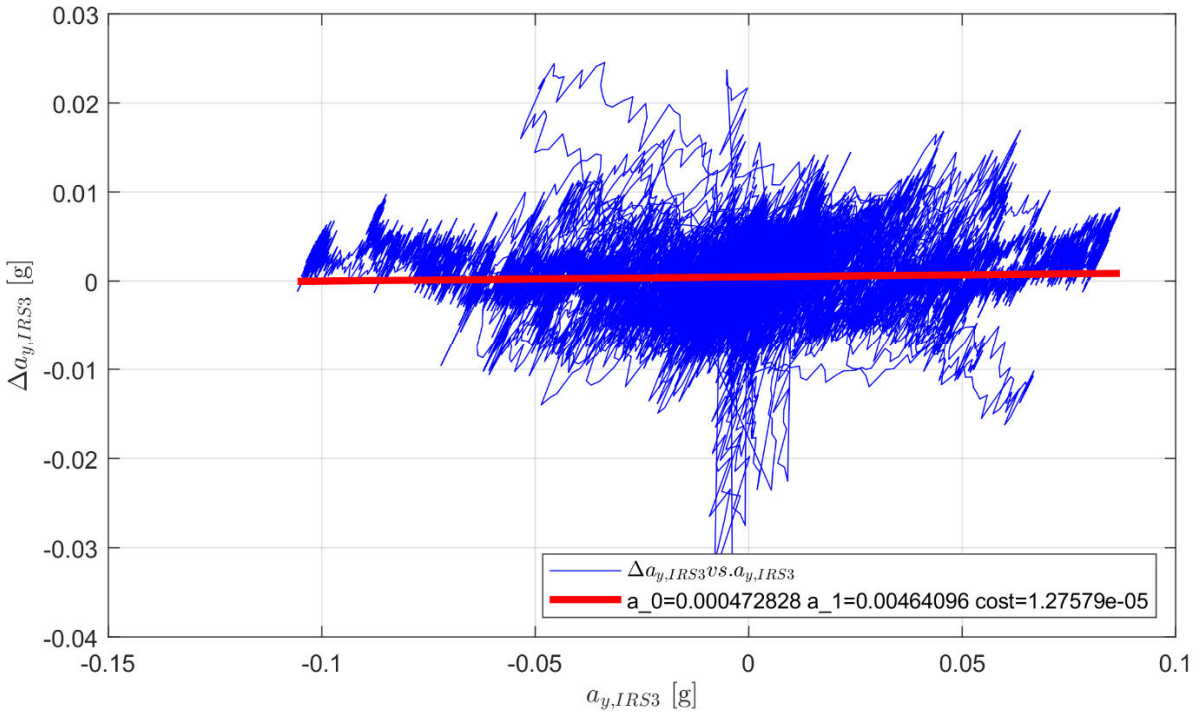

Figure 41: Comparison of the model error in the lateral acceleration and the measured lateral acceleration for configuration SF2.

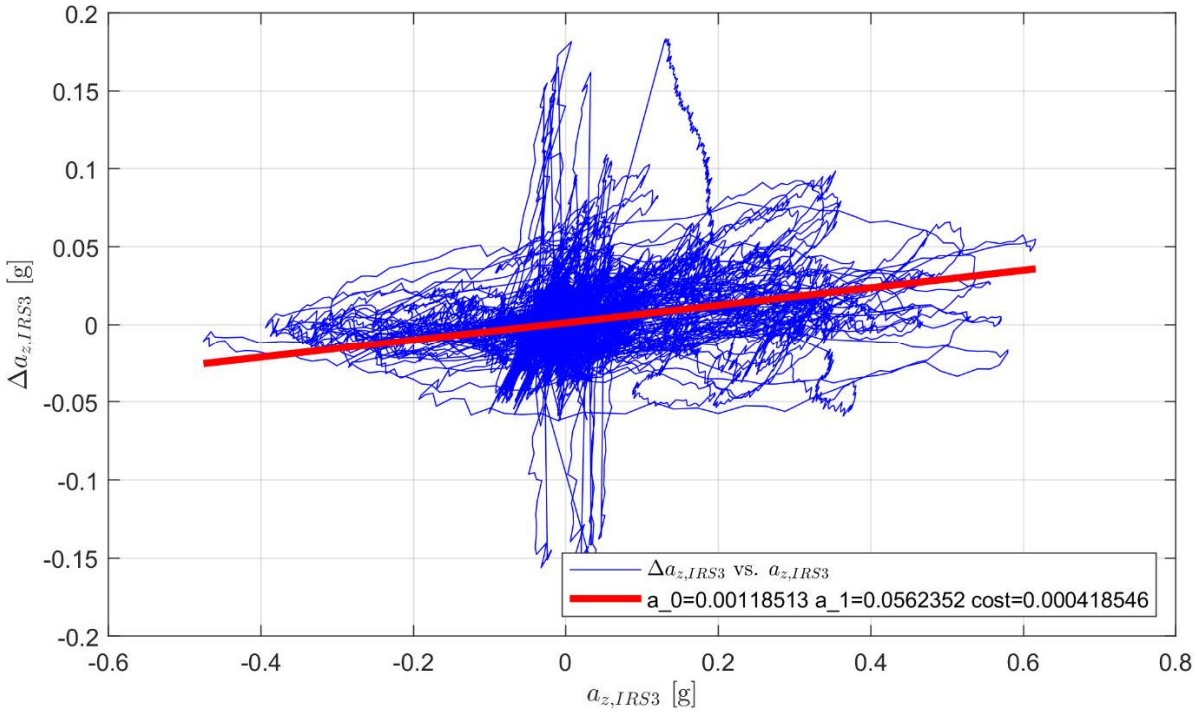

Figure 42: Comparison of the model error in the vertical acceleration and the measured vertical acceleration for configuration SF2.

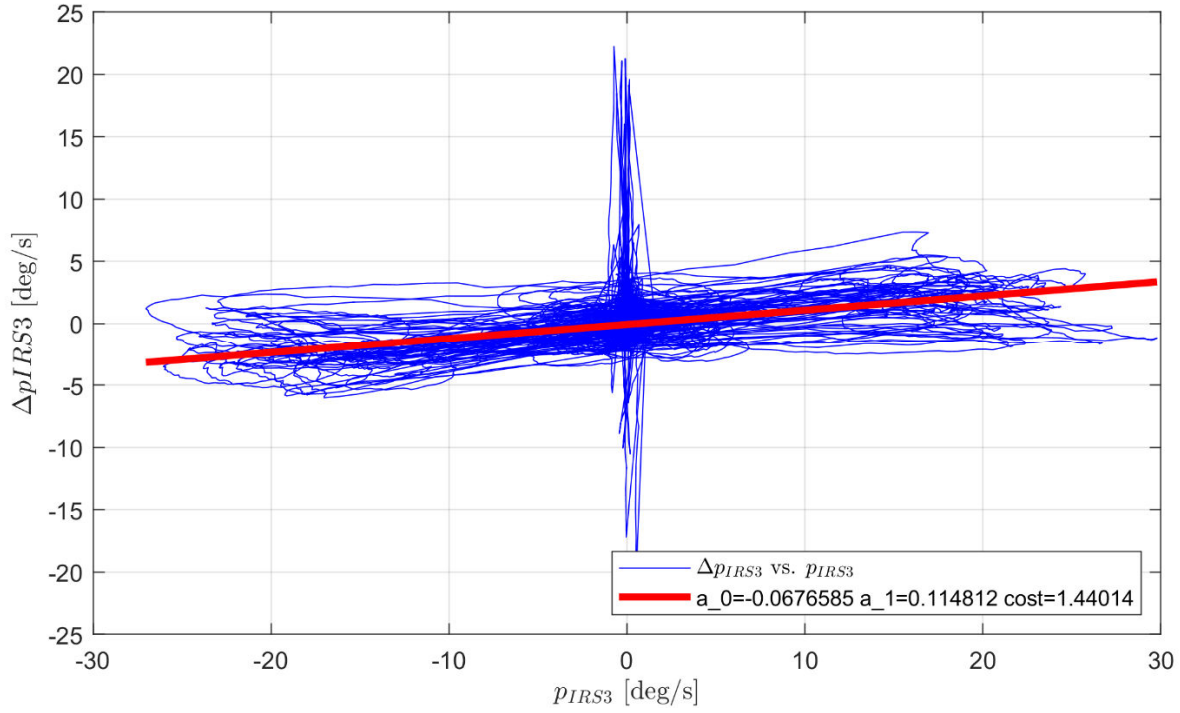

Figure 43: Comparison of the model error in the roll rate and the measured roll rate for configuration SF2.

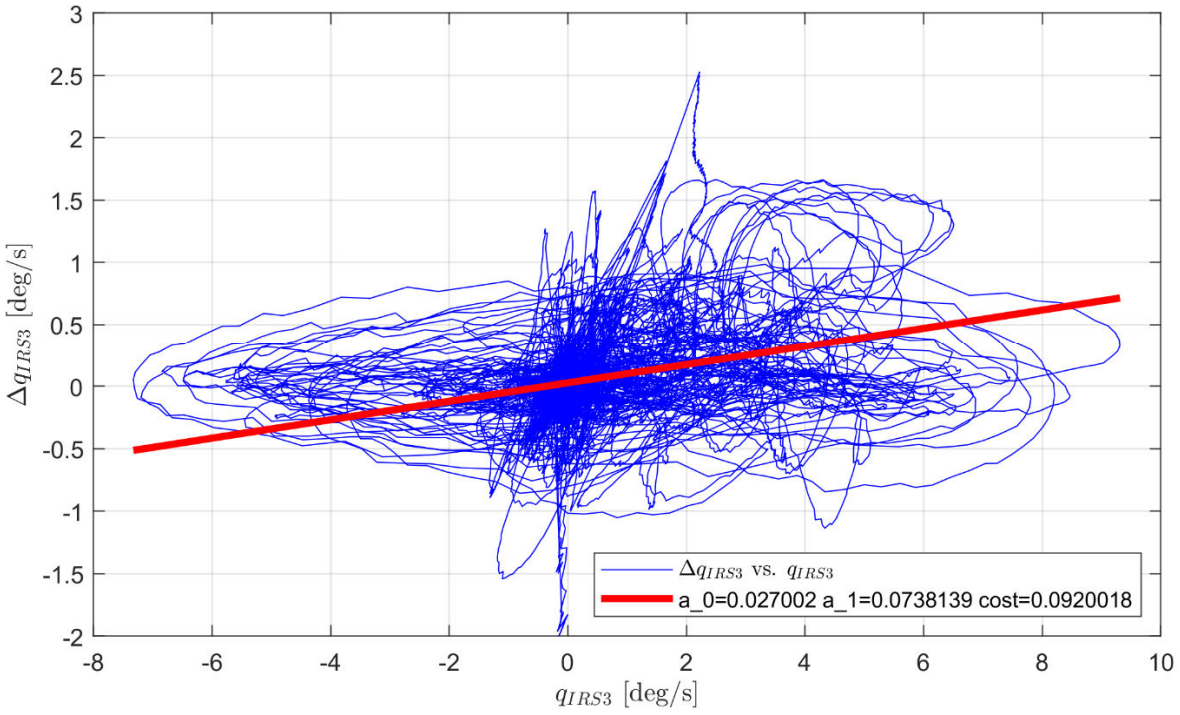

Figure 44: Comparison of the model error in the pitch rate and the measured pitch rate for configuration SF2.

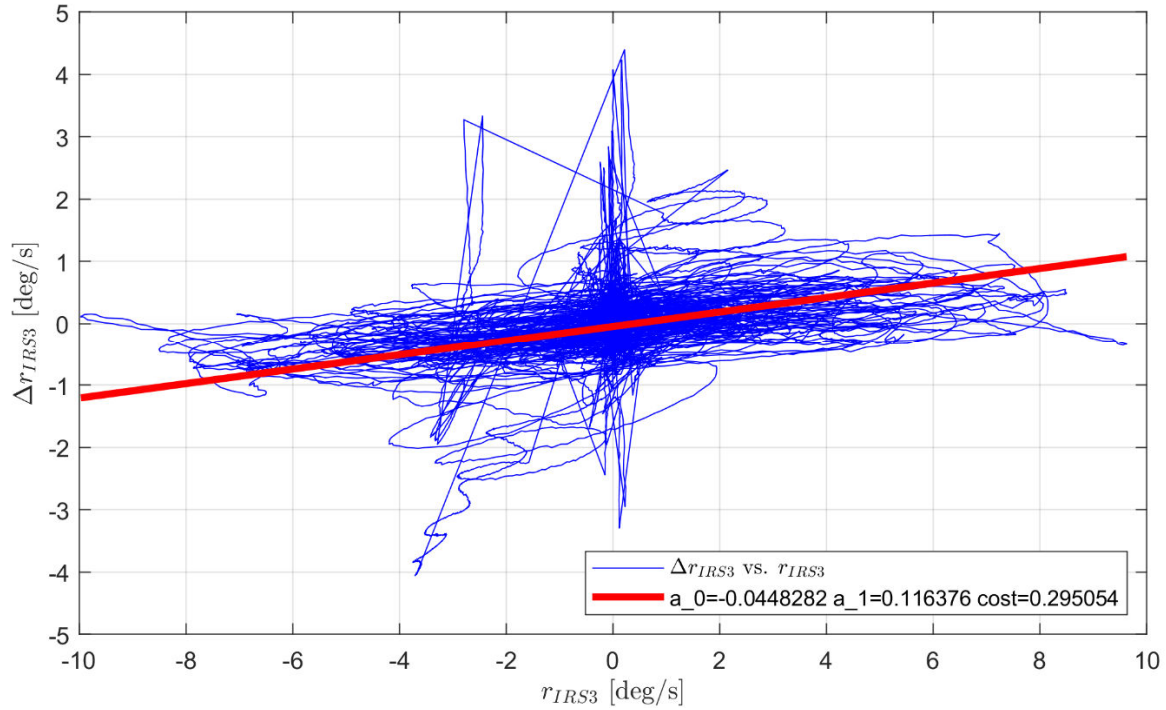

Figure 45: Comparison of the model error in the yaw rate and the measured yaw rate for configuration SF2.

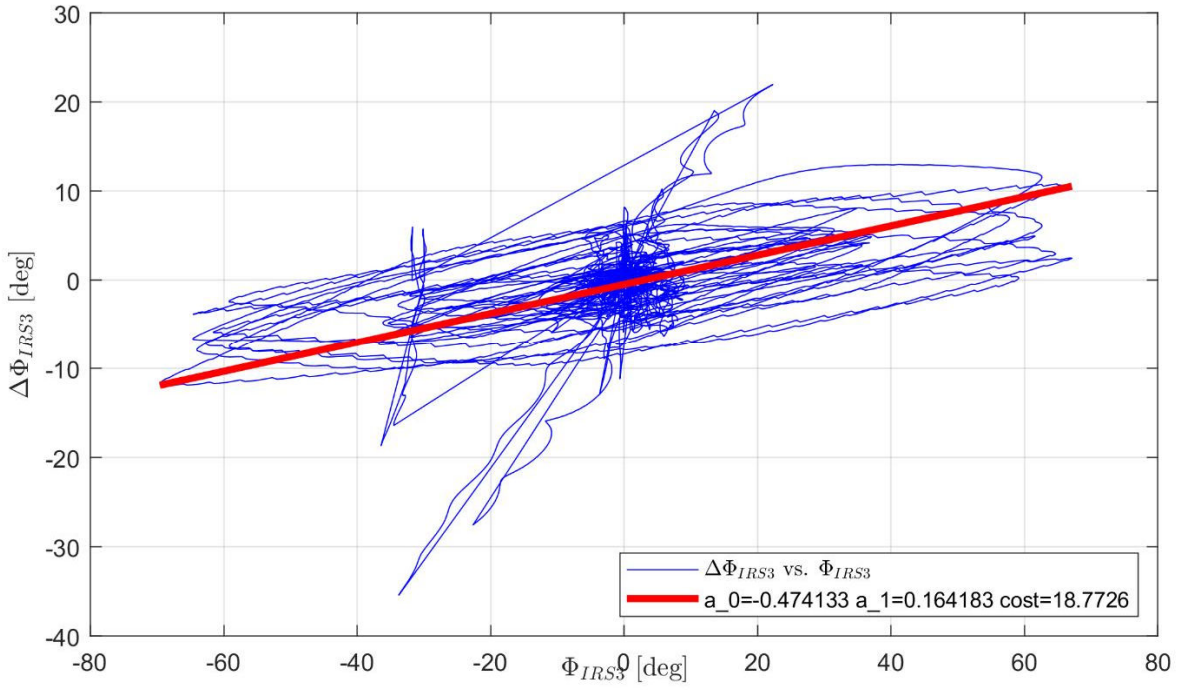

Figure 46: Comparison of the model error in the roll angle and the measured roll angle for configuration SF2.

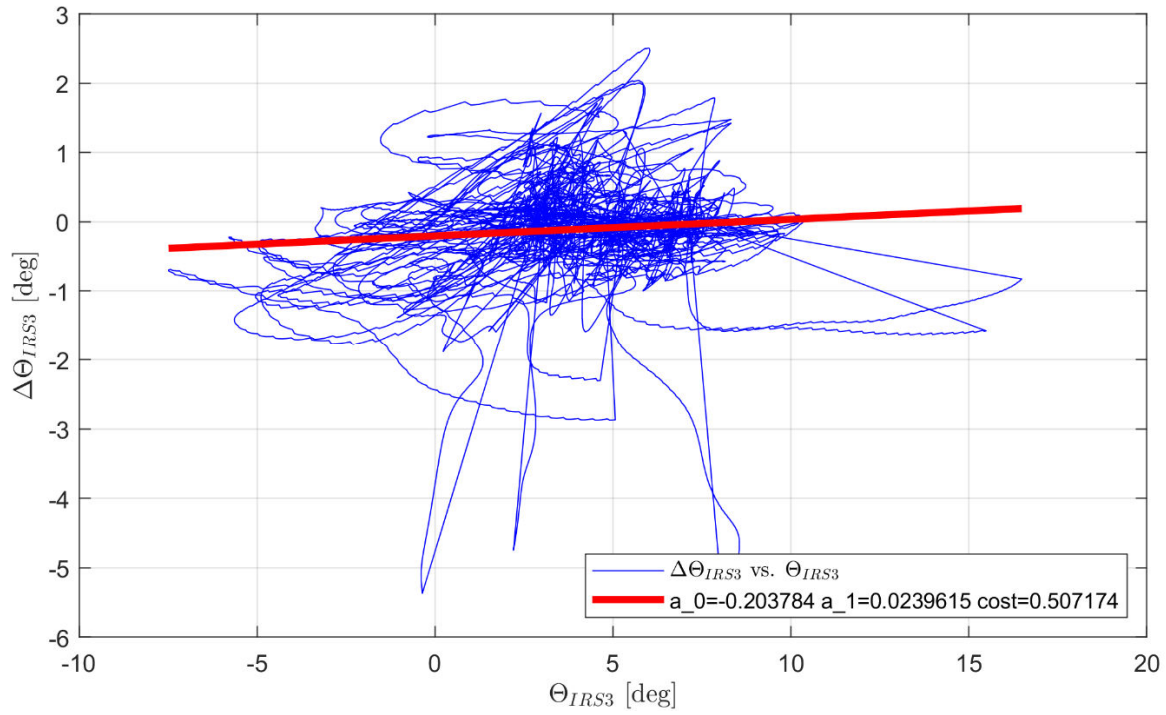

Figure 47: Comparison of the model error in the pitch angle and the measured pitch angle for configuration SF2.

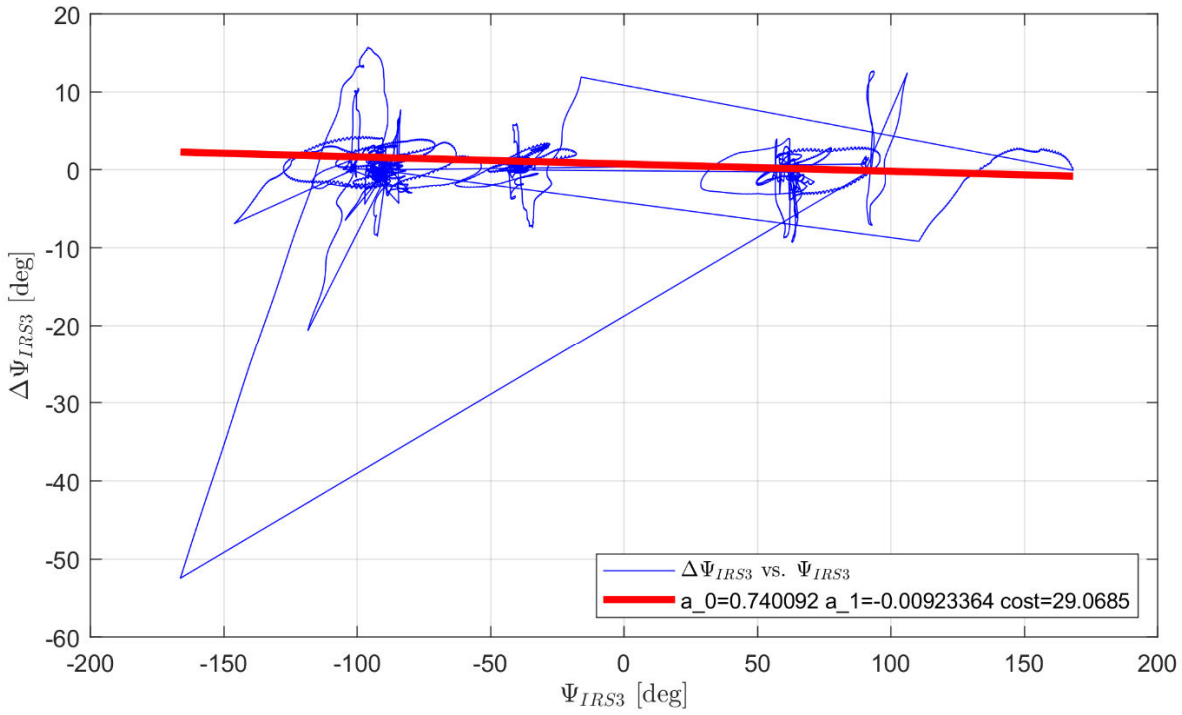

Figure 48: Comparison of the model error in the heading angle and the measured heading angle for configuration SF2.

7.6. Cross Plots – Configuration SF3

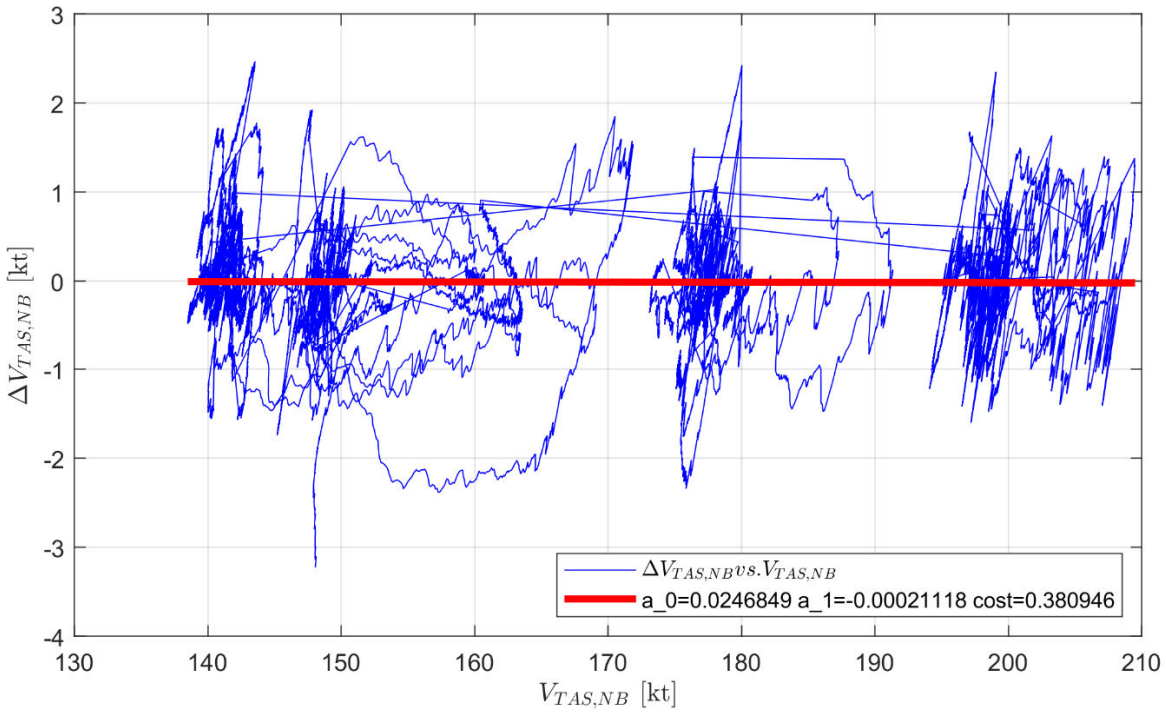

Figure 49: Comparison of the model error in VTAS and the measured VTAS for configuration SF3.

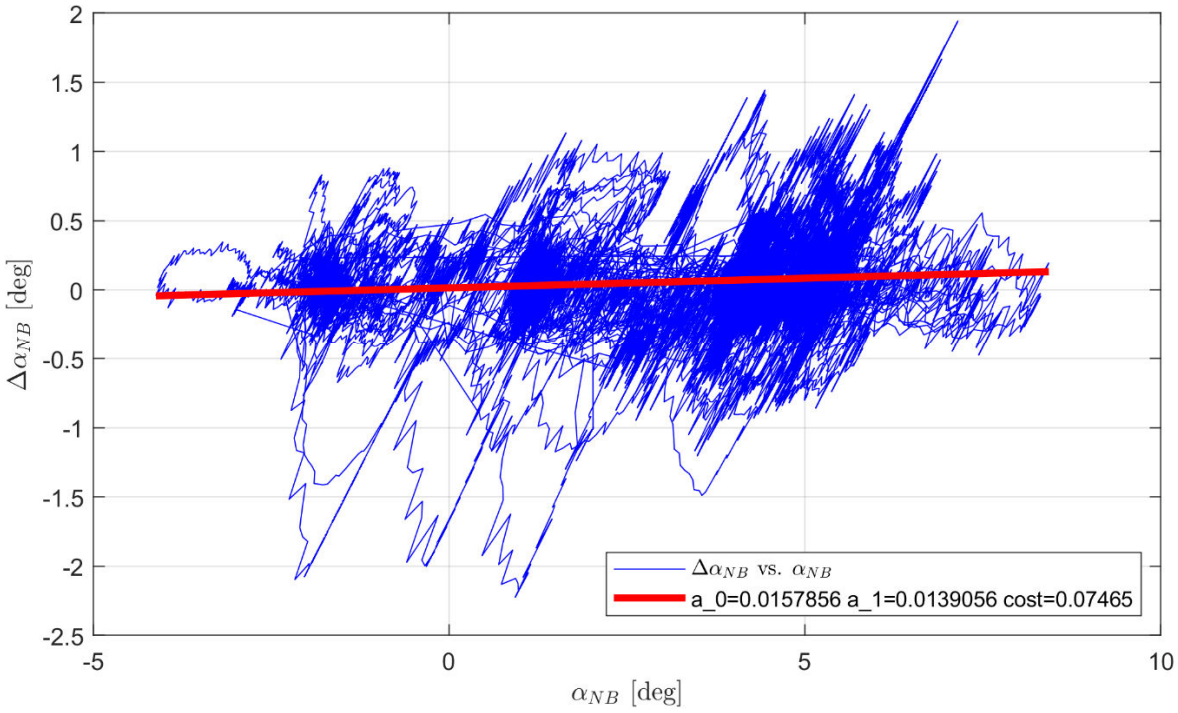

Figure 50: Comparison of the model error in the angle of attack and the measured angle of attack for configuration SF3.

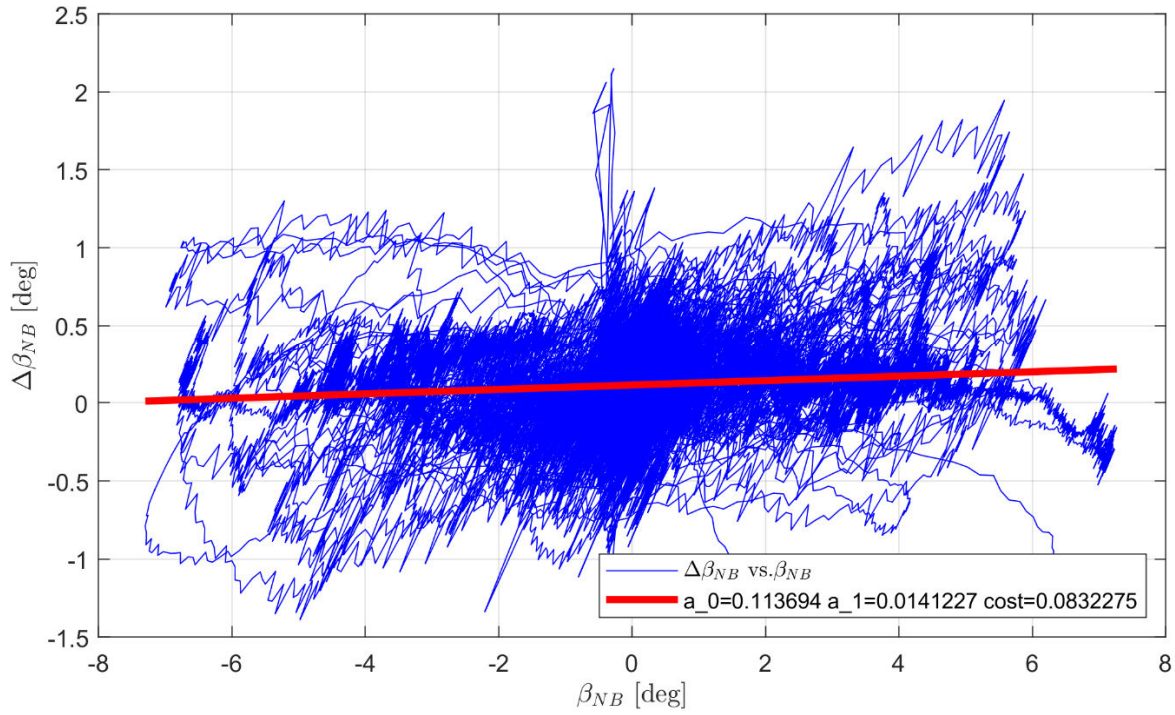

Figure 51: Comparison of the model error in the angle of sideslip and the measured angle of sideslip for configuration SF3.

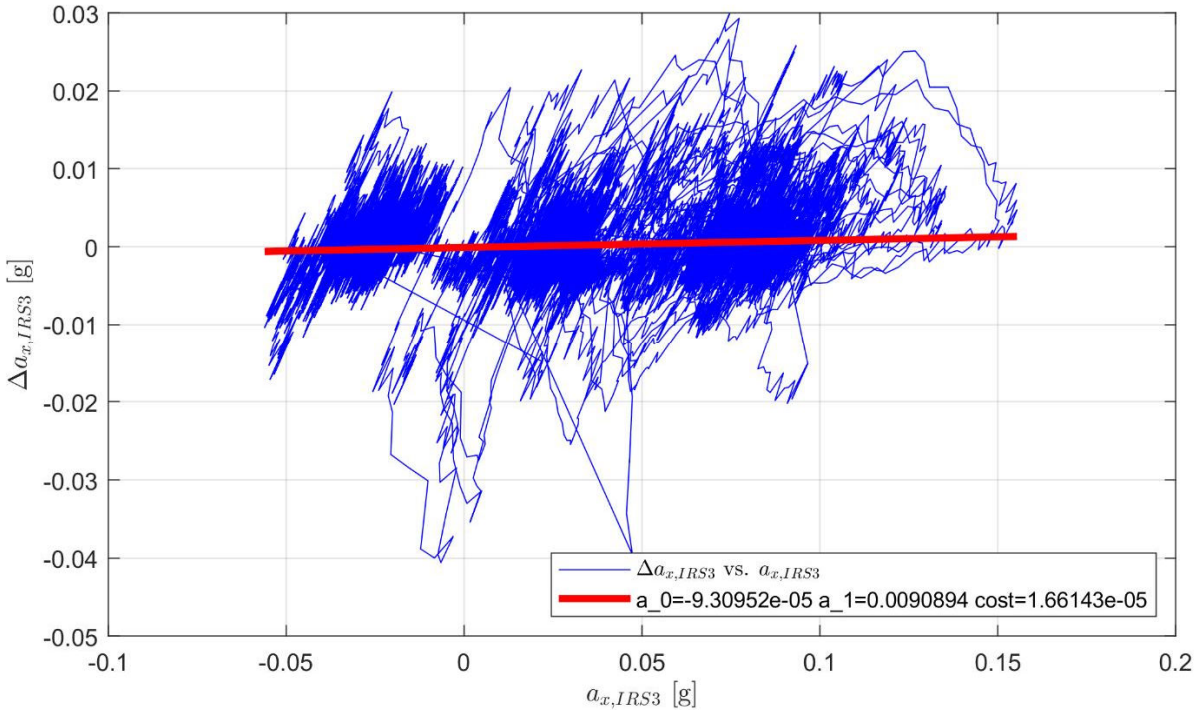

Figure 52: Comparison of the model error in the longitudinal acceleration and the measured longitudinal acceleration for configuration SF3.

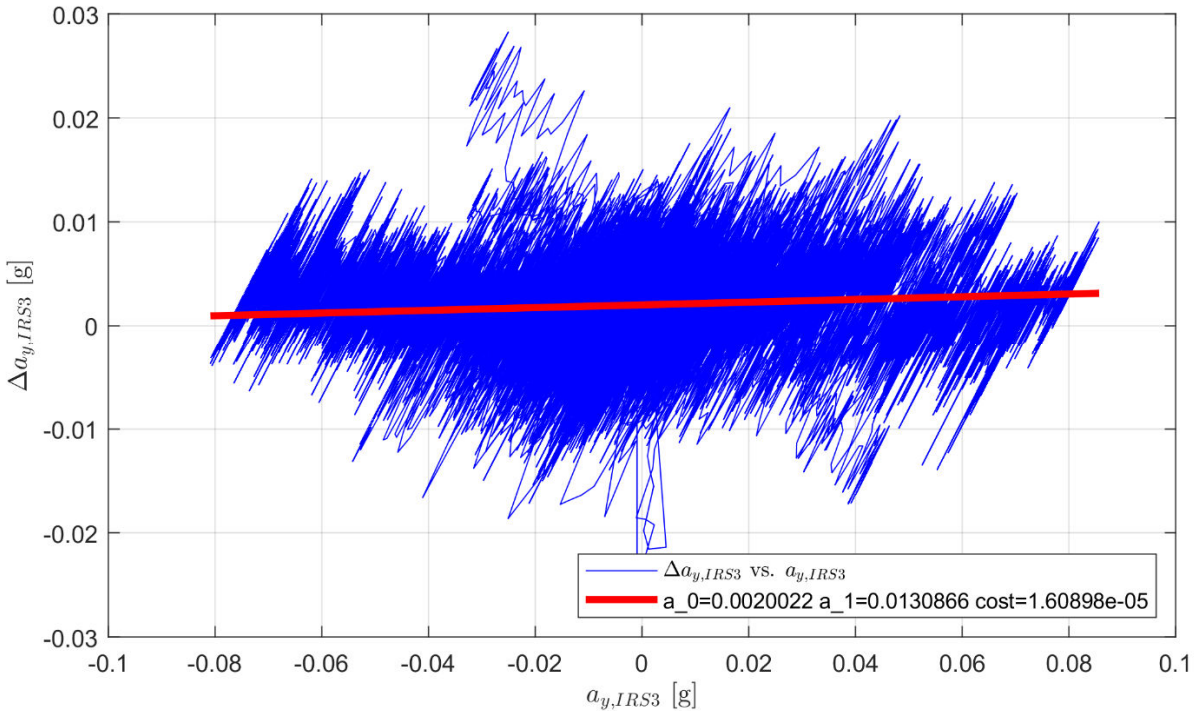

Figure 53: Comparison of the model error in the lateral acceleration and the measured lateral acceleration for configuration SF3.

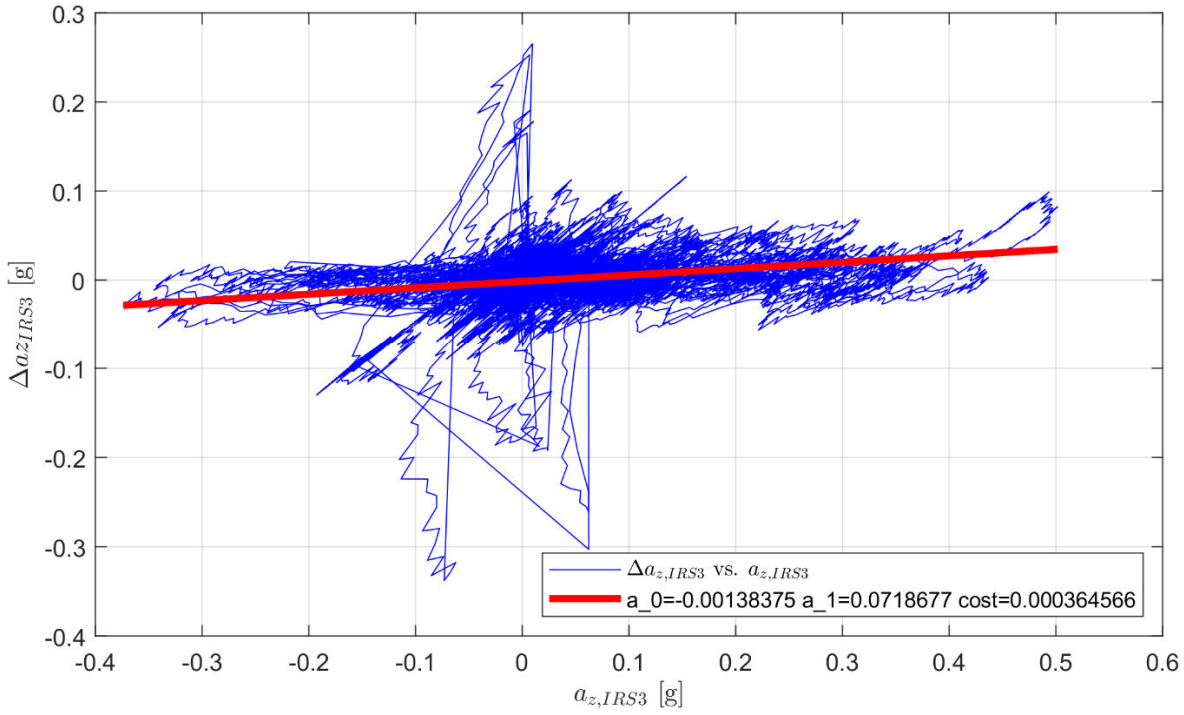

Figure 54: Comparison of the model error in the vertical acceleration and the measured vertical acceleration for configuration SF3.

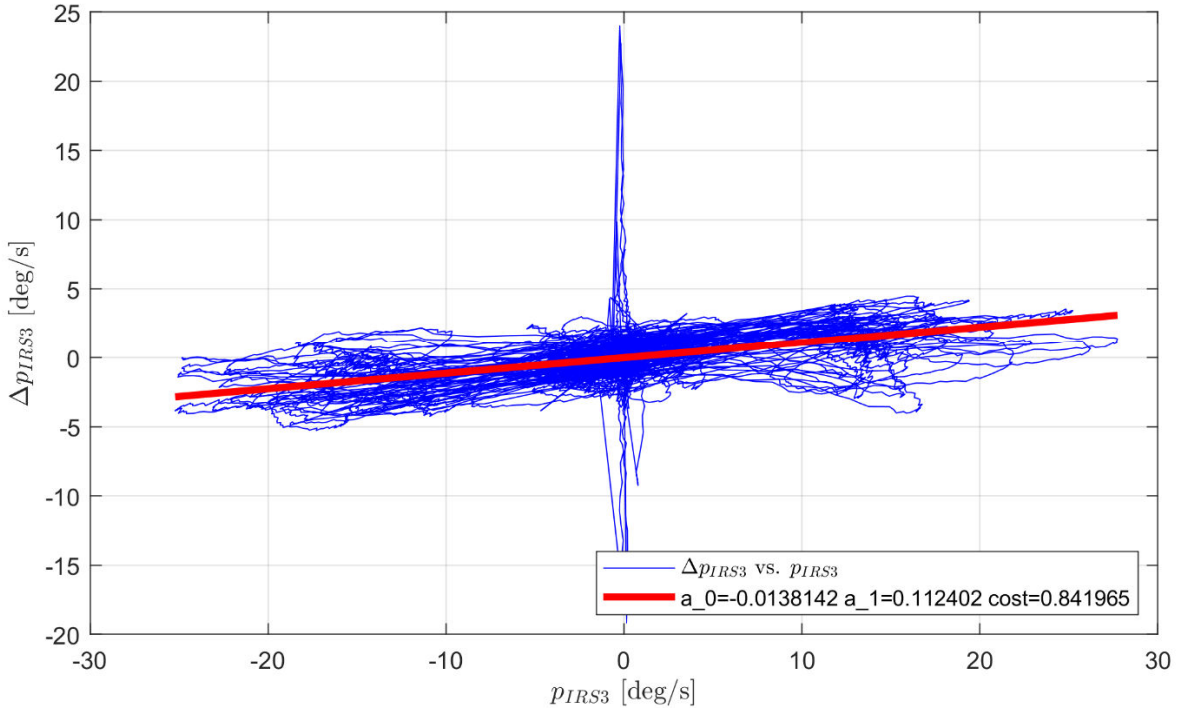

Figure 55: Comparison of the model error in the roll rate and the measured roll rate for configuration SF3.

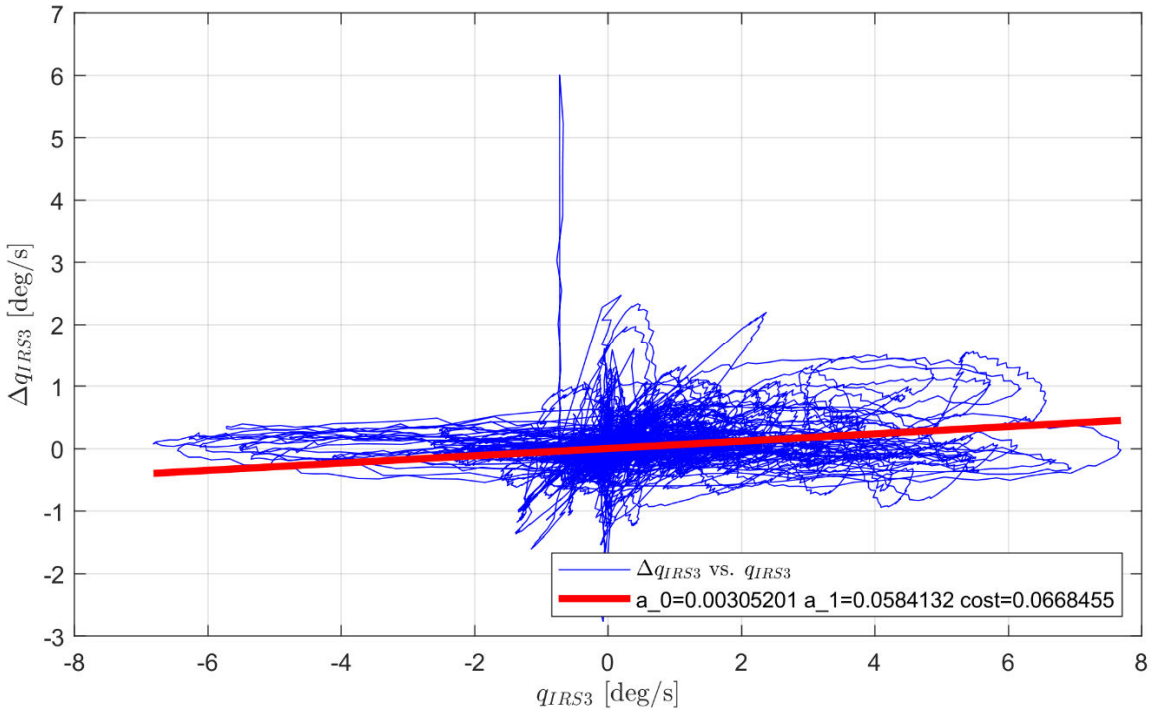

Figure 56: Comparison of the model error in the pitch rate and the measured pitch rate for configuration SF3.

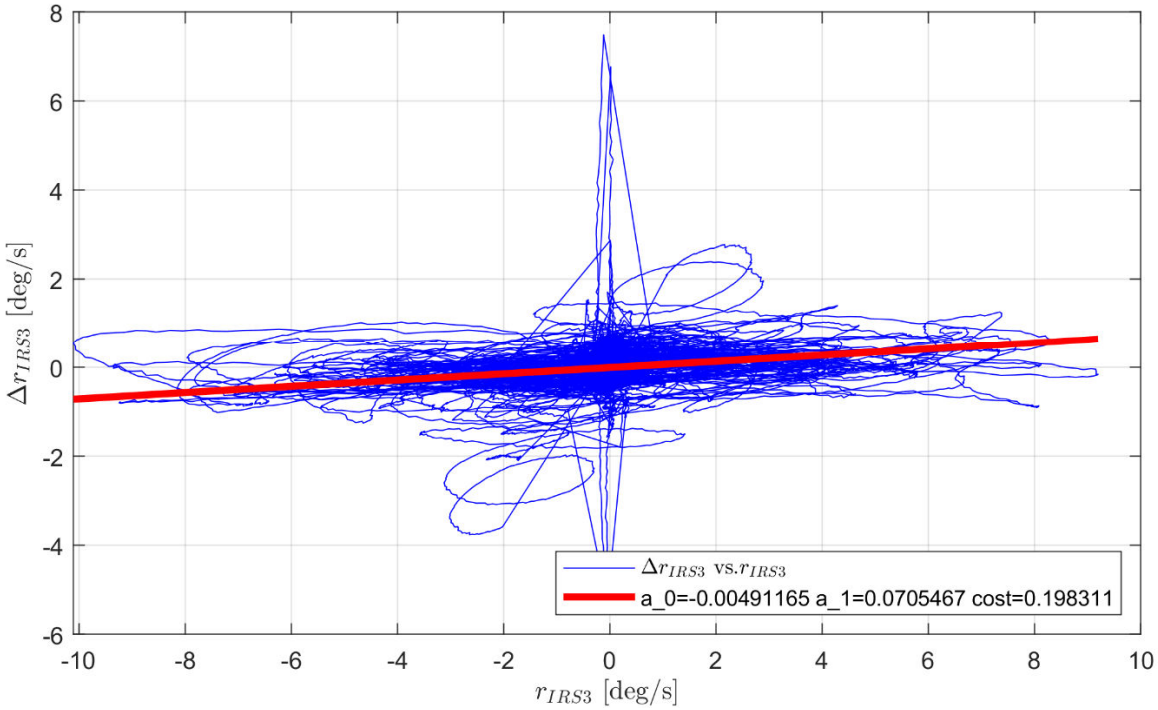

Figure 57: Comparison of the model error in the yaw rate and the measured yaw rate for configuration SF3.

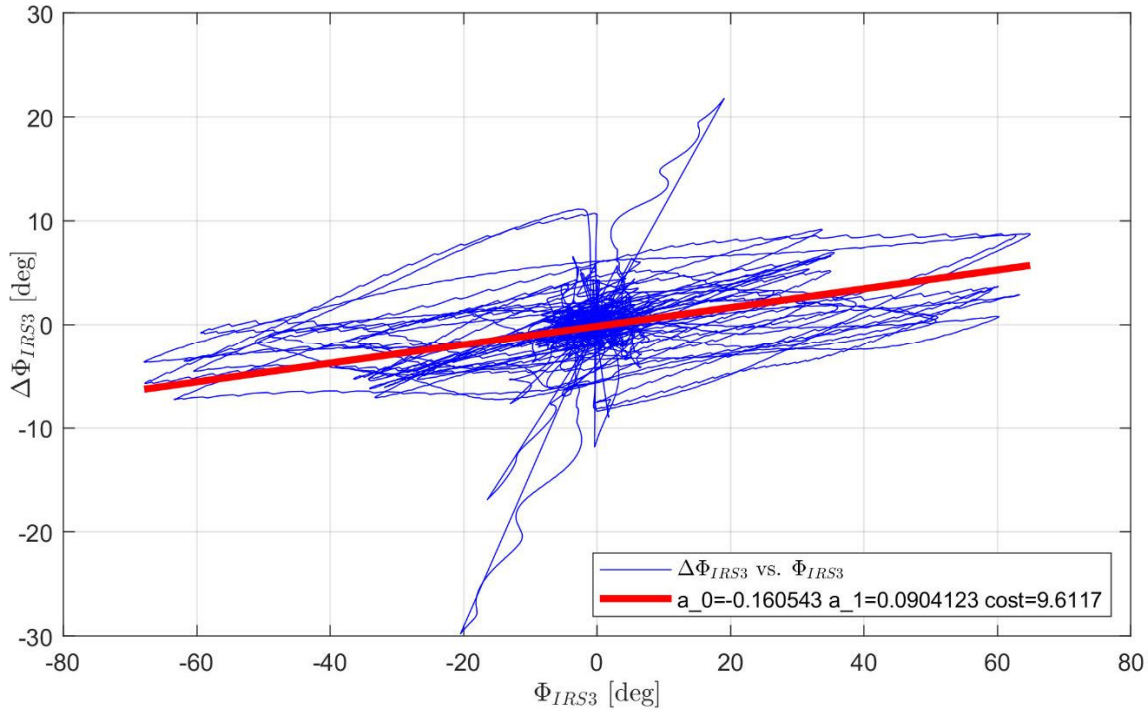

Figure 58: Comparison of the model error in the roll angle and the measured roll angle for configuration SF3.

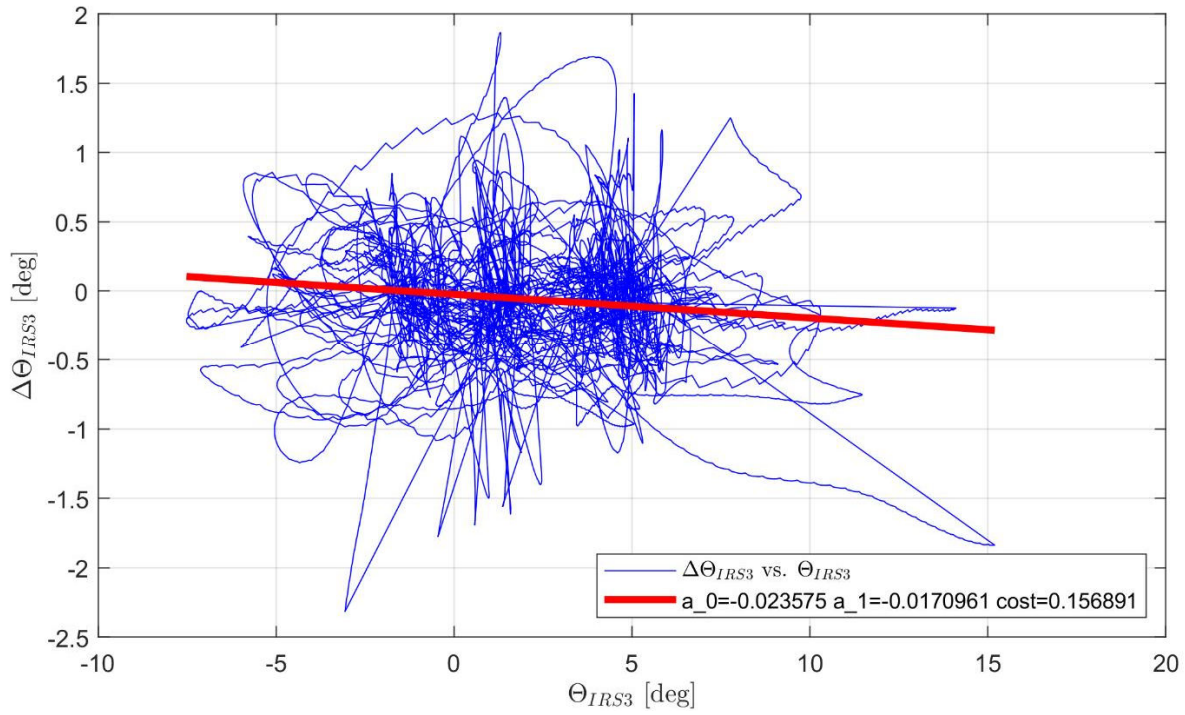

Figure 59: Comparison of the model error in the pitch angle and the measured pitch angle for configuration SF3.

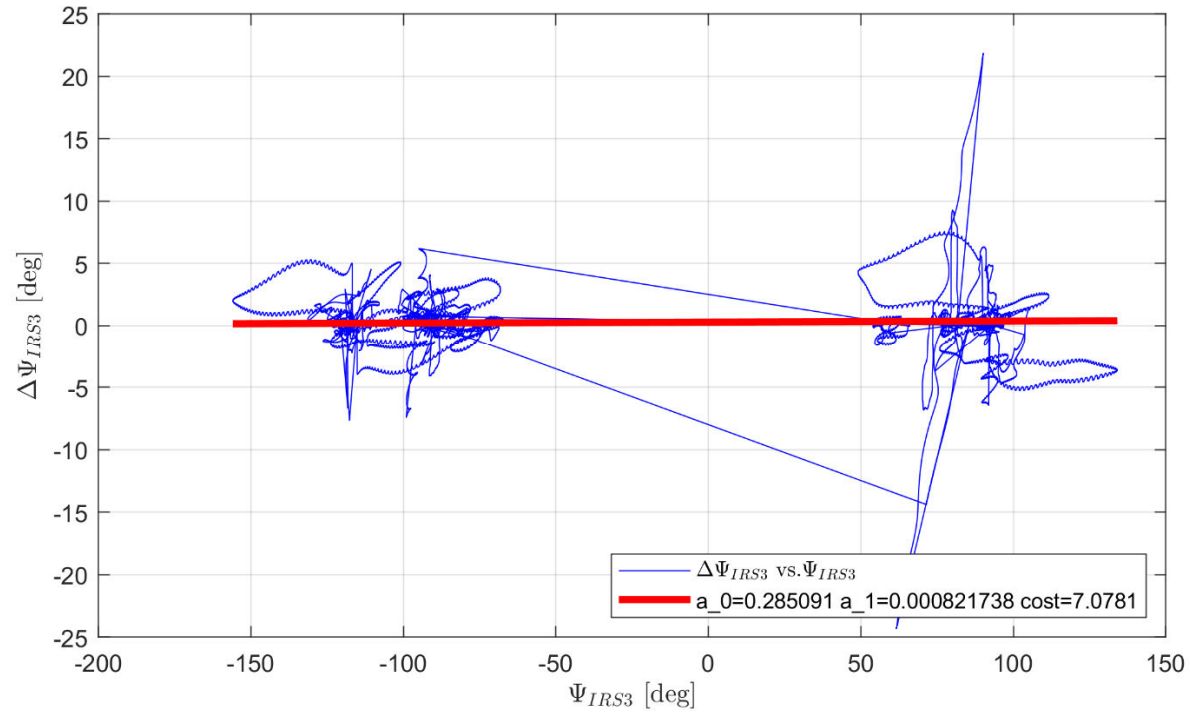

Figure 60: Comparison of the model error in the heading angle and the measured heading angle for configuration SF3.

8. Conclusion and Outlook

A preliminary flight dynamics model was developed for the ISTAR research aircraft, and the aerodynamic parameters were identified. The model was constructed using test data obtained from system identification flights. The data set was analyzed with regard to all slat/flap configurations, as well as with retracted and extended landing gear. The flight range of the model data was constrained to a speed of 80–260 knots and an altitude of 100–10,000 feet. As illustrated in Chapter 7, the cross plots demonstrate that the residual model error is minimal, and the flight dynamic behavior of the Dassault Falcon 200LX - ISTAR is accurately represented across the specified flight range. Nevertheless, the creation of a comprehensive model requires the extension of the model at specific operating points, thereby ensuring that the simulation accurately represents the flight envelope of the ISTAR. Specifically, the following points require attention:

- It is recommended that the model be supplemented with flight measurement data at velocities greater than 260 kt VIAS, in order to provide a more comprehensive representation of the flight envelope in the CLEAN configuration. This enables a more accurate mapping of the effects of Mach number.

- An improvement in the behavior of the aircraft when extending the airbrakes may be achieved by adapting the control signal to the actual spoiler position, as opposed to a discrete signal. An analysis and adaptation of the behavior during the retraction and extension of the flaps and landing gear is required.

- The analysis did not consider maneuvers with engine doublets, as an exact mapping of the engine dynamics was not yet necessary. In future extensions, an examination of the dynamic behavior of the engine should be conducted, and the model should be adapted accordingly.

- The aerodynamic model should be extended with additional parameters and terms to encompass the behavior exhibited during a stall. In the low-speed range, for instance, the lift curve becomes non-linear. It is therefore necessary to identify these properties with corresponding flight test data.

- The aerodynamic model should be augmented with the ground effect. In particular, the ground effect must be considered when simulating take-off and landing procedures.

Additional flight test data from ISTAR is required for the aforementioned points. Once these are available, the model can be rapidly and efficiently expanded with supplementary model terms, and the parameters can be re-identified. The AVES simulator model can then be updated directly. This ensures that the simulator always has an up-to-date version of the ISTAR flight dynamics, which is essential for designing suitable control and pilot assistance systems.

9. References

[1] Aguado M., Engineering Coordination Memo, Nose Boom Calibration, DA-091, Paris, 29.11.2019.

[2] Aguado, M., Engineering Coordination Memo, Answer to PCM-105 - Position of equipment and concepts on the Aircraft, DA-131, Paris, 11.11.2020.

[3] Cook, M. V., Flight Dynamic Principles: A linear systems approach to aircraft stability and control, Elsevier, Amsterdam, 2007.

[4] Dassault Aviation, Falcon 2000EX EASy Crew Operational Documentation for Dassault EASy CODDE 1 Airplane Description, DGT94085, Revision 19, Paris, 2020.

[5] Dassault Aviation, Falcon 2000EX EASy, Aircraft Maintenance Manual (AMM), Revision 28_001, Paris, 2022.

[6] Dassault Aviation, Falcon 2000EX EASy, Illustrated Parts Catalog (IPC), Revision 28_001, Paris, 2022.

[7] iMAR Navigation GmbH, iNAT-M200/SLN - iNAT-M200/MLN, Precise MEMS Based Inertial Navigation System with integrated INS/GNSS/xxx Data Fusion, Technical Data Sheet, rev. 2.16, DOC170201078, iMAR Navigation GmbH, St. Ingbert, 28.02.2020.

[8] Jategaonkar, R. V., Flight Vehicle System Identification: A Time Domain Methodology, American Institute of Aeronautics and Astronautics, Reston, VA, 2006.

[9] Jategaonkar, R. V., Identification of the Aerodynamic Model of the DLR Research Aircraft ATTAS from Flight Test Data, DLR Forschungsbericht 90-40, DLR Institut für Flugsystemtechnik, Braunschweig, 1990.

[10] Klamann, U., ISTAR – Air Data Nose Boom Ausrichtung, Technical Document, ISTAR Kal.-Nr. I0110, DLR Institut für Flugsystemtechnik, Braunschweig, 15.07.2021.

[11] Klamann, U., ISTAR Sonden Positionskoordinaten, Technical Document, ISTAR Kal.-Nr. I0121, DLR Institut für Flugsystemtechnik, Braunschweig, 24.02.2022.

[12] Klamann, U., Kalibrierprotokoll, ISTAR - ADM3 Static and Total Pressure Sensor, Technical Document, ISTAR Kal.-Nr. I0128, DLR Institut für Flugsystemtechnik, Braunschweig, 24.02.2022.

[13] Klein, V. and Morelli, E., *Aircraft System Identification: Theory and Practice*, American Institute of Aeronautics and Astronautics, Reston, VA, 2006.

[14] Lacoste, J. P., Dassault Aviation ISTAR Project - Feasibility Studies Report WP1.2 - Aerodynamics and Models of F2000EX s/n 6 Aircraft, DGT 158331, 13/02/2017.

[15] Lübbeke, J., Klamann, U., ISTAR INS Hebelarme der GNSS-Antennen, Technical Document, ISTAR Kal.-Nr. I0105, DLR Institut für Flugsystemtechnik, Braunschweig, 24.02.2021.

[16] Mönnich, W., Ein 2-Punkt-Aerodynamikmodell für die Identifizierung, Systemidentifizierung in der Fahrzeugdynamik: Symposium des Sonderforschungsbereichs SFB 212 „Sicherheit im Luftverkehr“, Braunschweig, März 10-11, 1987.

[17] Raab, C., Check your Air Data – Setup and practical Examples for the Flight Data Compatibility Check, Society of Flight Test Engineers European Chapter 34th Symposium, 16.-18. May 2023, Rom, Italy.

[18] Raab, C., Dassault Falcon 2000LX ISTAR - Flight Data Gathering and DCC for System Identification - V 1.00. DLR – Institute of Flight Systems, Internal Report, DLR-IB-FT-BS-2022-119, Braunschweig, 2022.

[19] Raab, C., Dassault Falcon 2000LX ISTAR – System Identification Part II – Estimated Aerodynamic Parameters – V1.0, Internal Report, DLR-IB-FT-BS-2024-XXX, Institute of Flight Systems, Braunschweig, 2024.

[20] Raab, C., Flight Test Request - HighFly (High Speed Inflight Validation) – System Identification Flight Tests, DLR Technical Document, FTR-IST-HPID-2020-001-A, DLR Einrichtung Flugexperimente, Braunschweig, 2020.

[21] Seher-Weiss, S., FitlabGui – A MATLAB Tool for Flight Data Analysis and Parameter Estimation, Version 2.7.5, Institutsbericht IB 111-2015/34, DLR Institut für Flugsystemtechnik, Braunschweig, 2015.

[22] Stevens, B. L. and Lewis, F. L., Aircraft Control and Simulation, John Wiley & Sons, 2003.

[23] Zach, Adolf, Kalibrierprotokoll, ISTAR-Bord-Kalibrierung der Querruder-Stellungssensoren, Kal.-Nr. I0103, DLR Institut für Flugsystemtechnik, Braunschweig, 03.09.2020.

List of Figures

List of Tables

4